INFORMATION TO USERS

This manuscript has been reproduced from the microfilm master. UMI films the text directly from the original or copy submitted. Thus, some thesis and dissertation copies are in typewriter face, while others may be from any type of computer printer.

The quality of this reproduction is dependent upon the quality of the copy submitted. Broken or indistinct print, colored or poor quality illustrations and photographs, print bleedthrough, substandard margins, and improper alignment can adversely affect reproduction.

In the unlikely event that the author did not send UMI a complete manuscript and there are missing pages, these will be noted. Also, if unauthorized copyright material had to be removed, a note will indicate the deletion.

Oversize materials (e.g., maps, drawings, charts) are reproduced by sectioning the original, beginning at the upper left-hand corner and continuing from left to right in equal sections with small overlaps. Each original is also photographed in one exposure and is included in reduced form at the back of the book.

Photographs included in the original manuscript have been reproduced xerographically in this copy. Higher quality 6" x 9" black and white photographic prints are available for any photographs or illustrations appearing in this copy for an additional charge. Contact UMI directly to order.

UMI®

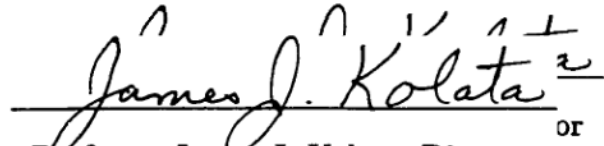# ELASTIC SCATTERING OF ^{9}Li AND ^{11}Li FROM ^{12}C AT 50 MeV PER NUCLEON

A Thesis

Submitted to the Graduate School

of the University of Notre Dame

in Partial Fulfillment of the Requirements

for the Degree of

Doctor of Philosphy

by

Donald A. Peterson,

Professor James J. Kolata, Director

Department of Physics

Notre Dame, Indiana

March 2001

UMI®

ELASTIC SCATTERING OF ^{9}Li AND ^{11}Li FROM ^{12}C AT 50 MeV PER NUCLEON

Abstract

by

Donald A. Peterson

The elastic scattering of ^{9}Li + ^{12}C and ^{11}Li + ^{12}C has been measured with the S800 Spectrograph at Michigan State University at an energy of 50 MeV/A over the angular range of 2–15° in the center-of-mass frame. The energy resolution of the S800 provided the ability to separate true elastic from inelastic reaction channels, especially at forward angles. Dispersion-matched focusing was utilized to further improve the energy resolution. Ray-tracing techniques making use of measured field data were necessary to determine scattering angles.

A Monte Carlo code was developed to determine the acceptance of the spectrograph and to understand the interaction of the Li ions with the complex series of apertures, focusing elements, and fringe fields comprising the S800,. A successful technique for actively correcting gain shifts in the tracking detectors was developed. Techniques for correcting aberrations in the field maps used in the ray-tracing were explored with partially acceptable results.

An intrinsic energy resolution of < 1 MeV was obtained, which was negligible compared to straggling effects in the targets (2–6 MeV). An intrinsic angular resolution of 10 mr in the laboratory frame (1.1° c.m.) was achieved, limited both by uncertainties in ray tracing and poor performance of tracking detectors. The angular distributions obtained in this experiment appear to confirm prior ^{9}Li measurements.

Donald A. Peterson

The ^{11}Li results are also striking, as they show an absence of the near-side/far-side interference at forward angles as seen in prior measurements. This indicates a need for further refinement in the interaction models used to describe this exotic nucleus.

For my family

ii

CONTENTS

iii

iv

TABLES

vi

FIGURES

ix

x

xi

ACKNOWLEDGEMENTS

First and foremost I wish to thank my adviser, Professor James J. Kolata, for his guidance through these past few years. His enthusiasm and passion for physics was inspiring. He consistently provided new ideas and avenues of analysis, helping to keep me on track toward the end result whenever it started to disappear behind the minutia of analysis. I would also be remiss without thanking my colleague, Dr. Peter Santi, not only for his friendship which helped us both through some difficult times, but for our many discussions about physics as well as those intangible things that make up the everyday experiences of life.

I also wish to thank Professors Peter Jolivette and Paul DeYoung of Hope College, who taught the majority of my undergraduate courses and provided me with the original impetus to pursue physics at an advanced level. It has been a privilege to collaborate with them throughout the last ten years of my graduate and undergraduate life.

I would also like to thank Drs. Brad Sherrill and Daniel Bazin of Michigan State University (MSU) for their expertise in spectrograph analysis techniques—especially as they pertain to the S800 Spectrograph at MSU. Their emails, details, and conversations regarding the subtleties of this data and the nuances of the S800 have been of great assistance in achieving these results. A special "thank you" goes to Dr. Jeff Tostevin from the University of Surrey for generously providing DWBA calculations for these reactions. I would like to express a most heartfelt thanks to Dr. Walter Loveland of Oregon State University for employment as his postdoctoral

assistant and for his patience and understanding through the finishing process of this thesis.

The people of the Nuclear Structure Lab (NSL) at Notre Dame have helped these years pass by quickly and I will miss their support and company. Larry Lamm, James Kaiser, and Charlie Guy have provided many interesting conversations. I wish them the best of luck with the new pelletron. Sandy Trobaugh and the rest of the physics department secretaries have been of immense help with supplies and red tape. I also wish to thank my fellow graduate students with whom I've learned and shared much over the years. I must make a special mention of the help Mr. Ed Stech provided in running the little errands necessary at Notre Dame while I was stationed in my new position at Oregon State. Finally, a special thanks is due to Dr. Jeffrey M. Squyres in the Computer Science and Engineering department at Notre Dame. He has introduced me to many useful computing tools and techniques, and our "MBC" meetings have been most entertaining.

I must thank my family for their unending support. My parents, Gladys June and the late Donald Rudolph, expressed a faith in me that was a constant source of comfort through the tough times. I love you! The support and interest (even if it was feigned at times) of my brothers: Doug, Daryl, DeWayne, and Dex, my sister Donna, and my sisters in law: Jan, Mary, Sallie and Brenda has been greatly appreciated. My nephews, Peter, Micah, Michael, and Bryan provided the comic and stress relief necessary to relax when I visited home. I wish them the very best in their futures.

Finally, words cannot express the gratitude I have for my wife, Karen Anne, for her undying love, support, encouragement, and nagging through the process of finishing my analysis and writing this Thesis. Many times her support was the only thing that kept me sane through this inherently insane process. Whenever I was

xvii

ready to throw in the towel, she was there with words of encouragement, if not wisdom. She has been more than patient through this endeavor, and further words cannot express my true feelings without embarrassing her greatly, so I will conclude by simply saying I love her with all my heart. This work closes one chapter of our lives and opens the next. I look forward to the rest of our lives.

CHAPTER 1

Introduction

1.1 Background

1.1.1 A new era

At the turn of the century, a new field of physics was about to be born. Becquerel made his famous studies of X rays in 1896 [1]. In 1897 J.J. Thomson discovered the electron [2]. Since atoms are neutral, it was deduced that there must be oppositely charged constituents as well, and studies regarding the nature of the atom and radiation were launched. Ernest Rutherford was particularly interested in the scattering of alpha particles, now known to be the nucleus of the He atom. From 1907–1909 Rutherford, along with his assistants, Hans Geiger and Ernest Marsden, studied the scattering of alpha particles at great length, culminating in a search for evidence of particles scattering backward. The result was astonishing, for it indicated that roughly one in eight thousand incident α particles bounced back [3]. It was determined that such backscattering must be caused by a collision with a very small, hard object in the target, described by Rutherford in March, 1912 as "a central electric charge concentrated at a point" [4]. Around this point was a "uniform spherical distribution of opposite electricity" [4]. We now call the central hard point the nucleus, and the opposite electricity is the orbiting cloud of electrons. Of course, further experiments have shown the electron cloud to be not as Rutherford expected, but the concept of a nucleus has withstood the test of time and experiment and spawned the era of Nuclear Physics. Nearly twenty years elapsed before

1

the final piece of the nuclear puzzle would be found. Another of Rutherford's former students, James Chadwick, discovered the neutron [5] by building on studies of Curie and Joliot [6]. The field of nuclear physics was now in full-swing.

1.1.2 More discoveries

With the basics of nuclear structure in-hand, the next step was to explore the forces binding the nucleons (the protons and neutrons that constitute the atom's nucleus) together and to find out just how they interact with each other. This led to the discovery of the strong and weak nuclear forces. New conservation laws, such as baryon number and isotopic spin were established. Experiments were performed to probe the inner-workings of the nucleus. These would pave the way for yet another new field of physics, the realm of "high-energy" or "elementary particles", but that lies outside the scope of this thesis. Other studies systematically explored how the nucleonic forces and interactions depend on the number and type of particles involved. It was discovered that as one changes the ratio of protons to neutrons, especially by adding many excess neutrons, the fundamental structure created by the nuclear interactions begins to change and new features develop. To understand such behaviors requires quantum theory and Heisenberg's uncertainty principle.

1.1.3 Tanihata's discovery

The experiments and measurements relevant to the halo phenomenon will be discussed in more detail in the following section, but are briefly summarized here. One of the most recent and exciting of these developments was due to Tanihata, in 1985 [7]. It had been well-established that the nuclear mass density is approximately constant, so the radius of a nucleus is proportional to the cube-root of the number

2

of nucleons (A) it is composed of,

$$R = R_0 \sqrt[3]{A}, \tag{1.1}$$

where R_0 in the above equation is usually taken as 1.2–1.3 fm. However, a more-often measured quantity is the root-mean-square (rms) radius, $\langle r^2 \rangle^{1/2}$. For comparison, assume a uniformly charged sphere of radius R. Then, we can find the rms charge radius as follows:

$$\langle r^2 \rangle = \frac{\iiint_V (r^2)}{\iiint_V} = \frac{\int_0^R \int_0^\pi \int_0^{2\pi} (r^2) r^2 \sin\theta \, dr \, d\theta \, d\phi}{dV}$$

$$\langle r^2 \rangle = \frac{4\pi}{V} \int_0^R r^4 dr = \frac{4\pi}{V} \frac{R^5}{5}. \tag{1.2}$$

The volume of a sphere of radius R is

$$V = \frac{4}{3}\pi R^3,$$

leaving us with

$$\langle r^2 \rangle = \frac{3}{5} R^2. \tag{1.3}$$

Using Eq. (1.1) (with $R_0 = 1.25$) and Eq. (1.3), we find for the rms charge radius,

$$\langle r^2 \rangle^{1/2} \approx 0.97 A^{1/3}. \tag{1.4}$$

This implies that the nuclear density is essentially constant as previously noted. However Tanihata found that, even though ^{9}Li has an rms radius of 2.3 fm, approximately obeying Eq. (1.4), ^{11}Li was much larger than expected. In fact, ^{11}Li is found to have an rms charge radius of about 3 fm [8], which is 40% larger than expected. Even more striking is that the matter distribution, illustrated in Fig. 1.1, extends to beyond 8 fm. By contrast, the nucleus ^{208}Pb has an rms radius of about 5.5 fm [9].

3
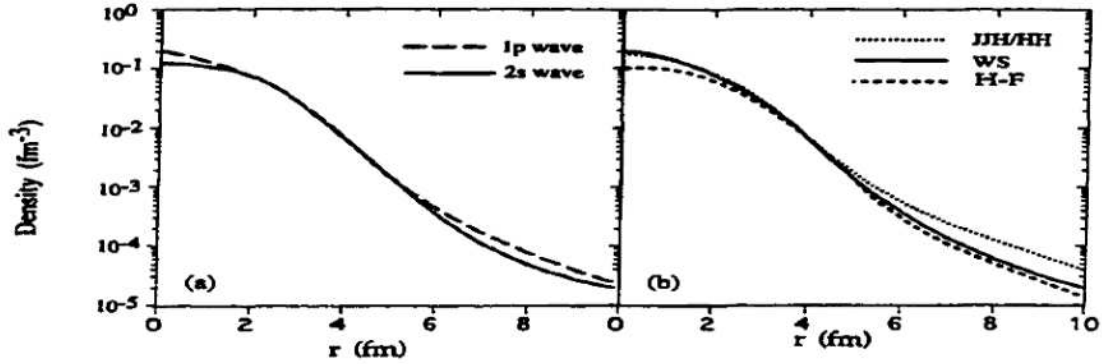
Figure 1.1. The ^{11}Li density distribution determined from interaction cross section measurements with several targets. The left panel represents experimental central values based on assumptions about the halo orbital. The curves in the right panel are various theoretical models. (Taken from [8])

The discovery of a system with less than a dozen particles being comparable in size to a system of over 200 particles was at once both striking and exciting. A whole new world of physics was about to be explored.

1.1.4 "Halo" physics

The structure of ^{11}Li can be described as a ^{9}Li core with two extra, or valence, neutrons orbiting at a larger distance leading to an extended matter distribution with low density that is nearly pure neutron matter at a large radius. This became known as the "neutron halo" structure, and the properties of this neutron halo generated much theoretical excitement [10–14, for example] and became the subject of many experiments [15–20]. The interpretation of the experimental data has generated even more theoretical excitement [21–24]. Not only is the halo nature of interest, but also the interactions responsible for holding such a system together. On their own in nature, two neutrons will not form a stable system. Similarly, ^{10}Li as a ^{9}Li+n subsystem is unbound in nature. So, ^{11}Li forms a true, bound, three-body system in which each two-body subsystem is unbound. Several other

4
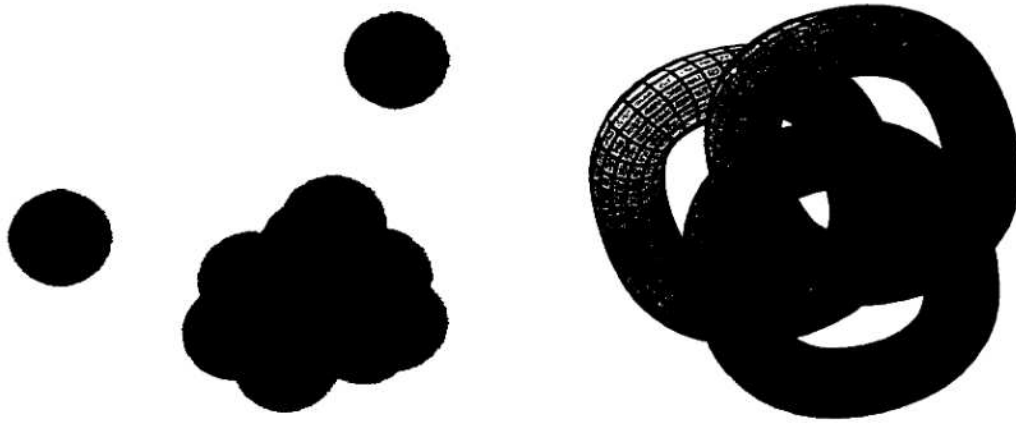
Figure 1.2. The interlocking "Borromean" rings. If any one ring is removed, the remaining two fall apart. The subsystems of ^{11}Li behave in the same manner.

light nuclei, such as ^{6}He and ^{14}Be, exhibit this same type of structure. This class of nuclei has been given the name "Borromean", after the heraldic symbol of the princes of Borromeo which consists of three interlocking rings as shown in Fig. 1.2. These nuclei allow theorists to test their favorite models of three-body interactions on real, tangible objects and has generated much interest. The physics of the halo structure is discussed in more detail in Chapter 2.

One of the experiments to explore the halo features of ^{11}Li was performed by Kolata et al. in 1992 [16]. That experiment hoped to measure the structure through elastic scattering. Due to the limitations of the detectors and energies used, they were unable to differentiate between true elastic events and contributions from inelastic reaction channels. The results of their experiment were puzzling, even after accounting for the inelastic contributions. Several different approaches have been tried to describe the data, but none so far have been truly satisfactory. Khoa et al. [22] proposed what was presumed to be a realistic scenario for the scattering, but this failed to describe the forward-angle data. Mermaz [25] found phenomenological optical model (OM) parameters that could fit all the scattering data rather well, but the resulting parameters are highly unusual, and seem to be non-physical. Fur-

5

thermore, as will be discussed in Chapter 2, due to the experimental technique and the inability of the "complete" models to describe the forward-angle data, there has arisen some question as to whether some problem may exist with the published data. This experiment was designed to repeat the elastic measurements in an attempt to resolve these discrepancies.

1.2 Organizational overview

1.2.1 The big picture

This thesis is structured in the following manner. First we lay out the groundwork for the physics and motivation of this study in Chapter 2. The second part of the thesis focuses on technique. Chapters 3 and 4 discuss the experimental setup and detector calibration, while the methodology of the analysis is explained in Chapters 5 and 6. Finally Chapter 7 concludes the thesis by revealing the results with some discussion as to their importance.

1.2.2 Specifics

Chapter 2 provides the theoretical background and framework for studying nuclear systems, focusing on elastic scattering. A discussion of the nuclear shell model, the optical theorem, and the optical model is given. From there the existence and nature of halo structures is explored. Finally, the chapter closes by presenting the previous data of Kolata et al. [16] along with discussion of the various attempts to describe the data which motivated the present experiment.

Chapter 3 describes the experimental setup and procedure for the scattering measurements performed for this thesis. It discusses the beam preparation and transport, the targets used, and the detectors that comprise the S800 Spectrograph. The technique of using dispersion-matching to improve spectrograph resolution is also presented. Finally, it closes with a preview of the analysis technique, which is

6

more fully discussed in Chapter 5.

Conventionally, discussion of detector calibration is rather limited in scope and presented as part of the analysis technique. However, there were so many pitfalls and nuances to the detector system of this experiment that the calibration really earned a chapter of its own. Chapter 4 holds the details and techniques used to gain self-consistent calibrations.

Chapter 5 holds the crux of the experiment—the data analysis. This chapter discusses the methods used in extracting meaningful results from the raw measured parameters, including pre-sorting the data into a compressed set. The discussion of the analysis itself begins with a general discussion of technique and methodology and what parameters are needed. The development of the sorting algorithms used, as well as appropriate gates for isolating "good" events from "bad" ones is discussed. The transfer maps that describe the trajectory through the S800 are explained and the modifications necessary to achieve self-consistency are discussed. All this is put together to obtain raw scattering spectra.

Chapter 6 continues the analysis, exploring the systematics of the S800 Spectrograph system through the use of Monte Carlo techniques. The details of the physics inputs and intricacies of the Monte Carlo code are relegated to an appendix, but the essential results are presented here. It is shown how Monte Carlo simulation allows the unfolding of the coupling between momentum, position, and divergence to determine systematic uncertainties in the transfer maps. It concludes by presenting the final determined scattering distributions.

Chapter 7 pulls the two analysis chapters together to discuss the final ratio-to-Rutherford cross sections. Along with these results, some final remarks and conclusions about this data are given, as well as an outlook for further studies and analysis.

CHAPTER 2

Theoretical background and motivation

2.1 Basics of nuclear structure

Before discussing halo nuclei and their importance, we must first establish the basics of nuclear structure so that we can see how special halo systems are. We begin our discussion with the nuclear force and then explore the simplest and lightest nuclei and what makes them stable.

The nuclear force is the strongest of the four fundamental forces of nature, whose relative strengths are listed in Table 2.1.   The nuclear force has a very short range of only 2–3 fm. It is mainly attractive, but turns repulsive for distances less than 0.5 fm. The short range means that a nucleon essentially only interacts with its closest neighbors. The dual nature of attraction and repulsion is in large part responsible for the essentially constant density of nuclear matter. The repulsive nature keeps nucleons from imploding upon each other or becoming infinitely dense while the attractive part is responsible for binding nucleons together to form a stable system.

Table 2.1. Relative strengths of the four fundamental forces

Force	Strength
Strong Nuclear	1
Electromagnetic	10^{-2}
Weak Nuclear	10^{-14}
Gravitational	10^{-54}

8
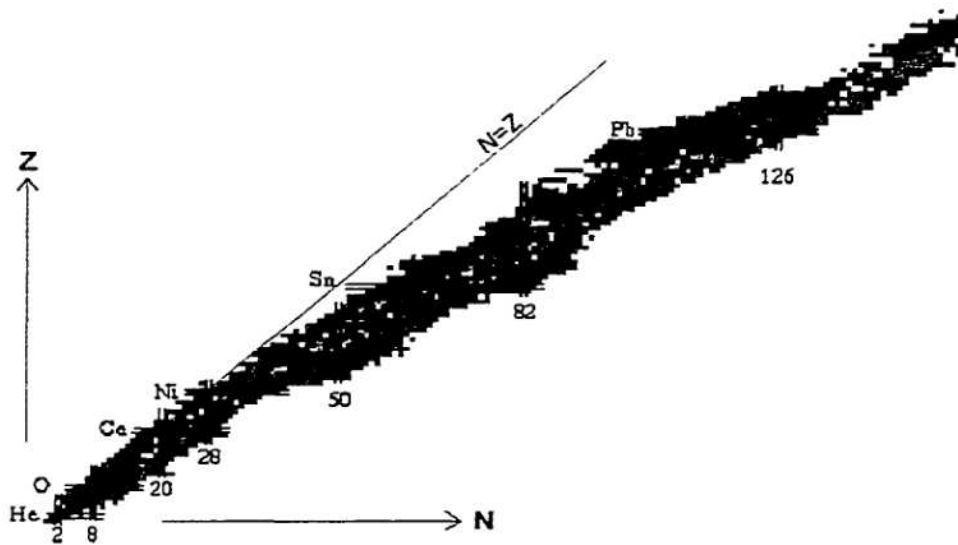
Figure 2.1. Chart of the nuclides. Known nuclei are plotted as proton number versus neutron number, with the so-called "magic numbers" (§2.1.2) of shell closures indicated. Nuclei in the valley of stability are denoted by black cells, known radioactive nuclei bound against strong decay lie in the shaded regions.

2.1.1 Binding energy and stability

Figure 2.1 plots the known nuclei as a function of proton number Z and neutron number N. This is known as the chart of the nuclides. The stable elements are darkened and lie in a region known as the "valley of stability" for reasons which will become clear later. For the lightest nuclei ($A \lesssim 40$) the stable nuclei lie along the $N = Z$ line with equal numbers of protons and neutrons. As we progress toward the heavier elements, the ratio of neutrons to protons increases, becoming roughly 1.5:1. The extra neutrons are needed to provide additional binding to overcome the electromagnetic repulsion of many protons.

Figure 2.2 shows an expanded view of the chart of nuclides in the region of very light nuclei. This figure also indicates the locations of neutron-halo (and possible proton-halo) nuclei. The stable isotopes are those lying near or along the $N = Z$ line. As one travels further away from the valley of stability creating an excess of

9
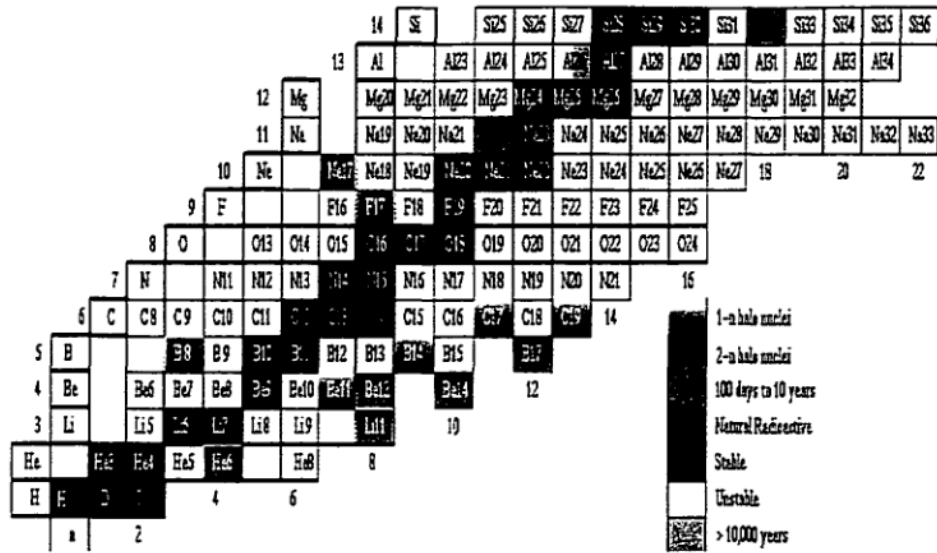
Figure 2.2. Expanded view of the very light region of the nuclide chart. Neutron and proton halo candidates are indicated by the gradient-shaded isotopes.

neutrons or protons, nuclei may β-decay (governed by the weak force) in order to "correct" the excess and achieve a more favorable ratio of neutrons to protons with minimum energy. At further distances from the valley, the difference in binding energy (see below) between neighboring isobars (nuclei with the same total number of nucleons) becomes greater than the binding energy of the last nucleon and decay by particle emission becomes possible. At this point it becomes simply impossible to add another nucleon to a system, which instead simply "falls off". This limit is called the drip line. For example, in the hydrogen isotopes, a nucleus of one proton and up to two neutrons can be formed. However, ^{4}H does not exist. The neutron drip line is then at three for a single proton. Moving to the Li isotopes, ^{9}Li with six neutrons, can be formed in a particle-stable state, but ^{10}Li cannot. However, in this case we can skip a space and form particle-stable ^{11}Li, but this seems to be the limit. No higher particle-stable isotopes of Li have been discovered. This would indicate that the neutron drip line passes through $N = 8$ for three protons. We must

10

note here that all of the elements near the drip lines have finite lifetimes, owing to the weak decay properties mentioned above. ^{3}H is rather long-lived with a lifetime around 12 years, whereas ^{9}Li and ^{11}Li have lifetimes of 180 ms and 8 ms, respectively.

Also related to the stability, or lifetime, of an isotope is its binding energy. The binding energy is the amount of missing energy in the nucleus compared to the simple sum of the energy of its constituents. That is, if we compare the mass of a system X, consisting of Z protons and electrons, and N neutrons, to the sum of the masses of its individual constituents, the difference is the binding energy

$$B = (Zm_p + Nm_n + Zm_e - m(X)) c^2 \tag{2.1}$$

with the masses given in MeV/A. A larger binding energy B implies a more tightly bound nucleus. Put another way, the absolute value of the binding energy is the energy required to break apart a nucleus into its separate constituents. Plotting the contours of the binding energy surface, $-B(N, Z)$, in Fig. 2.3, we see a surface that looks like a valley containing the most stable elements—hence the name "valley of stability". It is also found (see Fig. 2.4) that the absolute value of the binding energy per nucleon remains nearly constant at 6–8 MeV/A for stable nuclei with mass $A \gtrsim 12$.

2.1.2 Separation energies

Other parameters of interest in studying nuclear structure and stability are the neutron and proton separation energies, S_n and S_p. This is the amount of energy required to remove the last neutron or proton from the system. This is equivalent to the difference in binding energies between the original and resultant nuclei:

$$\begin{aligned} S_n &= B(_Z^A X_N) - B(_Z^{A-1} X_{N-1}) \\ S_p &= B(_Z^A X_N) - B(_{Z-1}^{A-1} X_N) \end{aligned} \tag{2.2}$$

11
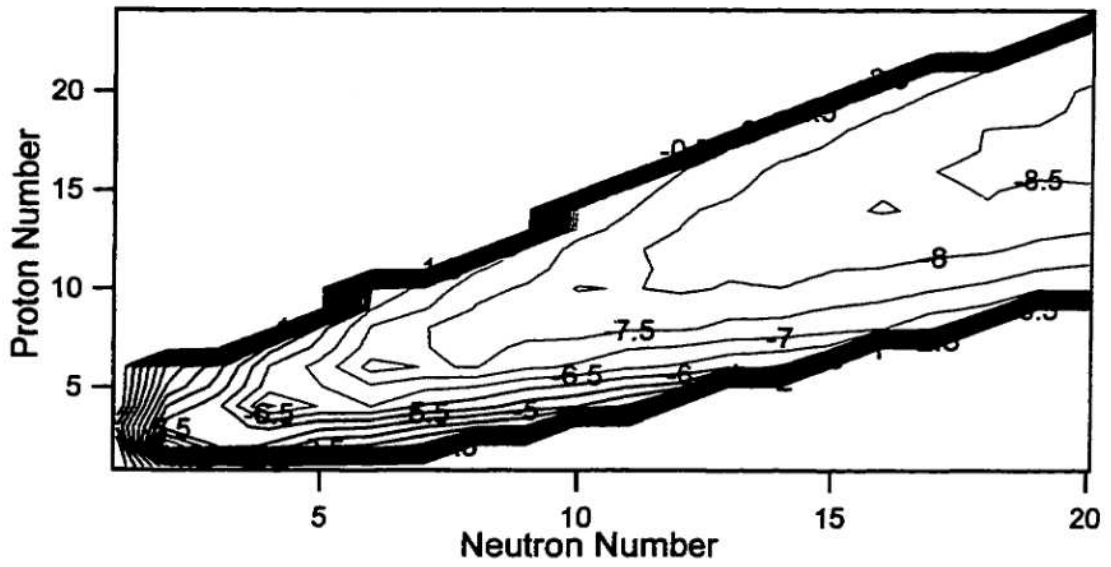
Figure 2.3. Valley of stability. The binding energy surface [26] in MeV/A.
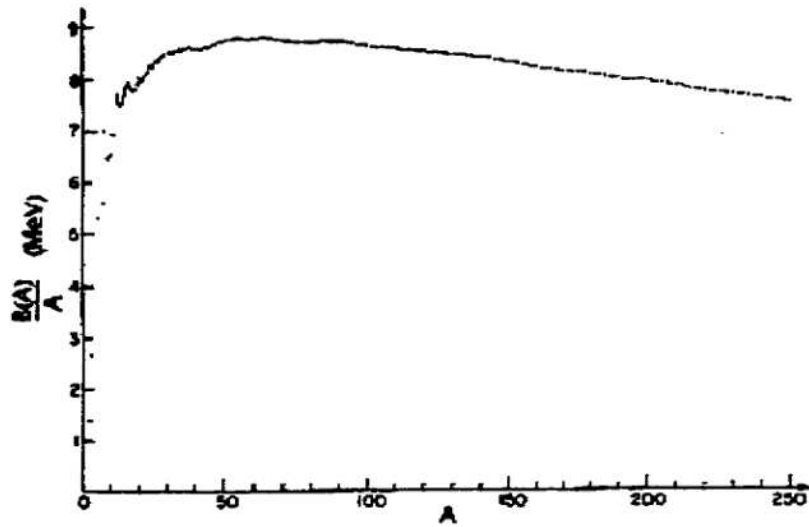
Figure 2.4. Binding energy per nucleon (Reproduced from [27])

12

We can use Eq. (2.1) to rewrite the separation energies of Eq. (2.2) in terms of masses:

$$S_n = Zm_p + Nm_n + Zm_e - m({}_Z^A X_N)$$
$$- \left[Zm_p + (N-1)m_n + Zm_e - m({}^{A-1}_Z X_{N-1}) \right]$$
$$= m_n - \left[m({}_Z^A X_N) - m({}^{A-1}_Z X_{N-1}) \right] . \tag{2.3}$$

Similarly, we find

$$S_p = m_p - \left[m({}_Z^A X_N) - m({}^{A-1}_{Z-1} X_N) \right] . \tag{2.4}$$

For some elements, the probability of removing two nucleons exceeds that of removing a single nucleon. In those cases, the two-neutron separation energy, S_{2n}, is less than S_n and is the more relevant parameter. S_{2n} is defined analogously to Eq. (2.2),

$$S_{2n} = B({}_Z^A X_N) - B({}^{A-2}_Z X_{N-2}). \tag{2.5}$$

There is an interesting feature of the separation energies that sheds some light on nuclear structure. When plotting the two-neutron or two-proton separation energies as a function of nucleon number as in Fig. 2.5, one sees rather large discrete jumps at certain "magic" numbers—2, 8, 20, 28, 50, 82, and 126 [28]. This would seem to indicate a shell-like structure as in atomic systems such that a "filled" shell would be very difficult to break up and therefore have a large neutron separation energy, whereas valence nucleons outside the filled shell would be easier to remove and thus have lower neutron separation energies. Reinforcement of the idea that a shell structure leads to greater stability is provided by the fact that the most abundant naturally occurring nuclei are related to those with proton or neutron number equal to one of the magic numbers.

13
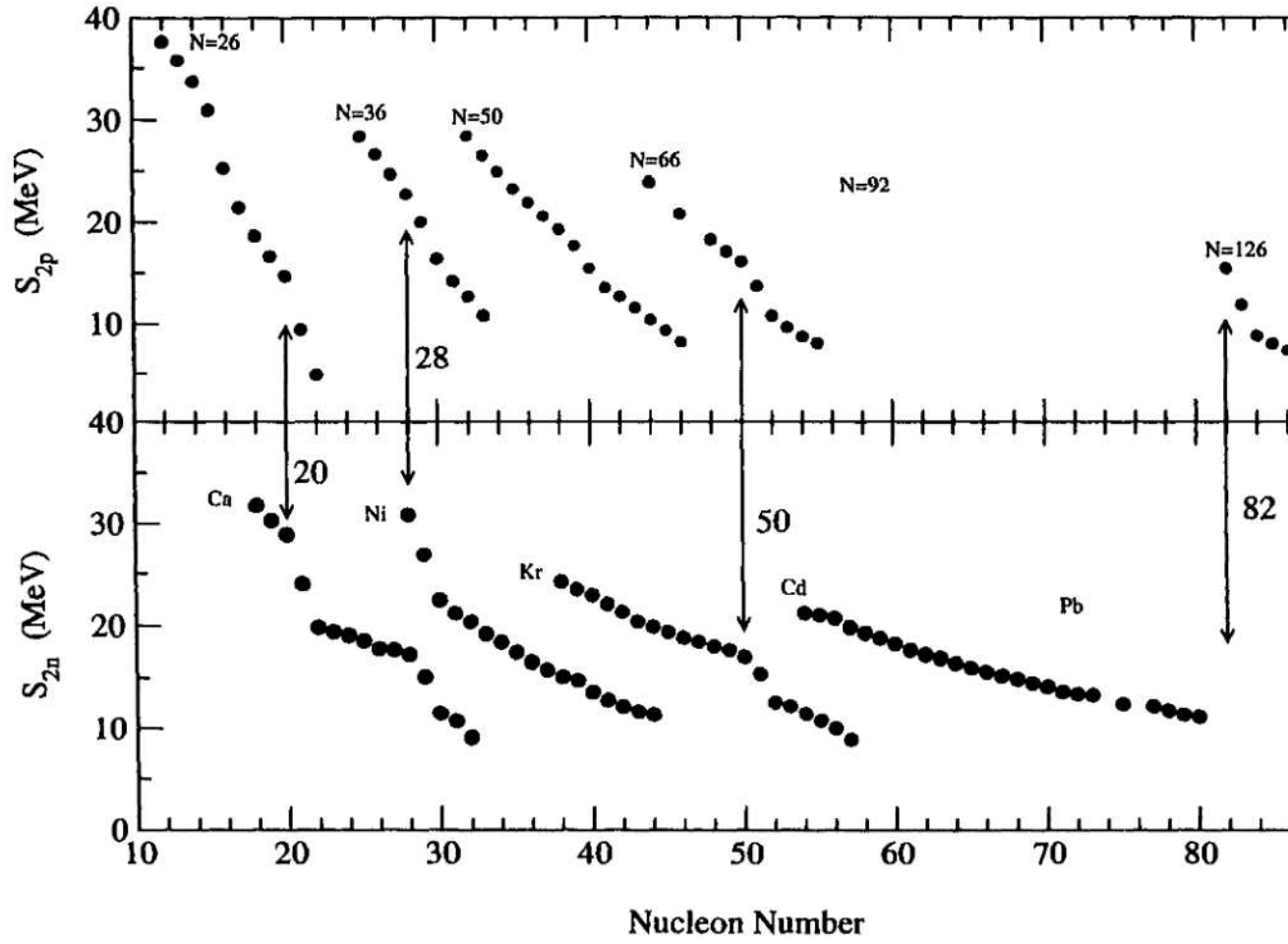
Figure 2.5. Evidence for shell structure from changes in separation energy. Note the dramatic drops in numbers, indicating a transition to a lesser-bound system. Note also the absence of drastic changes in re magic numbers. The S_{2n} are plotted for several isotopes, the S_{2p} for some isotones.

14

2.2 The shell model

One of the most basic models for interpreting nuclear structure is that of the shell model. Despite its relative simplicity, it is very successful and widely used. It is based on the idea that, just as electrons are confined to certain orbital shells, so are the protons and neutrons of the nucleus. Furthermore, there are limits as to how many nucleons may occupy any given shell. As mentioned above, there is strong motivation for a shell structure based on binding energy and nuclear abundance measurements.

Depending on the shell level configuration of the nucleons, a nucleus may be in one of several different "states"—each with a different energy. If the state is particle-stable, we consider it "bound". In order to describe the nature and energy levels of these bound states, we need a framework in which to model the nuclear structure. That is, we seek a way to describe the nuclear wave functions under a general formalism. We note that a free particle can be described by the solution to the Schrödinger equation

$$H\psi = E\psi \tag{2.6}$$

where H is the Hamiltonian and E is the energy of the particle. If the complete nuclear wave function is to be a combination of single-nucleon bound-state wave functions, we bind the entire nucleus to a single point in space through the introduction of a central potential, $V(\mathbf{r})$, that does not affect the intrinsic structure of the nucleus. That is, we can study the modified version of the Schrödinger equation

$$H'\psi = (H + V)\psi = E'\psi \tag{2.7}$$

where $V = V(\mathbf{r})$ only acts on the center-of-mass (c.m.) coordinate. E' is composed of two parts. One part, $E_{\text{c.m.}}$, is due to the kinetic energy of the motion. The

15

other part, ϵ, arises from the internal energy of the nucleus as governed by the inter-nucleon interactions. That is,

$$E' = \epsilon + E_{\text{c.m.}} \tag{2.8}$$

If V is known, then $E_{\text{c.m.}}$ is, in principle, known, and we can extract the interesting information regarding the state of the nucleus. A further advantage of binding the nucleus with a potential as in Eq. (2.7) as opposed to the free particle form of Eq. (2.6) is that the solution, ψ, is now localized with the extent of its wave function determined by the strength of the binding potential V.

We must discover an appropriate form for $V = V(\mathbf{r})$. An infinite well is not adequate for realistic modeling of the nuclear force since real nuclei do not have sharp edges. One may instead use the harmonic oscillator potential, $V(r) = \frac{1}{2}kr^2$ (which has a frequency of $\omega_0 = \sqrt{k/m}$ for a particle of mass m) which yields discrete energy levels. For a particle with angular momentum ℓ, there is a $2(2\ell+1)$-fold degeneracy in the energy level corresponding to how many nucleons may occupy it. As with the infinite well, the shape of the harmonic oscillator potential is not completely satisfactory since it implies infinite binding energy, but it provides a reasonable starting point. Figure 2.6 compares the shell levels predicted by the infinite well and harmonic oscillator potentials.

Comparing the results from this simple harmonic oscillator potential to the empirical data [28] reveals that although the "known" magic numbers 2, 6, 8, and 20 are reproduced, higher values are not very close to experiment. Clearly some refinements must be made. It was independently shown by Mayer [29] and Haxel, Jensen, and Suess [30] that by accounting for the orbital angular momentum, ℓ, and spin, s, a new potential, called the *spin-orbit* potential, can be added of the form

$$V_{\text{so}}(r) = V_{\text{so}}\, \boldsymbol{\ell} \cdot \mathbf{s} \tag{2.9}$$

16
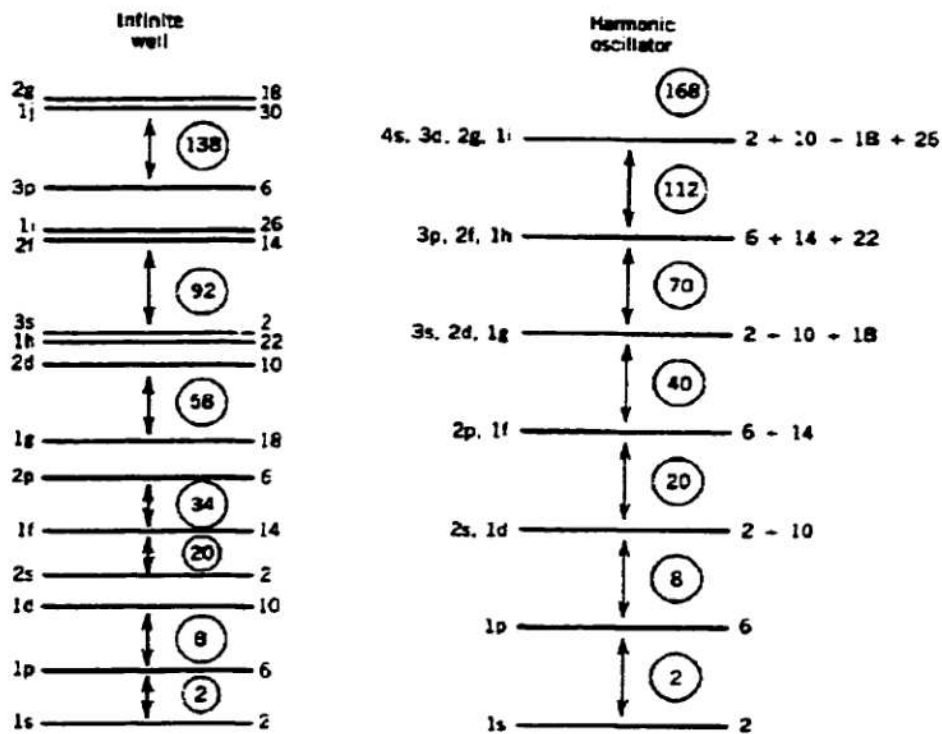
Figure 2.6. Comparison of shell levels predicted by the infinite square well and the harmonic oscillator potentials. Spectroscopic notation is used for denoting angular momentum. $(s, p, d \ldots$ for $\ell = 0, 1, 2 \ldots)$

17

The addition of the spin-orbit potential splits the degenerate levels for $\ell > 0$ in order to reproduce the observed magic numbers. Figure 2.7 illustrates the effect of adding the spin-orbit potential to the harmonic oscillator. Our simple shell model nuclear potential can then be written as

$$V(r) = V_{\text{ho}}(r) + V_{\text{so}}(r) \tag{2.10}$$

In order to more accurately describe the energy levels and spacings, an improvement over the infinite well and the harmonic oscillator is found in the Woods-Saxon potential [31] which attempts to mimic the shape of the nuclear surface,

$$V_{\text{ws}}(r) = \frac{-V_0}{1 + e^{(r-R)/a}} \tag{2.11}$$

The Woods-Saxon form allows the characterization of a nucleus by two parameters. The mean radius, R, of the matter distribution is the point at which the density falls to one-half its central value. The skin thickness, $t = 4a \ln 3$, is the region over which the density falls from 90% to 10% of its central value [31]. For the majority of nuclei, owing to the nearly constant density of nuclear matter, R is typically $1.2\sqrt[3]{A}$ (where A is the number of nucleons in the system) and $a = 0.524$ (yielding a typical skin thickness of 2.3 fm). The well depth, V_0, is empirically adjusted to obtain the measured separation energies and has typical values on the order of 50 MeV. The spin-orbit potential must also be added to the Woods-Saxon potential to obtain the experimentally determined magic numbers. The shell levels produced by this potential (with and without the spin-orbit splitting) are shown in Fig. 2.8. Our final form for the shell model potential is

$$V(r) = V_{\text{ws}}(r) + V_{\text{so}}(r) \tag{2.12}$$

18

168

$2g, 1i$ ────────

112

$3p, 2f, 1h$ ────────

70

$3s, 2d, 1g$ ────────

40

$2p, 1f$ ────────

20

$2s, 1d$ ────────

8

$1p$ ────────

2

$1s$ ────────

H.O.

126

$3p, 2f,$
$1h_{9/2}, 1i_{13/2}$ ────────

82

$3s, 2d,$
$1g_{7/2}, 1h_{11/2}$ ────────

50

$2p, 1f_{5/2}, 1g_{9/2}$ ────────

28

$1f_{7/2}$ ────────

20

$2s, 1d$ ────────

8

$1p$ ────────

2

$1s$ ────────

H.O. + S.O.
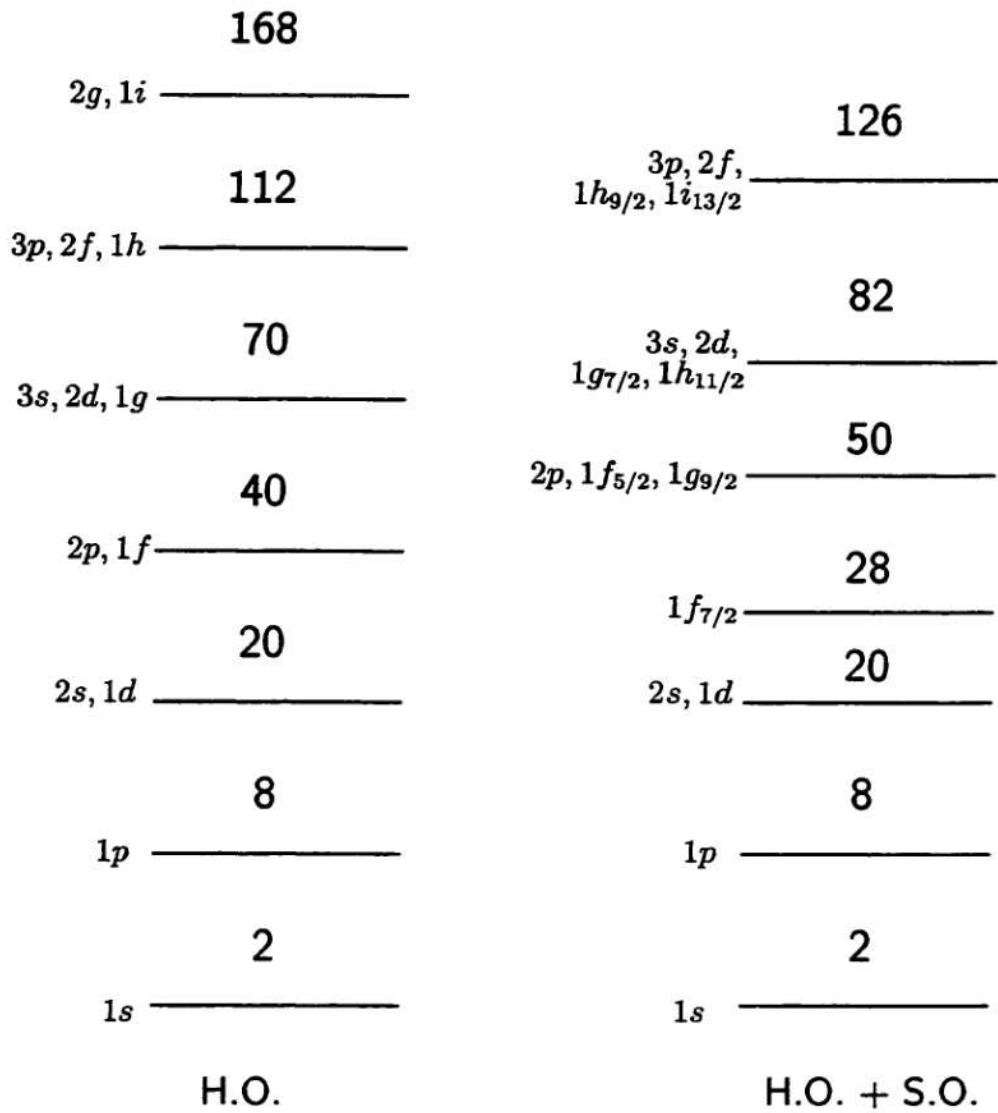
Figure 2.7. Effect of the spin-orbit interaction. On the left are the shell levels that appear from using a simple harmonic oscillator potential. The right side includes the spin-orbit effect. The number of nucleons filling each shell is also given. Angular momentum is given in spectroscopic notation $(s, p, d \ldots$ for $\ell = 0, 1, 2 \ldots)$.

19
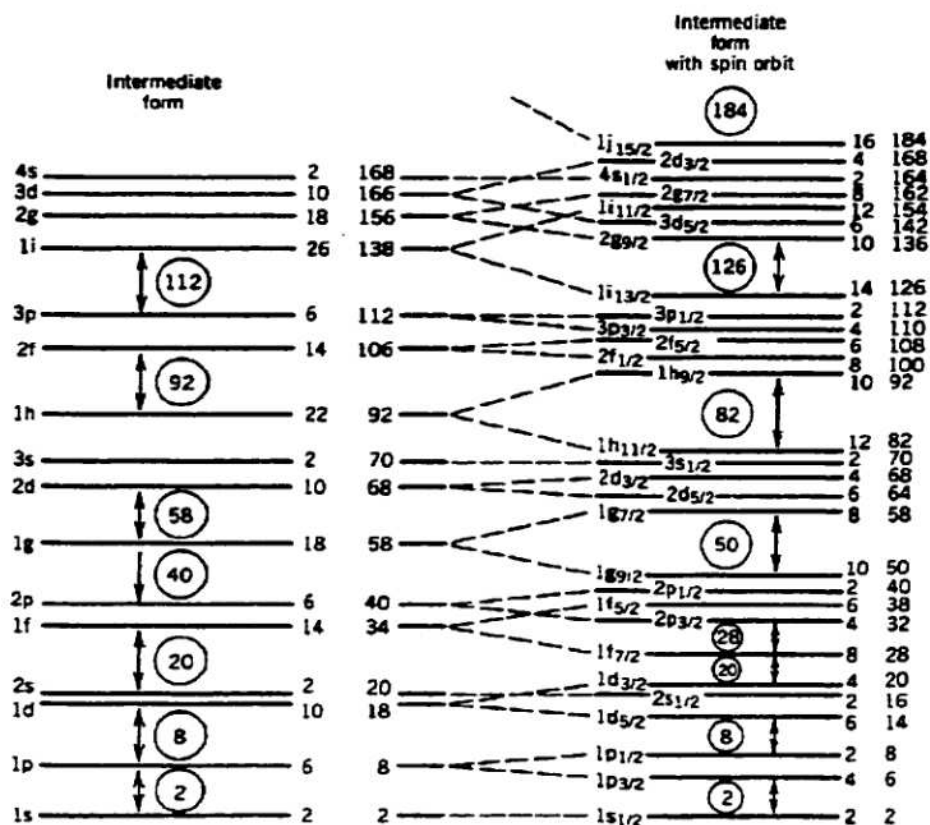
Figure 2.8. Detailed illustration of the Woods-Saxon potential with (right) and without (left) the spin-orbit interaction. (Reproduced from [31])

20

2.3 Reactions

In order to investigate the nuances of nuclear structure, we can observe how particles interact with one another. By studying the probability of a certain reaction as a function of energy or angle, or both, we learn about the potential governing the reaction, which in turn yields information about the nucleus of interest. Depending on the energy of the colliding particles, different regions of the nucleus can be probed, with Coulomb effects dominating at lower energies, nuclear effects dominating at higher energies, and their interference at energies in between. This section establishes the basics of studying these nuclear reactions, especially as they pertain to elastic scattering.

2.3.1 Cross sections

When two nuclei collide, many things can happen, each with varying probability. That probability is related to the cross section, denoted by σ. If R particles per second are emitted from the interaction of a beam with intensity I particles per second incident on N target nuclei per unit area, the cross section is given by

$$\sigma = \frac{R}{IN} \tag{2.13}$$

Generally in an experiment, one does not detect particles over all of space, but rather only that element of solid angle, $d\Omega$, available to the detector system. In this case one really measures the number of particles emitted within that solid angle, and the proportionality of Eq. (2.13) becomes the differential cross section

$$\frac{d\sigma}{d\Omega} = \frac{R}{IN d\Omega} \tag{2.14}$$

This is related to the total cross section by the expression

$$\sigma = \int_0^{2\pi} \int_0^{\pi} \frac{d\sigma}{d\Omega} \sin\theta \, d\theta \, d\phi \tag{2.15}$$

21

which, if there is no polarization present, becomes

$$\sigma = 2\pi \int_0^\pi \frac{d\sigma}{d\Omega} \sin\theta \, d\theta \tag{2.16}$$

There are two important types of cross sections noted in nuclear physics. The elastic cross section, σ_{el}, accounts for those events where the scattered particles are the same as the incident particles. The reaction cross section, σ_r, accounts for everything else, including transfer reactions and Coulomb excitation. Sometimes in the literature σ_r is called the absorption cross section and denoted σ_{abs}. The sum of the reaction and elastic cross sections yields the total cross section,

$$\sigma_t = \sigma_{el} + \sigma_r \tag{2.17}$$

2.3.2 Coulomb scattering

2.3.2.1 Elastic

Since nuclei are positively charged, the interaction between them at larger ranges in a scattering experiment is the repulsive $1/r^2$ Coulomb force. Rutherford [4] established the differential cross section for elastic Coulomb scattering as

$$\frac{d\sigma}{d\Omega} = \left(\frac{Z_1 Z_2 e^2}{4E}\right)^2 \frac{1}{\sin^4(\theta/2)} \tag{2.18}$$

where Z_1 and Z_2 are the atomic numbers of the colliding particles, e is the elementary charge, E is the bombarding energy, and θ is the scattering angle. At relativistic energies, the Rutherford cross section is modified slightly, and for particles with $Z \ll 137$ takes the form [32]

$$\frac{d\sigma}{d\Omega} = \left(\frac{Z_1 Z_2 e^2}{2E\beta^2}\right)^2 \left(1 - \beta^2 \sin^2(\theta/2)\right) \frac{1}{\sin^4(\theta/2)} \tag{2.19}$$

where $\beta = v/c$, E is now the total relativistic energy, $\gamma m c^2$, and E and θ relate to the c.m. frame.

22

2.3.2.2 Coulomb excitation

Analogous to the atomic structure of energy levels for the electrons, there exist energy levels in the nucleus. In Coulomb scattering, if the projectile has sufficient energy to approach close enough to the target nucleus, a virtual photon of energy equal to that of a nuclear level can be exchanged between the two nuclei [32]. This is referred to as Coulomb excitation, or Coulex, and results in a loss of kinetic energy, which affects the energy distribution of the outgoing scattered particles.

2.3.3 Nuclear scattering
2.3.3.1 Elastic

Contrary to the repulsive Coulomb force that governs Rutherford scattering, the nuclear force is attractive, and results in a "refractive" trajectory. These two scenarios are contrasted in Fig. 2.9 for identical scattering angles. The majority of phenomena observed in scattering experiments, if not due to Coulomb effects, are the result of nuclear interactions. Since the nuclear force is attractive and the Coulomb force repulsive, they interfere with each other. It is by studying this interference that we learn about the relative strengths and ranges for a particular reaction and gain insight into the structure of the nucleus of interest. There are many different forms of nuclear reactions including nucleon transfer, resonance scattering, the formation of compound nuclei, and elastic nuclear scattering where no rearrangement of the participating nucleons takes place.

2.3.3.2 Inelastic effects

Coulomb excitation is not the only method of raising projectile and target nucleons to excited levels in the nucleus. If the colliding nuclei come close enough to each other, and have enough relative energy between them, it is possible for one nucleus to take energy from the other via nuclear interactions to excite its constituents. This

23
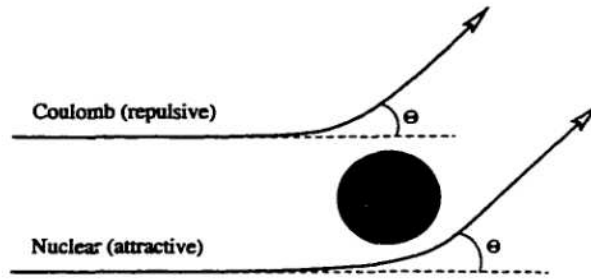
Figure 2.9. Comparison of the reaction trajectories due to the attractive Nuclear force and the repulsive Coulomb force

will be evident in the energy of the scattered particles, just as in the Coulex case.

2.3.4 Wave mechanics of scattering

Let us now turn to the quantum mechanics involved in a scattering process. We are seeking a solution to the Schröedinger equation:

$$H\psi = E\psi$$

$$\frac{\mathbf{p}^2}{2\mu}\psi + U\psi = E\psi \tag{2.20}$$

$$\frac{-\hbar^2}{2\mu}\nabla^2\psi(\mathbf{r}) + U(\mathbf{r})\psi(\mathbf{r}) = E\psi(\mathbf{r})$$

where U is the potential between two particles with an energy E corresponding to their relative motion in the center-of-momentum (c.m.) frame. We expect a solution to be of the form

$$\psi(\mathbf{r}) = \psi_i(\mathbf{r}) + \psi_s(\mathbf{r}) \tag{2.21}$$

where ψ_i represents the incident beam and ψ_s represents the scattered beam. We can represent the incident beam of particles as a plane wave,

$$\psi_i = A_0 e^{i\mathbf{k}\cdot\mathbf{r}} \tag{2.22}$$

where $\mathbf{k}$ is the wave number, related to the momentum by $\mathbf{p} = \hbar\mathbf{k}$, $\mathbf{r}$ is the vector between the projectile and target nuclei, and A_0 is a normalization constant related

24

to the incident flux of the beam. The scattered wave will be spherical, and must exhibit a $1/r$ dependence to satisfy the inverse-square law of intensities. We write it as e^{ikr}/r. At large distances, the asymptotic boundary condition [32] that the wave strongly resemble a plane wave distorted by the spherical scattering must be satisfied. Furthermore, the scattered wave need not be isotropic. In fact, this is rarely the case. Therefore the scattering wave will have an associated weighting factor to describe its angular dependence. This weighting is called the scattering amplitude and is generally given as $f(\theta, \phi)$. This leads to the general result of Eq. (2.21),

$$\psi(\mathbf{r}) \sim A_0 \left\{ e^{i\mathbf{k}\cdot\mathbf{r}} + f(\theta, \phi) \frac{e^{ikr}}{r} \right\} \qquad \text{(large } r\text{)} \qquad (2.23)$$

Given this relation of outgoing (scattered) waves to the incoming flux, we find that the differential cross section (2.14) is simply related to the scattering amplitude

$$\frac{d\sigma}{d\Omega} = |f(\theta, \phi)|^2 \qquad (2.24)$$

2.3.5 Partial waves

Since both the electromagnetic and nuclear forces are central forces, angular momentum is a constant of the motion and we can use separation of variables to break the wave function, ψ, into angular and radial parts,

$$\psi(\mathbf{r}) = g(r) Y(\theta, \phi) \qquad (2.25)$$

where $g(r)$ satisfies the radial wave equation,

$$\frac{-\hbar^2}{2\mu} \frac{1}{r^2} \frac{\partial}{\partial r} r^2 \frac{\partial}{\partial r} g(r) + \left(\frac{\hbar^2 \ell(\ell+1)}{2\mu r^2} + V(r) \right) g(r) = E \, g(r) \qquad (2.26)$$

Taking $g(r) = u(r)/r$ we obtain a more convenient form,

$$\frac{-\hbar^2}{2\mu} \frac{d^2 u(r)}{dr^2} + \left(\frac{\hbar^2 \ell(\ell+1)}{2\mu r^2} + V(r) \right) u(r) = E \, u(r) \qquad (2.27)$$

25

Equation (2.25) can be further decomposed for each particular angular momentum value ℓ (with z-component m):

$$\varphi_{\ell,m}(\mathbf{r}) = g_\ell(r)Y_\ell^m(\theta,\phi) \tag{2.28}$$

where the Y_ℓ^m are the spherical harmonics. The partial wave expansion for the complete wave function is then

$$\begin{aligned}
\psi(\mathbf{r}) &= \sum_{\ell,m} a_{\ell,m}\,\varphi_{\ell,m}(\mathbf{r}) \\
&= \sum_{\ell,m} a_{\ell,m}\,g_\ell(r)Y_\ell^m(\theta,\phi)
\end{aligned} \tag{2.29}$$

where the $a_{\ell,m}$ are determined by satisfying boundary conditions.

2.3.5.1 The scattering matrix and phase shifts

For the asymptotic condition, $r \to \infty$, the $g_\ell(r)$ of Eq. (2.29) must have the form of Eq. (2.23). For elastic scattering, this is [32]

$$g_{\ell(r)} \xrightarrow{r \to \infty} \frac{b_\ell}{r}\left[(-)^\ell e^{ikr} - S_\ell e^{ikr}\right] \tag{2.30}$$

where the b_ℓ are chosen to normalize the wave function. The S_ℓ are known as the scattering matrix. For pure elastic scattering, the amplitude of the outgoing and incoming waves must match due to conservation of particle number. However, their phase can be affected. In this case

$$|S_\ell| = 1 \quad \text{or} \quad S_\ell = e^{2i\delta_\ell} \tag{2.31}$$

and

$$\sum_\ell |S_\ell|^2 = 1 \tag{2.32}$$

26

Using Eq. (2.31) in Eq. (2.30) along with the result of Eq. (2.29) in Eq. (2.23), we find that the scattering amplitude is related to these phase shifts

$$f(\theta) = \frac{\sqrt{4\pi}}{k} \sum_\ell \sqrt{(2\ell+1)}\, e^{2i\delta_\ell} \sin\delta_\ell\, Y_\ell^0(\theta) \tag{2.33}$$

The differential cross section for elastic scattering is then

$$\frac{d\sigma}{d\Omega} = |f(\theta)|^2 = \frac{4\pi}{k^2} \left| \sum_\ell \sqrt{(2\ell+1)}\, e^{2i\delta_\ell} \sin\delta_\ell Y_\ell^0(\theta) \right| \tag{2.34}$$

where we have eliminated the ϕ dependence by taking the incident wave axis to correspond with the z-axis. The total (elastic) cross section can be obtained by integrating Eq. (2.34) over all angles. Since the Y_ℓ^0 are orthogonal, we are left with

$$\begin{aligned}
\sigma_{el} &= \frac{4\pi}{k^2} \sum_\ell (2\ell+1)\sin^2\delta_\ell \\
&= \frac{\pi}{k^2} \sum_\ell (2\ell+1)|1 - S_\ell|^2
\end{aligned} \tag{2.35}$$

where Eq. (2.31) was used to obtain the final form. Thus, the partial wave expansion and phase shifts can provide powerful insight into the interaction governing the scattering. It is even possible to work in reverse. From cross section measurements, one can determine the phase shifts, δ_ℓ, and eventually obtain the potential, $U(r)$, of the interaction [33].

2.4 Optical theorem and model

We now consider that in a scattering experiment, every particle is not elastically scattered. If particles do not elastically scatter, due to conservation of flux they must undergo some other process such as inelastic scattering or nucleon transfer. We can say those particles have been "absorbed". By making an analogy to the diffractive scattering of light through opaque spheres, which is described by the use of complex indices of refraction, we can add an imaginary term to our potential

$$U(r) = V(r) + iW(r) \tag{2.36}$$

27

It is this analogy to classical optics that leads to calling this the optical potential, sometimes referred to as the "cloudy crystal ball" model. It provides a phenomenological approach to describing the complex interactions of nuclear collisions.

The solution of a plane wave of particles with mass m and energy E traveling along the z-axis in this potential is

$$\psi = e^{(ikz)} \qquad k = \sqrt{2m(E - U)/\hbar^2}$$

as found before. However, since U is now complex, so is k. If we write $k = k_r + ik_i$, ψ becomes

$$\psi = e^{i(k_r + ik_i)z}$$
$$= e^{-k_i z} e^{ik_r z}$$

with density

$$|\psi|^2 = e^{-2k_i z}$$

so that the wave is damped proportionally to the strength of the imaginary part of the potential.

Taking the terms on the right hand side (r.h.s) of Eq. (2.36) to be proportional to the nuclear density, they are of the Woods-Saxon form of Eq. (2.11) to follow more closely the actual nuclear shape. We then write

$$U_{\text{vol}}(r) = \frac{-V_0}{1 + e^{(r_v - R_v)/a_v}} + i \frac{-W_0}{1 + e^{(r_w - R_w)/a_w}} \tag{2.37}$$

where $R_v \approx R_w \approx 1.2 A^{1/3}$ are the mean radii of the real and imaginary potentials. The depth and surface diffuseness of the real (imaginary) potential are then given by V (W) and a_v (a_w). This provides six adjustable parameters. In practice it is further determined that absorption reaction channels are often surface-peaked,

28

especially at lower energies. In this case an additional imaginary term is added to the optical potential to mimic that of a surface absorption:

$$U_{sur}(r) = iW_D(r) = i\frac{d}{dr}W$$
$$= i\frac{-W_0 e^{(r-R_w)/a_w}}{a_w\left(1 + e^{(r_v-R_v)/a_v}\right)^2} \qquad (2.38)$$

where the subscript D reminds us that this term comes from a derivative of the volume potential. From Fig. 2.10, which compares the Woods-Saxon volume and surface potential shapes, one can readily see that the surface potential is rather well-localized in space with a width that is directly related to the diffuseness of the nuclear surface. Ignoring spin-orbit forces then provides us with the basic optical potential

$$U_{opt}(r) = U_{vol}(r) + U_{sur}(r)$$
$$= V(r) + i\Big(W(r) + W_D(r)\Big) \qquad (2.39)$$

To see the results of scattering from a complex potential such as this we revisit the partial wave expansion and the S-matrix. In deriving the elastic results above, the exit and entrance channels were identical and the S-matrix was diagonal with S_ℓ pertaining to the ℓth partial wave. However, the more general form of the S-matrix relates all possible reaction channels. If we denote our initial system of a projectile and target $(a + A)$ by α, and denote the final system of scattered particle and residual nucleus $(b + B)$ by β, we then write $S_{\alpha,\beta}^\ell$ to represent the scattering. Obviously we recover the elastic results with $\alpha \equiv \beta$. Then the unitarity condition of Eq. (2.31) is the sum over all possible exit states,

$$\sum_\beta |S_{\alpha,\beta}^\ell|^2 = 1 \qquad (2.40)$$

or, looking at only the inelastic channels,

$$\sum_{\beta \neq \alpha} |S_{\alpha,\beta}^\ell|^2 = 1 - |S_{\alpha,\alpha}^\ell|^2 \qquad (2.41)$$

29
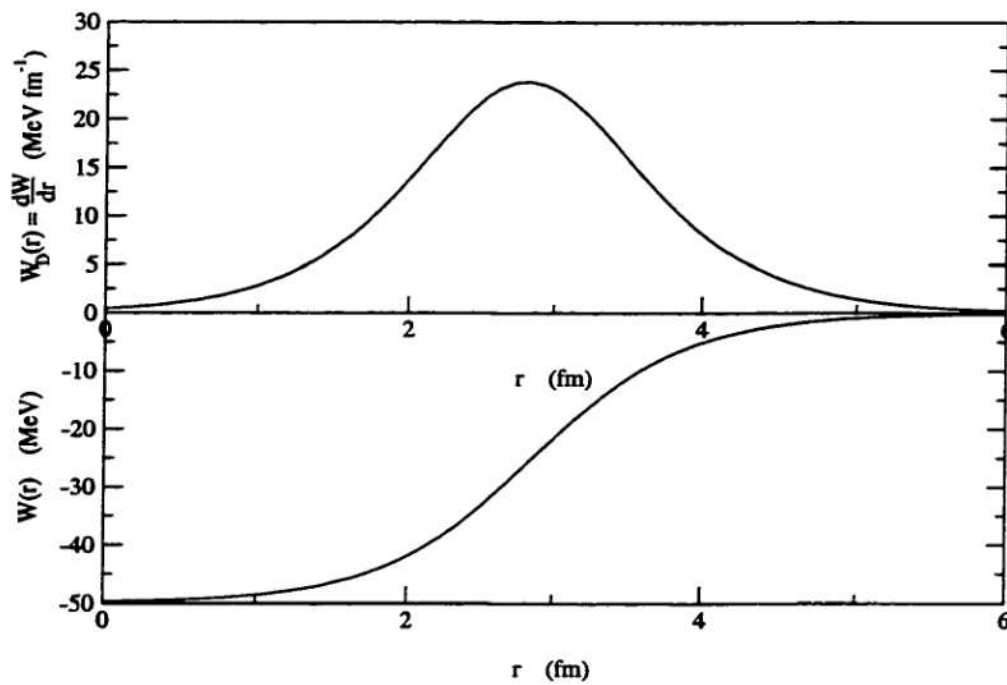
Figure 2.10. Comparison of the volume (bottom) and surface (top) Woods-Saxon form potentials. The parameters used were $W = 50\,\mathrm{MeV}$, $R = 1.25\sqrt[3]{12}\,\mathrm{fm}$, and $a = 0.524\,\mathrm{fm}$

30

By analogy with Eq. (2.35), we write the reaction cross section as

$$\sigma_r = \frac{\pi}{k^2} \sum_\ell (2\ell + 1)(1 - |S_{\alpha,\beta}^\ell|^2) \tag{2.42}$$

Finally, we obtain the partial wave expansion for the total cross section,

$$\begin{aligned}
\sigma_{tot} &= \sigma_{el} + \sigma_r \\
&= \frac{\pi}{k^2} \sum_\ell (2\ell + 1) \left[|1 - S_{\alpha,\beta}^\ell|^2 + 1 - |S_{\alpha,\beta}^\ell|^2 \right] \\
&= \frac{\pi}{k^2} \sum_\ell (2\ell + 1) \left[1 - \mathrm{Re} S_{\alpha,\beta}^\ell \right]
\end{aligned} \tag{2.43}$$

2.5 Halo structure and signatures

The halo phenomenon is one of the most beautiful results of quantum mechanics. In fact, we can look directly to quantum theory and the wave equation to learn something about the origins of the halo structure. We follow the discussion of Tanihata [8]. For simplicity, take the interaction potential of a square well,

$$V(r) = \begin{cases} -V_0 & \text{for } r < R \\ 0 & \text{otherwise} \end{cases} \tag{2.44}$$

and consider the state with no angular momentum, $\ell = 0$. Outside the potential the wave function of the last bound neutron ($E < 0$) is [34]

$$\psi(r) = \left(\frac{2\pi}{\kappa}\right) \left(\frac{-e^{\kappa r}}{r}\right) \left[\frac{e^{kR}}{(1 + kR)^{1/2}}\right] \tag{2.45}$$

Furthermore, the neutron density distribution outside the potential is

$$\begin{aligned}
\rho(r) &= |\psi(r)|^2 \\
&= \frac{4\pi^2}{\kappa^2} \frac{e^{-2\kappa r}}{r^2} \frac{e^{2kR}}{1 + kR}
\end{aligned} \tag{2.46}$$

In the above equations the wave number outside the potential, κ, is related to the neutron separation energy E_s by:

$$\hbar\kappa = \sqrt{2\mu E_s} \tag{2.47}$$

31
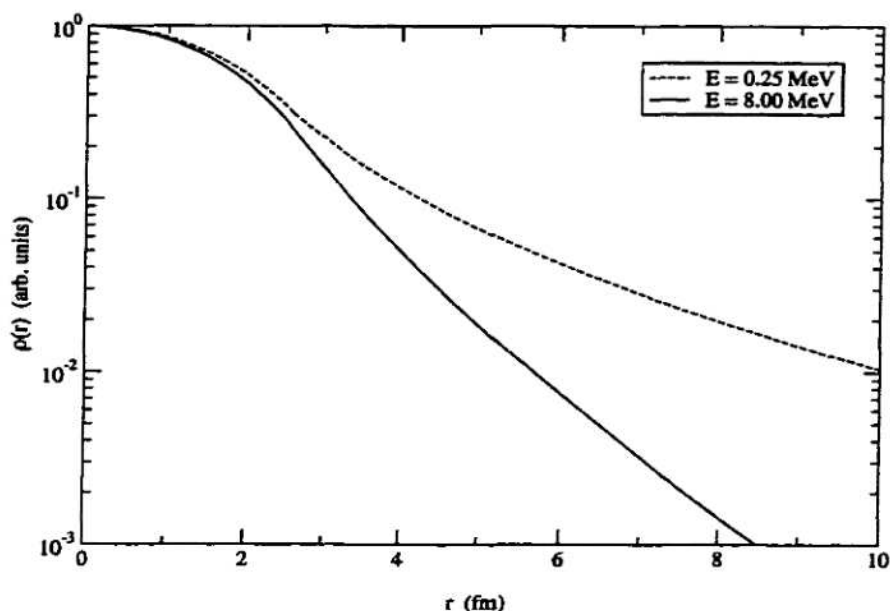
Figure 2.11. Comparison of neutron densities for a normally bound (solid curve) neutron (8 MeV) and a weakly bound (0.25 MeV) "halo" neutron (dashed curve)

and the wave number inside the potential, k, is given by

$$\hbar k = \sqrt{2\mu(E + V_0)}. \tag{2.48}$$

Clearly κ determines the slope, and hence extent, of the density tail. It is also readily apparent from Eq. (2.47) that as the separation energy decreases, so does κ, and the tail of the wave function grows. This extended tail of the distribution is called the "halo". Therefore the onset of the halo phenomenon can be associated with very weak binding of the last one or two nucleons, though that is certainly not the only requisite of a true halo system. Fig. 2.11 contrasts the density distributions for a normally bound neutron($S_n = 8.0\,\text{MeV}$) to that of a weakly neutron ($S_n = 0.25\,\text{MeV}$) such as that of ^{11}Li. Table 2.2 lists the single neutron and neutron pair separation energies of the strongest neutron-halo candidates compared to some

32

Table 2.2. 1n and 2n separation energies of some neutron-halo and normal-bound nuclei (values from [13])

Element	A	S_n (keV)	S_{2n} (keV)	Halo?
He	4	20578	–	no
	6	1863	973	$2n$
	8	2583	2138	$4n$
Li	6	5664	27376	no
	7	7250	12913	no
	9	4064	6096	no
	11	326	300	$2n$
Be	9	1665	20564	no
	11	504	7316	$1n$
	14	1847	1336	$2n$
Fe	56	9298	20496	no

"normal", stable isotopes. One can see that the halo candidates, as expected from these simple arguments, have small separation energies on the order of 1 MeV. One further comment should be made regarding these halo nuclei. The halo nucleons are all in $\ell = 0$ or $\ell = 1$ angular momentum states, with the most pronounced halos in the $\ell = 0$ configuration. The absence of a centrifugal barrier does not restrict the wavefunction, allowing it to extend further into space.

Besides a small separation energy of the valence neutron, there are other related measurements that can indicate the presence of a halo. If the halo neutron really does occupy a large spatial range, then the Heisenberg uncertainty principle for momentum,

$$\Delta p \, \Delta x \geq \hbar, \tag{2.49}$$

tells us that the momentum of these halo particles should have a narrow distribution. There have been measurements of both transverse and longitudinal momentum distributions of the halo neutrons emitted from dissociation of several of

33
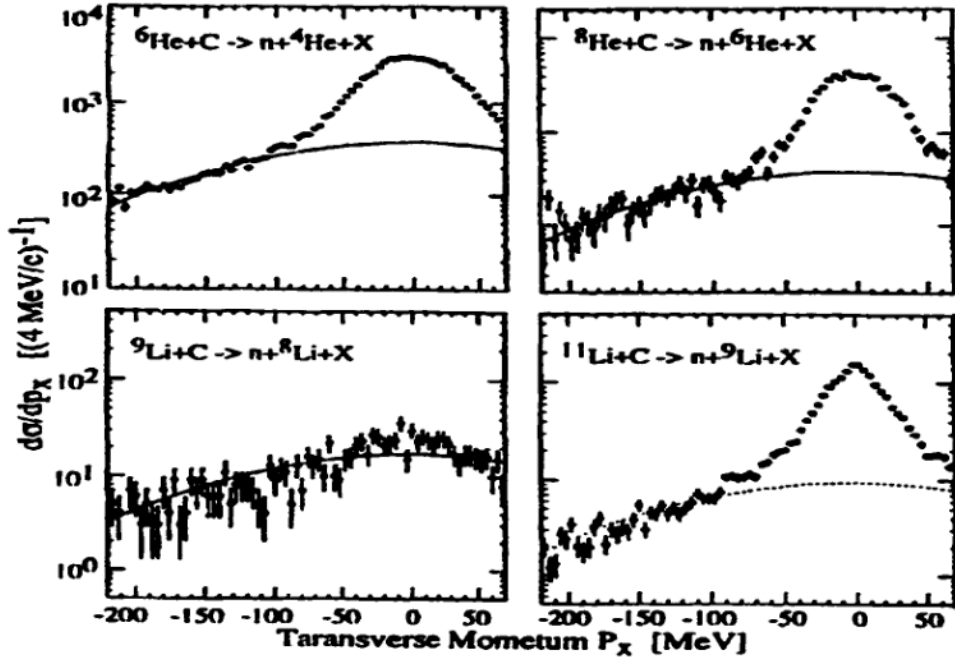
Figure 2.12. Transverse momentum measurements of ^{6,8}He and ^{9,11}Li at 790 MeV/A. The normally bound nucleus ^{9}Li only shows a broad component consistent with diffraction but the exotic halo candidates exhibit an enhanced narrow peak as well. (Taken from [8])

these halo candidates, as well as the corresponding momentum distributions of the underlying cores. Figure 2.12, taken from [8], shows the transverse momentum distributions of the neutrons for several nuclei at an incident energy per nucleon of 790 MeV/A. Every spectrum has a broad component consistent with standard diffractive breakup. For the non-halo nucleus ^{9}Li (lower left), this broad component is the sole feature. However, the other nuclei show a huge enhancement with a narrow width consistent with what may be expected from simple uncertainty arguments (≈ 20 MeV/c for $\Delta x = 10$ fm).

Another signature of a halo nucleus that is also due to its extended wave function is a large cross section. As discussed in §2.3.1, the cross section for a reaction

34
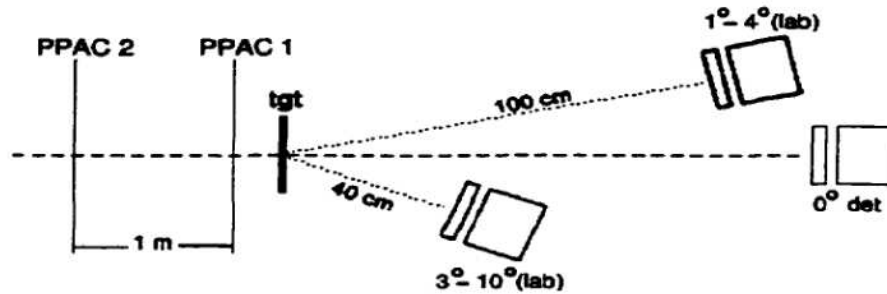
Figure 2.13. The experimental setup used in the 1992 elastic scattering experiment by Kolata consisted of two PPACs upstream for tracking the beam onto the target as well as Si-CsI telescopes for identification of the scattered particles. The 0° telescope used for monitoring beam purity and intensity was moved out of the way for runs with high beam intensities.

is related to its probability of occurrence. Classically one can imagine that with a larger projectile, there is a better chance of hitting a target and interacting. Quantum mechanically, with an extended wave function there is more opportunity for the wave functions of the halo nucleus and the scatterer to overlap.

2.6 Prior elastic scattering studies of ^{9,11}Li

Elastic scattering is an important tool for learning about basic nuclear structure and how particles interact. To probe the structure of ^{11}Li, Kolata et al. studied the elastic scattering of ^{11}Li$+^{12}$C at 60 MeV/A in 1992 [16]. Given the model of ^{11}Li as ^{9}Li$+n+n$, they also studied the elastic scattering of ^{9}Li$+^{12}$C in hopes of learning about the different natures of the core and halo of ^{11}Li.

2.6.1 Setup and measurements

The setup used in that experiment is depicted in Fig. 2.13. Due to the large divergence inherent to secondary beams produced via fragmentation, a common technique to improve the angular resolution of the scattering is to track the beam to the target on an event-by-event basis. This was accomplished through the use of

35

two Parallel Plate Avalanche Counter (PPAC) detectors.

Due to limitations of the telescope detectors, their experiment was unable to separate the pure elastic contribution from the inelastic excitations of the target or projectile. Therefore the measured data are really quasi-elastic scattering, and the analysis relied upon modeling to deduce the true elastic cross section and angular distribution. The results, obtained using a potential by Tostevin [16], for ^{9}Li are given in Fig. 2.14. The angular distribution appears to be fairly well-understood. Using that potential as the core of the ^{9}Li $+ n + n$ system, and folding the neutron interactions into the potential yields the result shown in Fig. 2.15. It is readily apparent that even though the agreement at large angles is reasonable, there is a huge mismatch at forward angles between the data and the calculations. This has led to a bevy of questions and speculation, some of which were mentioned in the introduction (§1.1.4) and some of which will be discussed in the following section.

2.6.2 Implications

The primary problem to be resolved from the previous experiment regards the far-forward angles. It must be determined whether there a problem with the data or with the modeling method used in the analysis. The method of extracting the individual contributions from the ground state as well as excited states of the ^{12}C target is completely model-dependent, and is only as good as our understanding of the excitation probabilities and processes. There is some confidence that this method is at least approximately right because of the success with the ^{9}Li data. There is some question regarding the reliability of the data at these forward angles. For the innermost detector (1° lab), there is the possibility that some fringe of the direct beam struck the detector and was not fully accounted for, yielding a false high cross section for the forward angles. Another possible difficulty with the data is with the

36
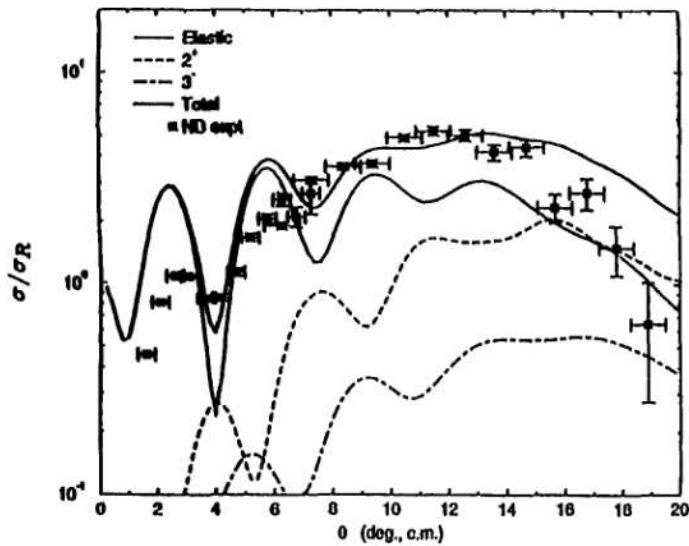
Figure 2.14. Quasi-elastic ^{9}Li data of the 1992 experiment. Also shown are the expected contributions from inelastic scattering processes as well as the pure elastic.
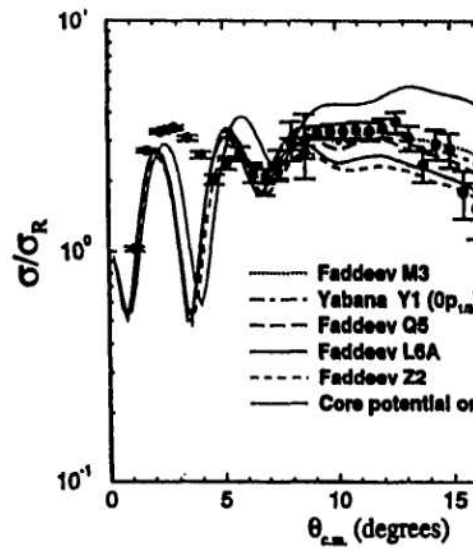
Figure 2.15. Quasi-elastic ^{11}Li data fr... iment. The various curves represent d... folding the valence neutrons with the ^{9}... from Fig. 2.14

determination of the far-forward angles. Since the masses of the projectile and target are roughly equal, the relationship between center-of-mass angles and lab angles is approximately 2:1. Thus, from the experimental configuration (Fig. 2.13), there is no direct way of measuring angles less than 2° c.m. Smaller scattering angles were deduced by using the tracking information. However, it must be remembered that the ^{9}Li data, analyzed with the same techniques, though not in perfect agreement with the models at forward angles, still exhibit the interference minimum expected near 4°.

With no clear answer to this dilemma to be found from the details of the experiment or the analysis methodology, we look to other possible theoretical explanations. The first minimum around 4°c.m. arises due to interference between the near and far-side scattering in the optical model calculations performed in the analysis of the existing data. Mermaz [25], however, performed a purely phenomenological analysis of the data, and found parameters that provided a reasonable fit, as shown in Fig. 2.16. However, even though the fit appears reasonable, the resulting parameters, which are listed in Table 2.3, do not. There are several odd features to the fit. Among the exotic features are extremely large values of the radius, r_0 and diffuseness, a_0, of the real part of the potential, both of which are greater than 1 fm. Perhaps the most esoteric feature is the addition of a real surface term. For comparison, the parameters of Tostevin used in the Kolata analysis are also provided in Table 2.3. As indicated in the discussion of the optical model (§2.4), the imaginary part of the optical potential is responsible for removing flux from the elastic channel, and generally those interactions are considered to occur at the surface of the interacting nuclei. Thus, surface-type potentials are often added only to the imaginary portion of the complete potential. Besides the oddity of simply having a real surface potential, the form of that potential is also very odd, with

38
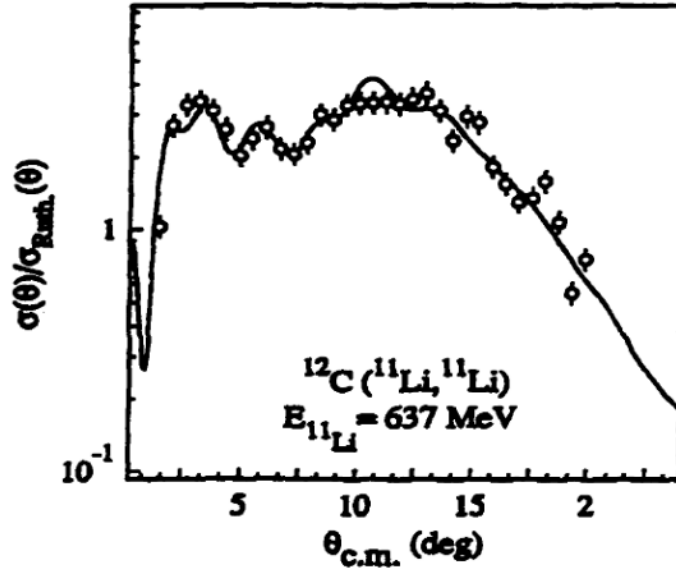
Figure 2.16. Phenomenological fit of Mermaz

Table 2.3. Comparison of optical model parameters. The parameters of Tostevin correspond to those used in the analysis of [16]. The column labeled Mermaz 1 lists the parameters obtained in [25] using only volume terms for the real (V) and imaginary (W) parts. The final column, Mermaz 2, lists the parameters for the best fit of [25], as shown in Fig. 2.16

	Tostevin	Mermaz 1	Mermaz 2
V (MeV)	120.000	40.000	40.000
r_0 (fm)	0.700	0.810	1.015
a_0 (fm)	0.900	1.907	1.055
W (MeV)	25.000	25.090	20.730
r_i (fm)	0.980	1.226	1.077
a_i (fm)	0.750	0.396	0.457
V_s (MeV)			2.260
r_{0s} (fm)			1.950
a_{0s} (fm)			1.201
W_s (MeV)			1.180
r_{is} (fm)			1.646
a_{is} (fm)			0.544

39

r_0 nearly 2 fm, and a_0 still greater than 1 fm. Visual examination of the shape of the Mermaz potential further illustrates its exotic nature. Figure 2.17 shows the real and imaginary parts of the more traditional Tostevin potential in contrast to the more esoteric Mermaz potentials of [25]. For the Mermaz potentials, the first potential, which only uses volume terms for the real and imaginary parts, is drawn with dashed lines while the complete potential that provided the best fit (shown in Fig. 2.16) is drawn with solid lines. Figure 2.17 also indicates the location of the rms radii [8] of the ^{9}Li core, the ^{11}Li system, and the n halo for reference. Three features are immediately apparent: first, the imaginary part of the Mermaz potential falls to zero very quickly compared to the more traditional Tostevin potential; secondly, the real part remains considerable even at radii beyond the neutron halo; and finally, the real shape is quite shallow.

There has also been another attempt to explain the far forward angle data of [16]. Cooper and Mackintosh [21] analyzed the ^{11}Li + ^{28}Si data of Lewitowicz [17] through the method of inversion [33] and applied that method to the 1992 data of Kolata. Similar to the results of Mermaz, they also found that the real potential required a rather long tail, extending beyond 10 fm. The Cooper potentials, however, also featured some structure near the surface of the ^{9}Li core ($\approx$ 3 fm). The imaginary potential also had a hump near the halo surface around 6 fm.

Those studies provide yet further evidence that there is some interesting and bizarre behavior of ^{11}Li that continues to elude explanation. Traditional models such as that of Tostevin fail to describe the forward angle quasi-elastic data. Optical potential parameters determined through inversion of the scattering matrix yield results consistent with those found from purely phenomenological methods, yet both methods lead to extremely exotic potentials, whose meaning is not completely understood.

40
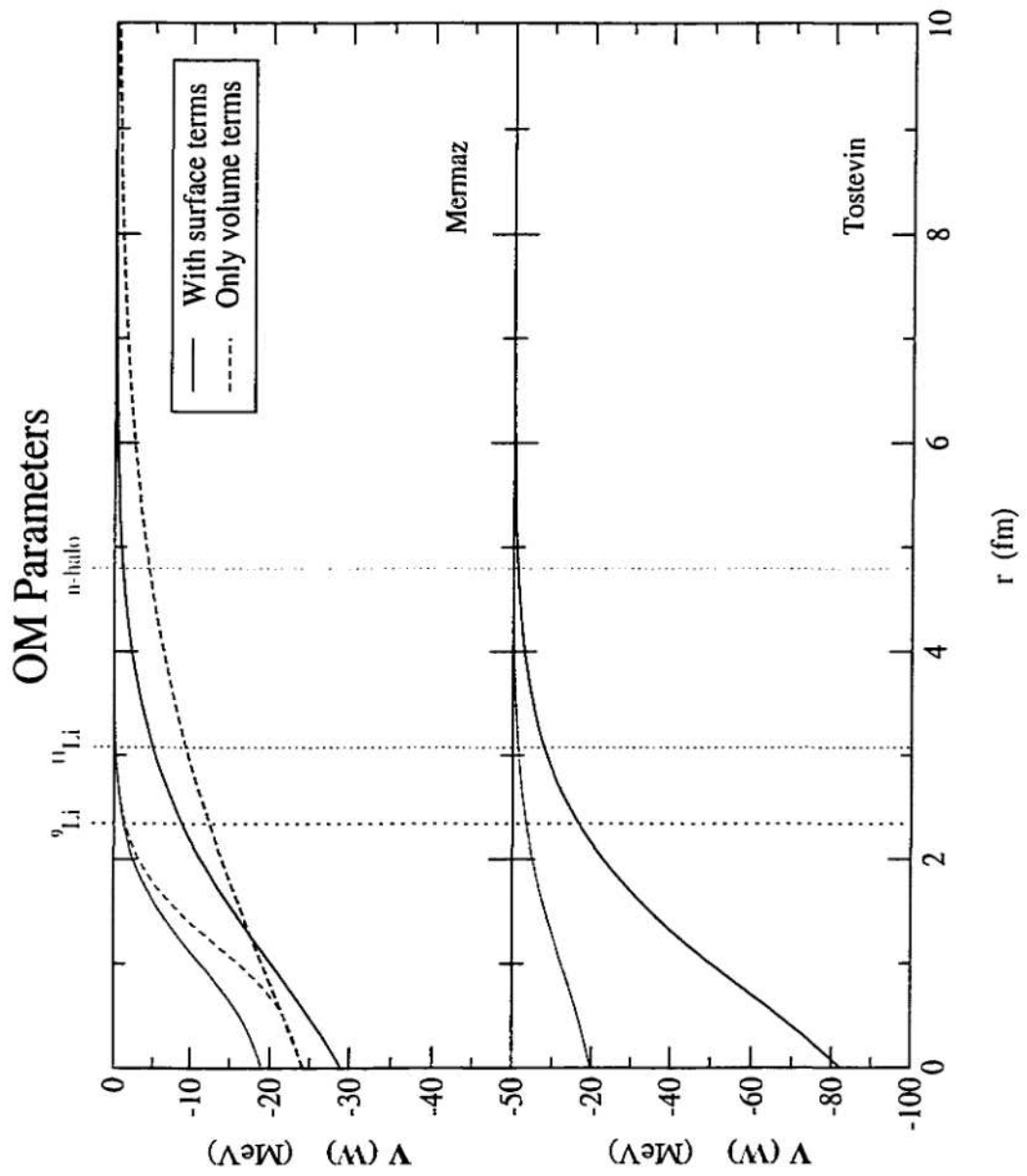
Figure 2.17. Comparison of the phenomenological potentials of Mermaz with the theoretical potential of Tostevin

41

2.6.3 The next step

With the ambiguity of data versus theory and pure theory versus phenomenology, further study is required. To further understand the nature of ^{11}Li, a new experiment must meet several criteria:

High angular resolution at forward angles Only by accurately measuring very forward angles to a high degree of accuracy to explicitly map the region of the expected interference minimum can the question of the prior measurement's reliability be resolved. From Fig. 2.15 one sees that this amounts to roughly 0.5–$1.0°$ in the c.m. system which, for particles of nearly equal mass, translates to 0.25–$0.50°$ in the laboratory.

Good energy resolution at all angles To eliminate the model-dependencies inherent in quasi-elastic studies, it is necessary to cleanly separate the ground state from other channels. For 60 MeV/A ^{9}Li, this amounts to an energy resolution of one part in 240 for the first excited state of ^{9}Li (^{12}C). At larger angles, where the inelastic cross sections are expected to be nearly as strong as the elastic, this energy resolution is crucial.

Good statistics To reduce statistical errors, it is necessary to acquire a significant amount of data over the course of the experiment. This requires reasonable beam intensities.

It should be at the same energy as the previous quasi-elastic study Since the interaction between particles is energy-dependent and the cross section varies with energy, it is important to reproduce as closely as possible the 60 MeV/A data.

42

The S800 Spectrograph [35] at Michigan State University (MSU) seems to be tailor-made for this new experiment. The S800 was designed to provide a maximum energy resolution of $1/10,000$ and an angular resolution of $2\,\mathrm{mr} \approx 0.1°$ in the lab. These specifications, of course, are for well-defined and well-behaved incident beams. One would expect marginally worse parameters for a radioactive beam such as ^{9,11}Li, but with more than an order of magnitude of leeway for the energy resolution, and a factor of 5 leeway for angular resolution it looks quite promising. The A1200 mass fragment separator [36] has proven capable of producing the required intensities of beams at the energies required for this experiment. The final criterion of running at the same energy is marginally met with the S800. The spectrograph can bend particles with a maximum rigidity of $4.0\,\mathrm{T \cdot m}$. ^{11}Li at an energy of 60 MeV/A has a magnetic rigidity of $4.15\,\mathrm{T \cdot m}$. To meet the boundary of S800 acceptance of $4.0\,\mathrm{T \cdot m}$ would require 56 MeV/A ^{11}Li. However, since this experiment was just the second experiment performed with the S800 Spectrograph and the full operating parameters were not well-understood, upon the advice of the S800 designers it was decided to run at the slightly lower energy of 50 MeV/A, corresponding to magnetic rigidities of 3.1 and $3.75\,\mathrm{T \cdot m}$ for ^{9}Li and ^{11}Li respectively. This avoids taxing the S800 magnets and their power supplies, reducing the chance of a mechanical or electrical failure such as a quench.

43

CHAPTER 3

Experimental technique

3.1 Beam preparation

The Li beams were produced by impinging a primary 80 MeV/A $^{18}O^{(6+)}$ beam of approximately 150 pnA from the K1200 cyclotron at Michigan State University (MSU) onto a ^{9}Be target and analyzing the fragmentation products with the A1200 fragment separator [36] operated in its high acceptance mode. The A1200 is illustrated in Fig. 3.1.   After fragmentation in the Be target, particles with the same momentum to charge ratio, p/q, are selected by the first pair of dipoles followed by a pair of slits as described below. At the first dispersive image, they pass through a thin timing scintillator described in §3.4.3. An aluminum achromatic wedge is located at the second dispersive image. The wedge is used to purify the beam of interest. Particles of charge q and mass m, moving at velocity v through a magnetic
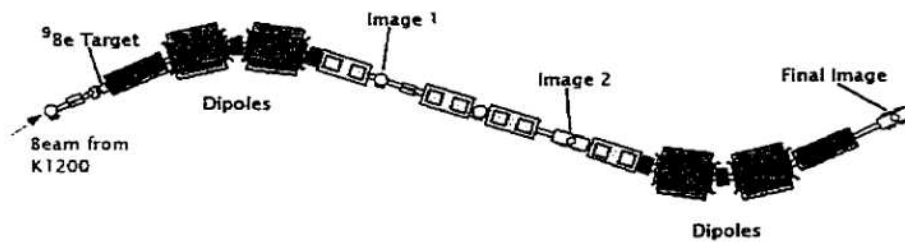
Figure 3.1. The A1200 mass fragment separator. The beam enters at the left from the K1200 cyclotron. The 1st pair of dipoles selects $B\rho = p/q$; after passing through an Al degrader at the second image, the 2nd pair of dipoles select m/q.

44

field of strength B will travel in an arc described by by the simple relation

$$\rho = \gamma \frac{m}{q} \left(\frac{v}{B} \right). \tag{3.1}$$

The primary beam is very energetic, which means all of the fragments exit the target with essentially the beam velocity so that v can be treated as constant. Furthermore the dipoles have a steady magnetic field, leaving the mass to charge ratio, m/q, as the only dependence in Eq. (3.1) for selecting particles that survive through the dipoles. Since many fragments may have approximately the same m/q, a further step is necessary to obtain a pure beam. A particle of charge ze passing through matter will lose energy by an amount given by the Bethe-Bloch formula [37]:

$$\frac{dE}{dx} = \frac{4\pi z^2 e^4}{m_e v^2} nZ \left[\ln \frac{2m_e v^2}{I} - \ln \left(1 - \beta^2 \right) - \beta^2 - C_k \right], \tag{3.2}$$

where $v \equiv \beta c$ is the velocity of the incident particle. The electron charge and rest mass are given by e and m_e. Z is the atomic number of the stopping material, with n atoms per unit volume. I is an empirical parameter related to the mean excitation energy of the atomic electrons and C_k is a correction term applicable at low energies. From inspection of Eq. (3.2) it is readily apparent that the energy loss depends most strongly on the nuclear charge of the incident particle, which allows the degrader to separate atomic species. Note also that the amount of energy loss is also directly proportional to the thickness and density of the material and inversely proportional to the incident energy. This fact can be used to a design advantage by selecting a degrader shape that will transmit the beam optimally for our purpose. Making the Al degrader wedge-shaped rather than homogeneous maintains the achromaticity of the fragment separator optics [38]. That is, by having the more energetic particles pass through the thicker section of the degrader, the condition of final beam position and angle (after the second pair of dipoles) being independent of incident momentum is maintained. This allows the second pair of dipoles to act as an isotope filter. Slits

45

at the final image clean up the beam "halo" for further transport. This technique provided us with beam purities of $> 99.4\%$ for both ^{9}Li and ^{11}Li, with intensities of approximately 5000 pps and 100 pps respectively.

3.2 Target preparation

For this experiment, the targets were graphitic natural C (99% ^{12}C) of thickness 178 mg/cm^2 and 890 mg/cm^2, with respective purities of 99.95% and 99.5+%. The targets were examined for non-uniformites by measuring the physical thickness at several points across the face with a calipers. The thinner target was used for data taken with the S800 at 0° relative to the beam line. The thicker target was used with the spectrograph at an angle of 5° to the incident beam line. The cross section falls off rapidly at larger angles, and a thicker target was needed to achieve useful count rates.

Energy loss and multiple scattering calculations were performed using the program **STOPX** [39]. The results for both beams and targets are summarized in Table 3.1. We found that, for the 178 mg/cm^2 target, the energy resolution would not be a factor, and the multiple scattering would have a relatively small effect. For the 890 mg/cm^2 target, we are at the limit of cleanly separating the contributions of the first excited state of the ^{9}Li projectile from the ground state. The extra uncertainty in scattering angle introduced by multiple scattering in the thicker target is not an issue at the larger angles for which this target was used, since large angular bins are necessary for obtaining meaningful statistics.

3.3 The S800 vault

Fig. 3.2 shows the S800 Spectrograph in its entirety, including the analysis line as well as the dipoles. The beam enters from the left and is transported achromatically

46

Table 3.1. Energy and angular resolutions (FWHM) due to energy straggling and multiple scattering in the targets used.

Target	^{9}Li		^{11}Li	
	E(MeV)	θ(mr)	E(MeV)	θ(mr)
178 mg/cm^2	1.23	8.2	1.31	6.7
890 mg/cm^2	2.74	19.8	2.91	15.9
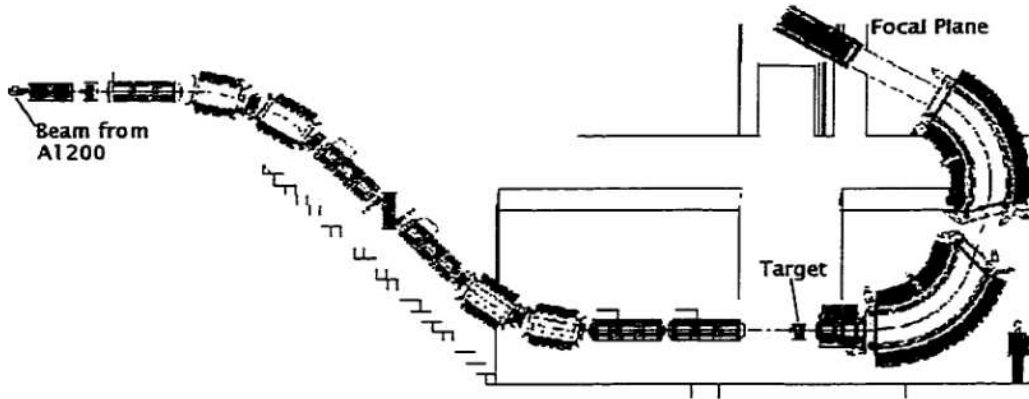
Figure 3.2. The S800 vault. Both the analysis beam line and the spectrograph itself are shown. A person is drawn to scale at the base of the first dipole.

through the analysis line, coming to a dispersed focus at the target. The importance of dispersion matching is discussed in §3.5. Finally the beam and reaction products are analyzed by the spectrograph.

Fig. 3.3 schematically illustrates the details of our experimental setup, from the target chamber to the focal plane. The tracking detectors, S803 and S804, were located 30.3 cm apart, with S804 just 8.32 cm in front of the target. This allowed, on an event-by-event basis, determination of the incident beam position and trajectory at the target location. After interacting with the target, the particles were collected and analyzed by the spectrograph's quadrupoles and dipoles, then brought to a focus at the first focal plane detector, S801. The focal plane detectors are separated by 1.073 m, providing a measurement of both angle and position to

47
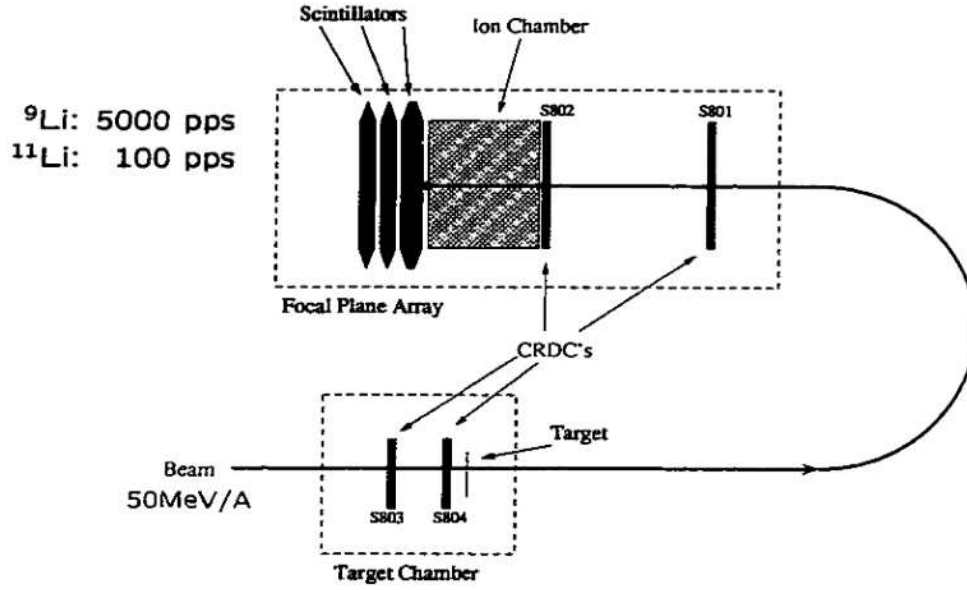
Figure 3.3. Schematic of the target chamber and focal plane detector setup, with beam intensities shown

high accuracy. Immediately following S802 is a gas-filled ion chamber. The back window of the ion chamber is formed by the first of three plastic scintillators, E1, which also served as the event trigger.

3.4 Detector details

Before discussing the detector system in detail, it is necessary to spend some time discussing notation conventions. In the practice of beam transport, a particle is represented in a multi-dimensional coordinate system with at least five important variables:

$$Z = (x, a, y, b, \delta). \tag{3.3}$$

In traditional notation, x and y are the positions relative to the central axis with respective momentum components p_x and p_y. The central momentum, p_0, is given by $p_0 = \sqrt{p_x^2 + p_y^2 + p_z^2}$. The planar angles between the particle trajectory and

48

the beam axis are denoted by $a = p_x/p_0$ and $b = p_y/p_0$. Often in older literature (a, b) is represented as (θ, ϕ), but that notation can be confusing when discussing scattering angles as well. The energy deviation from the central beam is denoted by $\delta = (E - E_0)/E_0$. Other elements such as mass and charge may also be included in Z; for this experiment only the canonical five parameters of Eq. (3.3) were used.

Traditional beam transport elements bend in the horizontal (x) direction. Since the S800 Spectrograph dipoles bend vertically due to spatial restrictions, two possibilities for notation arise: either place momentum along y—contrary to years of practice—or make x vertical and y horizontal. The latter has been adopted as the S800 convention. To maintain a right-handed coordinate system with $+z$ in the beam direction, $+y$ is chosen to be beam-right and $+x$ to be "up" at the target location. Maintaining consistency through the spectrograph requires that $+x$ remain to the inner radius, becoming "down" in the focal plane. If there is a drawback to this notation, it is the placement of $+x$ to a dipole inner radius. This causes a negative correlation between x and δ, whereas typical beam optics notation would have a positive correlation. This, however, is a minor detail that is easily accounted for in beam optic codes.

3.4.1 CRDC detectors

The CRDC detectors [40] are position-sensitive drift chambers yielding information in both x and y directions. Fig. 3.4 provides a rough schematic of these detectors. Drift chambers measure position in one direction by the drift time. As the beam particles pass through the detector, they ionize the gas. The free electrons then migrate towards the positive voltage on the anode wire. Although the actual drift velocity (and hence drift time) depends on the gas pressure and type as well as the anode voltage, typical velocities are a few cm/μs. With sub-microsecond timing

49

CRDC DETECTORS

Size: 60cm X 30cm (Focal Plane)
20cm X 10cm (Target Chamber)

Pads: 0.10in
#: 224 (Focal Plane)
32 (Target Chamber)

Gas (Pressure): 80%CF; 20% Isobutane
140 Torr (Focal Plane)
12 Torr (Tgt Chamber)

Frisch Grid

Anode Wire

Pads
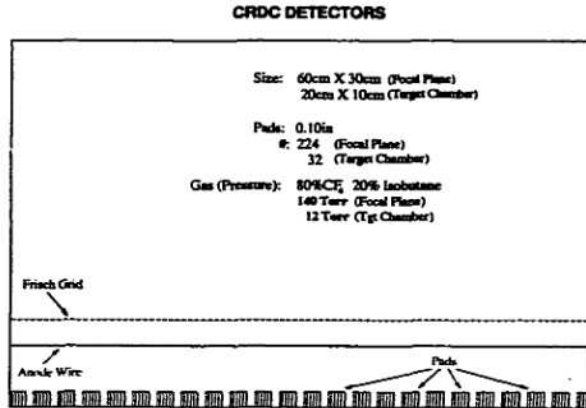
Figure 3.4. Schematic diagram of a Cathode Readout Drift Chamber

one can achieve position resolutions at the mm level or below. When the wire is hit a signal is generated and the time recorded. The time difference between this signal and the E1 (§3.4.3) signal is proportional to the distance from the wire at which the beam particle passed through.

The other position comes from the cathode pads that line one edge of the detector, just below the anode wire. The amount of charge collected on each pad is proportional to its proximity to the ionizing particle passing through the detector. For each event, the charge distribution along the pads is approximately gaussian. Using a fast least-squares minimization routine [41] to find the centroid of this distribution, we can determine the location of the ionizing particle to within 0.1 pad. Given that each pad is physically $0.1''$ wide, this results in a net resolution of $0.254 \, mm$. A sample charge distribution and fit are illustrated in Fig. 3.5. The detectors were oriented such that the pads were along the horizontal (transverse, y) direction in the scattering chamber and along the vertical (dispersive, x) direction in the focal plane. The advantages of such an orientation will be discussed in the context of analysis (chapter 5).

50
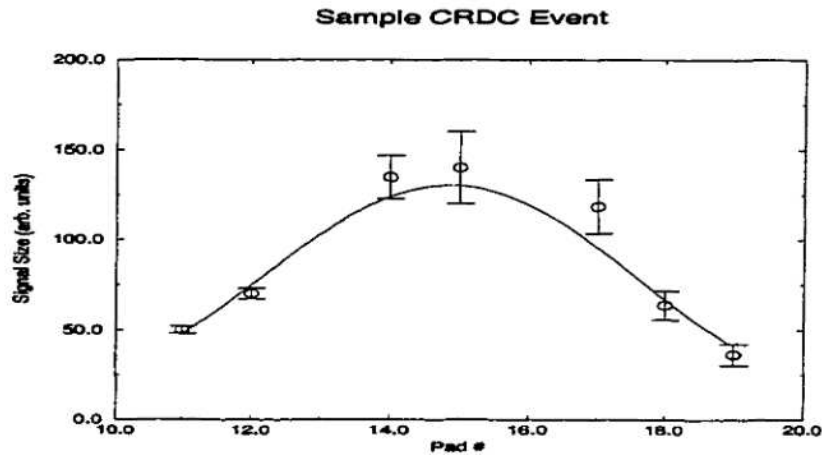
Figure 3.5. Sample charge distribution and gaussian fit of a single CRDC event from one of the target-chamber detectors.

3.4.2 Ion Chamber

In the focal plane, following the second CRDC detector, is an ion chamber which functions as a gas-filled ΔE detector. It is segmented by sixteen anode wires placed at one-inch intervals through the length of the chamber. Summing the sixteen signals allows for more complete and accurate charge collection than a single anode could provide for a volume of this size. This signal can be used in conjunction with the E1 stopping scintillator for particle identification via the ΔE-E technique. For this experiment, however, due to the high purity of our beams, this information was unnecessary and thus unused.

3.4.3 Plastic scintillators
3.4.3.1 In the spectrograph

The end of the S800 focal plane has three plastic scintillators, each with a photo-multiplier tube (PMT) at either end. This allows division of the light signal that can provide rudimentary position information by comparing the signal from the top PMT to that of the bottom PMT. The first scintillator, E1, forms the back

51

window of the ion chamber. The other two scintillators are flush to the one immediately preceding. For highly-penetrating particles, these can be used as yet another ΔE-E detector. Our heavy Li ions actually stopped in E1 rendering the last two scintillators unnecessary.

The E1 scintillator serves a second crucial purpose in any S800 experiment. It is the master event gate. If a particle has the right momentum to pass through the spectrograph and make it to the back of the focal plane, it is deemed a good event; the rest of the detectors are processed and recorded contingent on a valid signal from E1. By virtue of being the master trigger, E1 also serves as a start for all of the TAC and TDC clocks used.

3.4.3.2 In the beam line

In the A1200 beam line is a thin scintillator, appropriately dubbed the "beam line timer", or BLT. This detector was approximately 56 meters upstream from the target position. When the beam passes through it, the BLT provides a fast timing pulse without noticeably upsetting the beam energy or flight path. Using a delayed BLT signal as a "stop" in conjunction with the "start" from E1 provides time of flight (TOF) information for performing momentum calculations.

3.5 Proposed analysis technique

3.5.1 The advantage of dispersion matching

For a magnetic field of fixed strength, Eq. (3.1) characterizes the arc path as $\rho = \mathbf{p}/qB$. Obviously the more energetic particles will travel toward the outer edge of the dipoles. A perfectly mono-energetic primary beam can be difficult to obtain; the case is even worse for exotic secondary beams that are produced via fragmentation reactions since the reaction kinematics cause a large energy spread in the resultant products. One can improve matters by using slits and velocity

52
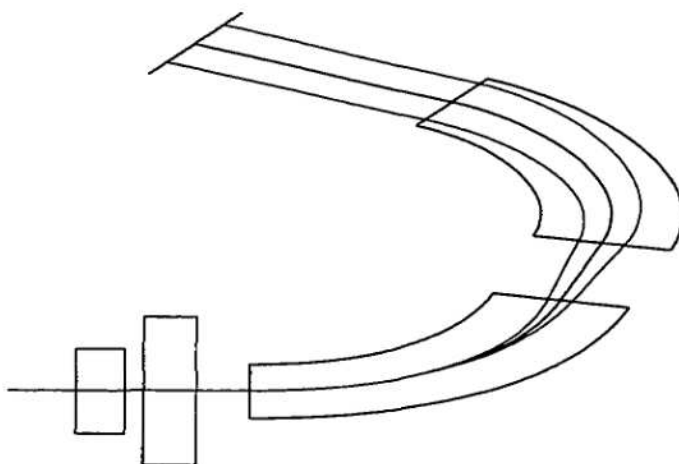
Figure 3.6. Effect of beam momentum spread on final spectrograph imaging. Particles differing only in energy are smeared out in the focal plane. Though not easy to see from the picture, an angular spread also develops.

filters, but this only further reduces the already limited intensity of radioactive nuclear beams. What is the real effect of this energy spread? Fig. 3.6 illustrates what happens to a normally focused beam with a $\pm 1\%$ energy spread as it goes through the S800 Spectrograph system. The final image is smeared out in the x direction and has developed an angular spread as well. With the possibility of a reaction at the target location that can transfer momentum and/or scatter the particle, the problem is how to use the final image to decipher whether the different focal properties are due to beam intrinsics or reaction mechanisms? Dispersion matching [42] is an elegant method of canceling out the beam intrinsics. By transporting the beam achromatically, we can obtain a dispersive focus that has energy (momentum) correlated with both incident position and angle such that the final focus is a single point, as shown in Fig. 3.7. This allows the decoupling of reaction effects from beam intrinsics. This technique of matching momentum

53
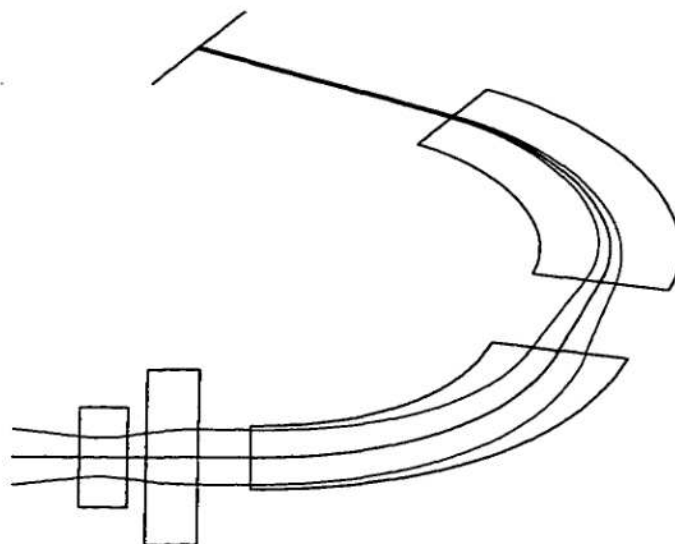
Figure 3.7. Effect of proper dispersion matching. The beam momentum is corre-
lated to incident position and angle in order to improve spectrograph imaging and
resolution.

to position and angle is also referred to in the literature as the energy loss mode.

The simplest and most immediate consequence of proper dispersion matching is
excellent energy resolution for resolving inelastic processes in the reaction. Elasti-
cally scattered particles will arrive at the same point in the focal plane regardless
of whether the true incident energy was $E_0 + \Delta E$ or $E_0 - \Delta E$. The final width will
only be due to the incoherent beam spot size and aberrations in the imaging system.
Similarly, inelastic processes remove a fixed amount of energy (i.e. corresponding to
the energy level of an excited state) and will form discrete lines in the focal plane,
separate from the elastic line, with widths independent of the beam energy profile.
The disadvantage to using the dispersion-matching technique is the demand placed
on target design—especially for radioactive beams. The A1200 mass fragment sep-
arator has a momentum dispersion of $10\,\mathrm{cm}/\%$. Radioactive beams produced via
fragmentation inherently have large energy spreads. To accept as much beam as

54

possible, the A1200's exit slits can be set as wide as 1.0% in momentum. Thus, to accomodate the full range of the beam spot, the target must be 10 cm tall, leading to potential uniformity problems.

3.5.2 Ray reconstruction

Although a single detector in the focal plane provides information about the momentum, using a second detector to make angle measurements in the focal plane provides the opportunity for full ray-reconstruction through the device. This allows the determination of scattering angle at the target, which can yield clues as to the structure and nature of the interaction. In order to do the full ray reconstruction accurately, detailed knowledge of the magnetic fields—especially the fringe fields—of the optic elements is necessary. Using the particle-optics code COSY [43] to calculate the mapping of trajectories through the S800, we should be able to deduce the angle at which the ion leaves the target from the focal plane information. Comparing to the incident angle as measured by the tracking detectors, we can find the scattering angle and construct an angular distribution.

3.5.3 Modeling

Finally, to understand the shapes of the angular distributions obtained from our measurements, it will be necessary to model the S800 Spectrograph and the detector efficiencies to determine an appropriate solid angle and acceptance. For this, a detailed Monte Carlo code was implemented. This will be discussed in detail in Chapter 6.

3.6 Summary

We produced secondary ^{9}Li and ^{11}Li beams from a primary ^{18}O$^{(6+)}$ beam, using the A1200 fragment separator in its high-acceptance mode. The beam was trans-

55

ported in the so-called energy loss, or dispersion matched mode in order to improve the spectrograph resolution. Use of tracking detectors in the target chamber allowed us to improve the angular resolution by knowing the incident profile on an event-by-event basis. Monte Carlo techniques were necessary for modeling the response function of the experimental apparatus.

56

CHAPTER 4

Calibration methods

Since the ΔE-E information from the ion chamber and E1 scintillator was not used in the analysis, in-depth calibration of those signals was not performed and will not be discussed. The critical information for doing ray-reconstruction and scattering-angle analysis comes from the four Cathode Readout Drift Chamber (CRDC) detectors [40]. To check momentum calculations, time-of-flight (TOF) information was measured using both the RF of the K1200 cyclotron and a thin plastic scintillator in the beam line called the beam-line-timer, or BLT.

4.1 CRDC detectors

Fig. 4.1 schematically illustrates the beam's path through the detector system. The CRDC detectors provide information in two planes. To obtain a spatial calibration, a mask with an unambiguous image pattern was placed in front of the detectors and a defocussed beam sent through the spectrograph system, illuminating the mask. The actual masks and techniques used for the focal plane and target chamber differed from each other and will be discussed in detail separately. However, our discussion begins with the elements common to the basic calibration technique.

4.1.1 CRDC basics

As mentioned in §3.4.1, the CRDC detectors use charge-sensitive pads in one plane and drift time in the other plane to provide spatial information. The sig-

57
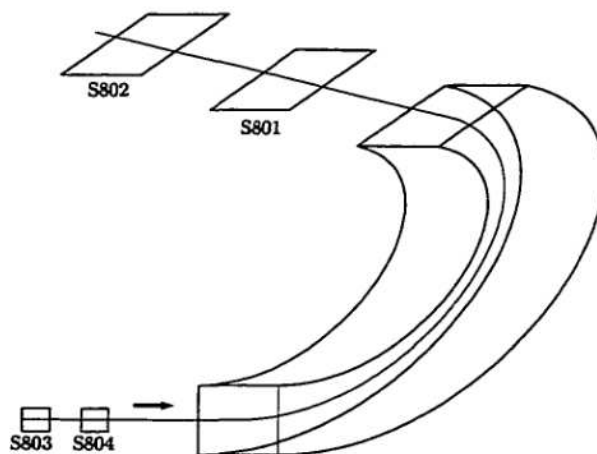
Figure 4.1. A schematic view of the central beam path through the S800 detector system

nal on a pad is proportional to its proximity to the position of the ionizing event. Any given event will cause a signal in several pads as seen in Fig. 3.5. However, the signal is also affected by the physical properties of the pad. Even though they are designed to a rather tight tolerance, there are variations in each individual pad response. The capacitance of each pad is dependent upon its size, and thus the amount of induced charge can vary. Each pad also has its own pre-amp and electronics which could lead to discrepancies in measured signal size. To ensure that the gaussian fits to these charge distributions are reliable, care must be taken to have the pads properly gain-matched. For this, a tail-pulser is connected to the anode wire and a pulse of fixed height is sent down the wire. Since the wire is equidistant from every pad, and we are using a fixed pulse, each pad should register the same signal. Repeating this procedure with the pulse height set at 0.6 and 0.3 times the original height yields a three-point calibration curve. A least-squares fit is then performed to obtain the gain and offset of each pad. Then every gain is normalized to that of the first pad and the offsets are adjusted accordingly. Using this normalized

58

calibration ensures that every pulse of a given height will register equally in each pad.

4.1.2 Focal plane CRDCs (S801 and S802)

The two CRDC detectors in the focal plane were filled with 140 Torr of a mixture of 80% CF_4 and 20% isobutane. The mask used for each of the detectors is illustrated in Fig. 4.4. The physical holes in the mask are 1/16″ in diameter. Due to the detector resolution and the range of angles that the particles may have, the effective hole size becomes approximately 3.5 mm, which is the size of the holes in the figure. The ideal method of doing these calibrations is to set the $B\rho$ of the S800 to bring the direct beam to the focal plane and then sweep the beam through the focal plane by varying the field of the spectrograph, illuminating as many holes and slits as possible. Fig. 4.5 illustrates a typical image for S801 under these circumstances. Unfortunately, that image is not from this data set. It was generously donated by Peter Santi for illustrative purposes [44]. One of the pitfalls of being the first to do an experiment is that "little" details and problems are sometimes overlooked or unforeseen. The calibration images for S801 and S802 from this experiment are shown in Fig. 4.6. It must be stressed that the data points in the calibration images are *not* averages of collections of events. There is exactly a one-to-one correspondence between events in the data stream and the plotted points. Note that rather than the few hundred events *per hole* seen in the ideal case, these data show less than fifty events *total*! In fact, no single hole has more than one event present. These data immediately call to mind two questions: "Why are there so few counts?" and "What assurance is there that these events are not background?".

The answer to the first is simple. For the ideal spectrum illustrated by Fig. 4.5, the calibration data were taken early in the experiment with the S800 at 0° relative

59

60

Individual Pad Response

Constant Pulser

Pad Number

Normalized Gains and Offsets fo

Pad Number
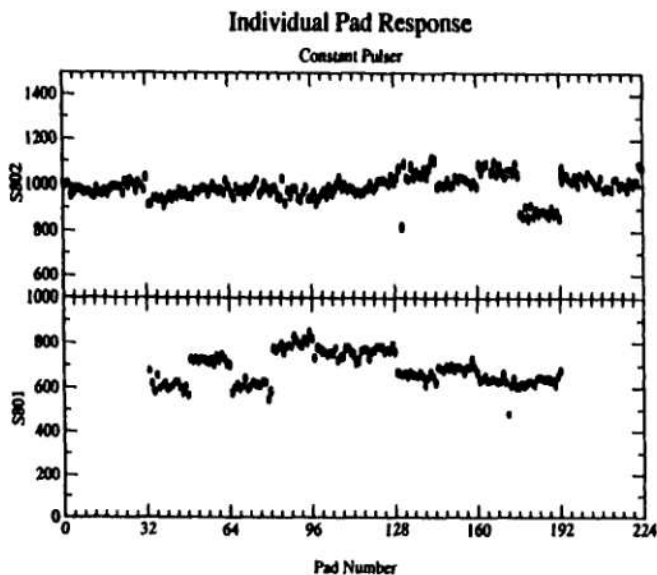
Figure 4.2. Pad response for a constant pulser. (Detector S801 was missing the 32 outermost pads on each end for this experiment.) This illustrates the need for pad normalization.
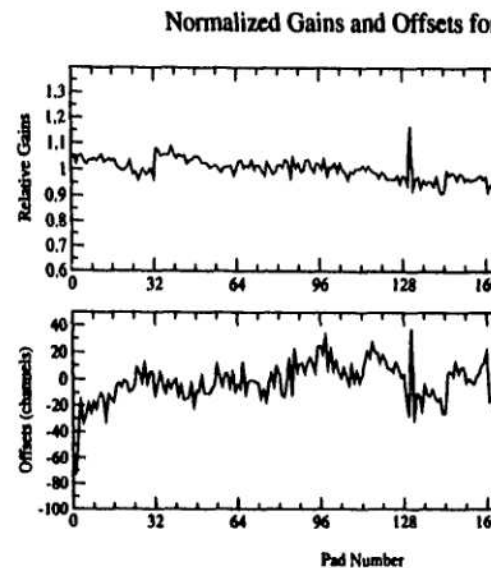
Figure 4.3. Sample normalization of pa
sure that no pad is given unfair weig
squares fit due to an enhanced or defi
gain of each pad is normalized to th
Then the offsets are adjusted accordin
of specific size will have the same calib
pad.

61
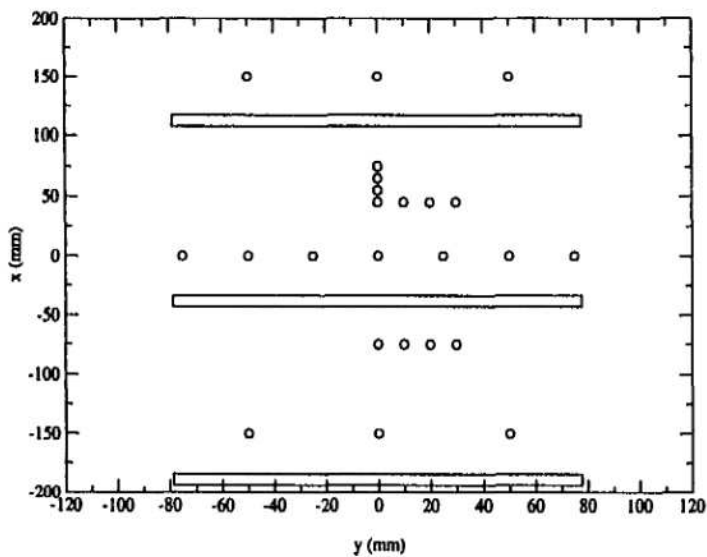
Figure 4.4. The standard mask used for calibrating the
focal plane detectors
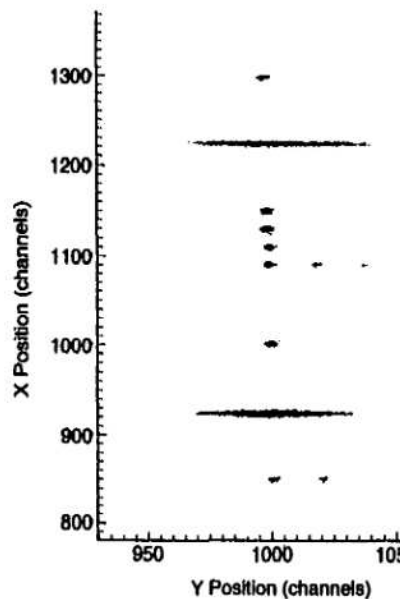
Figure 4.5. A typical S801 calibratio

62
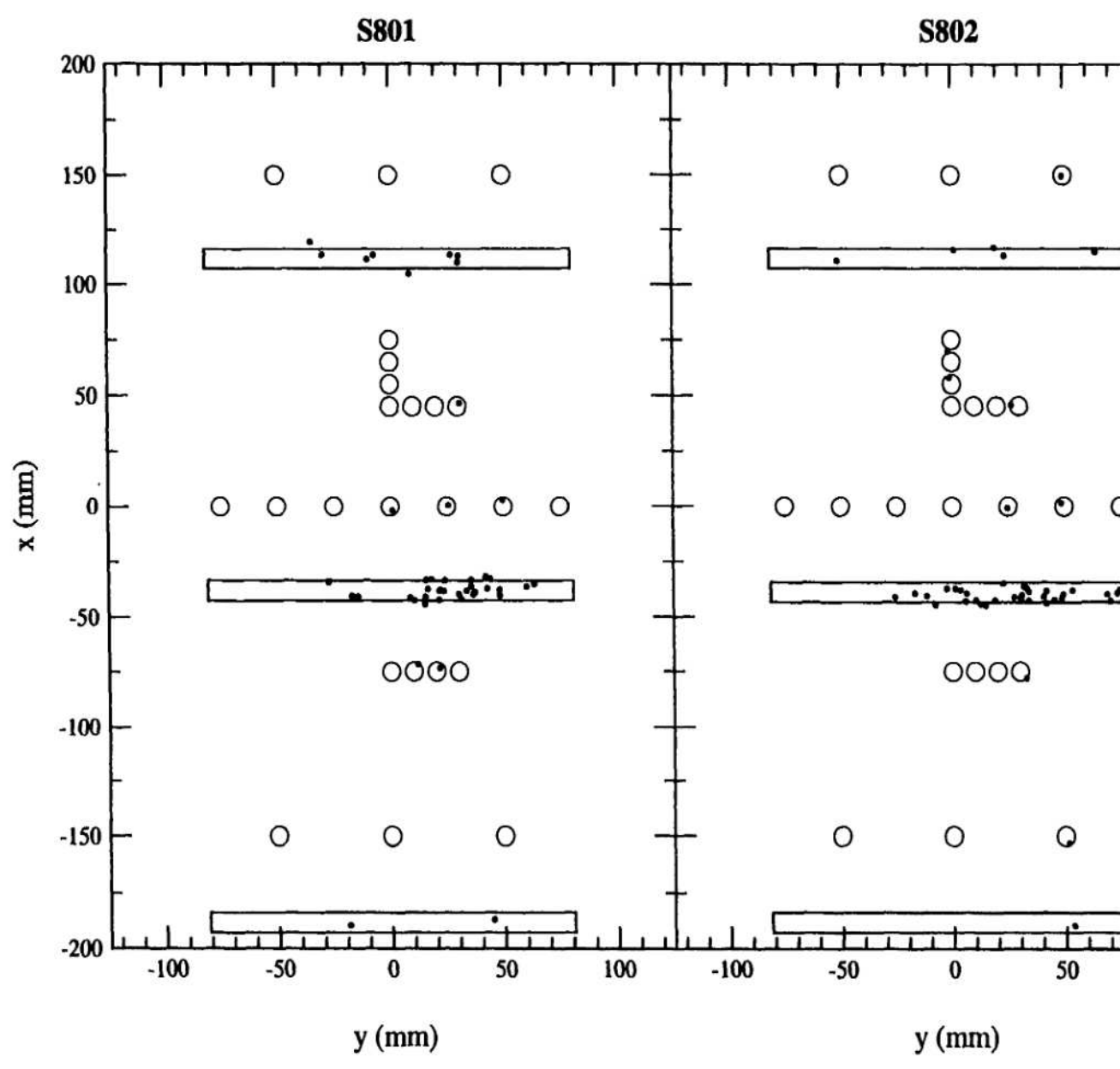
Figure 4.6. The calibration data for S801 and S802 from this experiment. Since there are so few counts, been superimposed to aid in visualizing the mask pattern.

to the beam line. This allows for ample statistics to be accumulated in a short amount of time. For the present experiment, the focal plane calibration was slated for the end of the run rather than the beginning. That meant that the spectrograph was at an angle of 5° to the beam line when the data were taken. It was assumed that since the S800 subtends ±5°, the focal plane would still see the direct beam that was coming in at 0°. Unfortunately, this assumption was drastically wrong and no direct beam made it to the focal plane. Left to the mercy of the scattered event rate, our ability to collect significant statistics was limited considerably. Monte Carlo simulations (chapter 6) using our fields show that the effective aperture for the S800 during these runs did not extend further forward than 2.8°. This will be discussed in more detail in §6.6 beginning on page 140.

As for the second question regarding the data's validity, it is impossible to say with 100% certainty that the image is void of spurious events. Several things, however, point to these events being real. First, these data have a coincidence gate between all four CRDC detectors as well as the E1 scintillator. It is very hard to imagine a spurious event, such as a cosmic ray, that has a non-noise signal in four detectors separated by several meters. Cross talk does not seem to be a reasonable explanation as the electronics for the focal plane and those of the target chamber were housed in separate CAMAC crates on separate floors of the target room. That points strongly to these being real signals. Also, as seen in Fig. 4.6 there are no events that do not correspond to a physical hole in a mask. The probability for spurious events to appear exactly at a mask hole when there is so much available area in the detector is very small. Another argument for the validity of the data is from the calibration coefficients themselves. The x(long) direction is governed by CRDC pads and thus fixed at a gain of 0.254 mm/fitted pad. The only free parameter is the zero point, which should appear near the physical center of the detector—pad 112. In the y

63

Table 4.1. Focal plane CRDC calibrations from several S800 experiments. All values obtained through private communication with the individual experimenters.

Experimenter	Y S801		Y S802	
	gain (mm/ch)	offset (ch #)	gain (mm/ch)	offset (ch #)
Caggiano	-0.09301	1595.0	0.09827	1766.0
Davids	-0.10922	1559.2	0.09456	1851.7
Guimarães	-0.10460	1429.6	0.09259	1730.4
Komives(1)[a]	-0.08797	1619.1	0.09347	1736.4
Komives(2)	-0.07285	1888.5	0.07908	1968.8
Santi	-0.07977	1586.2	0.09241	1718.2
This Work	-0.10330	1390.0	0.10538	1596.0

[a]Due to changing gas conditions, the drift time varied greatly over the course of the experiment. The values listed for the Komives data are nominal ranges of the calibration.

direction the main hope is to identify the center line or other key aspects of the mask.

In checking the y calibration, comparisons with calibrations obtained from other experiments can provide assurance that our gains are reasonable. Noting that the focal plane CRDCs have always been used with the same gas composition and pressure and assuming that their performance is reasonably constant over time, those other calibrations should help in understanding the uncertainty of the current calibrations. Table 4.1 reveals that the y-gains should be around 0.09–0.10 mm/ch and the two detectors within 5–10% of each other. Finally, we can check that the data using these calibrations is consistent with dependencies predicted from transfer maps. This last statement, of course, relies upon the calibrations of the tracking detectors in the target chamber, which now gain our attention.

4.1.3 Target chamber CRDCs (S803 and S804)

The target chamber CRDCs were calibrated at the very beginning of the experiment using the primary beam ($^{18}O^{6+}$) in a defocussed state along with an imaging mask. The defocusing was performed by reducing the field in the last element of the

64

final beam line triplet to one-half of its nominal value. The imaging mask used for the target chamber calibrations is illustrated in Fig. 4.7. These tracking detectors used the same CF_4-isobutane mix as the focal plane CRDCs, but ran at a lower pressure of 8 Torr.[1]

In the focal plane there was a separate mask for each of the CRDCs so that each detector could be imaged individually. This was not the case for the target chamber. Again, being one of the first experiments to use the S800 Spectrograph caused some trouble. At that time there was no ladder mechanism in place for moving masks in and out of place. Inserting or removing a mask required venting and opening the target chamber—a four hour cycle at best. Time constraints of allotted running time effectively restricted the number of chamber openings possible. A single mask, illustrated in Fig. 4.7, was bolted onto the face of S803. It was anticipated that the mask would create a nicely-collimated and well-defined beam image and profile at S803 which would then propagate to S804 and through the system. Obviously this would yield an excellent calibration for S803. There appeared to be several methods that would allow this single mask placement to be sufficient in obtaining a good calibration of S804 as well.

The first idea was to use a collimator on the target ladder—a so-called "hole" target—in conjunction with the mask. It was hoped that we could use ray-triangulation from the known hole location and S803 mask pattern to determine the calibration of S804.

A second method was to raise and lower the target ladder, imaging the hole target at several different heights with the secondary ^{9}Li beam. Again it was hoped that ray-triangulation from the "known" hole height and S803 data could allow us to deduce the location at S804.

---

[1] The pressure was eventually raised to 12 Torr (see §4.1.4.2) but the calibrations were performed at 8 Torr.
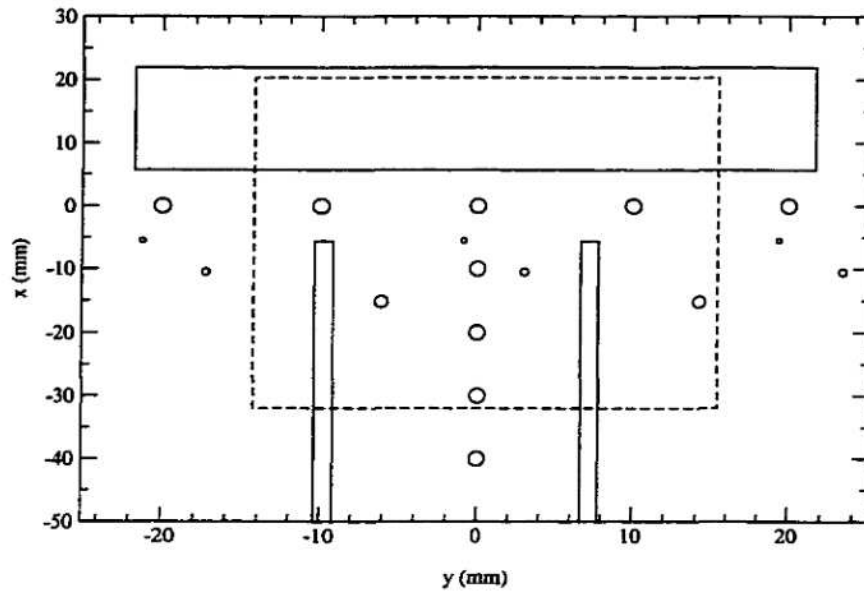
Figure 4.7. The calibration mask for the target chamber detectors. The dashed line shows the approximate area illuminated by the defocussed ^{18}O beam.

A final idea was thought to be the most robust, although it was also the most complex. It required two assumptions: good focal plane calibrations and transfer maps that would accurately describe the imaging properties of the S800. The basic notion was that from measurements of the beam profile at the focal plane, one could, through use of an inverse map, calculate the profile at the target location. Using calibrated S803 information, it would be a simple exercise to deduce the pattern at 804 to yield the appropriate target profile predicted by the inverse map.

The failings of each of these ideas will now be discussed, beginning with the first. Unfortunately when the target chamber was opened up to remove the S803 mask, it was discovered that even though the remote readout of the target ladder height indicated the hole target to be centered, it was in reality about 2 cm low. This meant that the hole target did not line up with any mask holes and no particles actually passed through both. The only events obtained are those that actually went *around* the entire target ladder and still made it into the S800's acceptance. Thus these

66

data were unusable.

There were several problems with the last idea of using map information:

- As seen in section 4.1.2, our focal plane calibration is far from robust.

- We have been unable to produce transfer maps that reproduce the optical properties of the data to a high degree of accuracy and/or reliability .

- The data show very odd tracking behavior, such as $(a|a) = 0$ which to first-order implies a non-invertible matrix.

- The defocussed nature of the beam in these runs leads to large entering angles and this possibly limits the accuracy of our maps since the fringe fields are now more important.

- All of these problems mean that our maps miss the measured b_{foc} and a_{foc} by at least 10 mr.

This left the hole-target imaging technique as the only reliable method of obtaining the calibration of S804.

4.1.4 Hole target imaging
4.1.4.1 Pad (y) calibration

The center hole of the S803 mask and the target ladder were sighted and aligned together. Using this information in conjunction with a fixed pad size of 2.54 mm and our ability to determine the event centroid to 0.1 pad allows the y_{804} calibration to be obtained with great certainty. Since both tracking detectors had 32 pads and were approximately centered on the beam line, $y = 0$ should occur around the 16th pad. This provides one more consistency check for this plane.

67
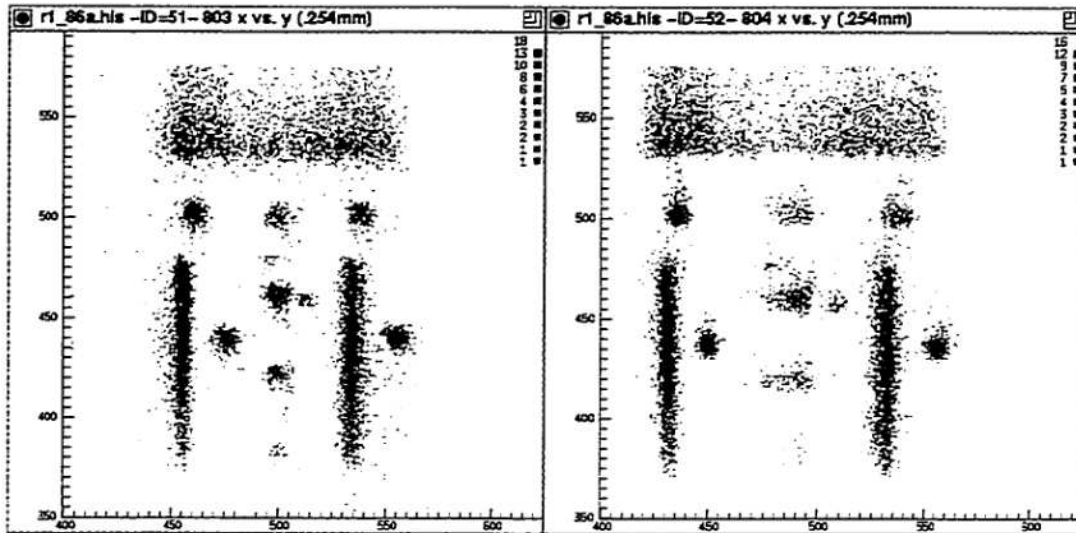
Figure 4.8. Images from the tracking detectors S803 and S804 with the calibration mask bolted to S803. Note the divergence of the beam.

4.1.4.2 Drift (x) calibration

Inspection of Fig. 4.8 illustrates a subtle problem that is obvious in hindsight, but was not fully appreciated during the run. Notice that the separation between adjacent mask holes is not the same in S804 as it is in S803. Since the pads are a fixed physical size, we are prevented from adjusting the gain. The difference in spacing *must* be due to the divergent nature of the defocussed beam.

Given the divergent nature of the beam and the spread in the hole positions seen in the pad direction, it is imperative to understand the implications for the drift direction. The first step was to make sure that the values used for each detector were essentially the same. Since the two detectors were connected to the gas-handling system in series, they must have contained the same gas at the same pressure, meaning that the drift velocity should be the same in each detector. For the best consistency it was decided to do the target chamber drift calibrations in terms of nanoseconds, rather than raw TDC channels as was done with the focal plane.

68

Eq. (4.1) shows the TDC calibrations obtained using a pulser.

$$t_{803} = -57.28 + 1.27355 \text{ ns/channel}$$

$$t_{804} = -53.46 + 1.27549 \text{ ns/channel}$$

(4.1)

Before continuing, a short detour is necessary to explain the purpose of cali-
brating the mask pattern when supposedly one can use ray-triangulation with the
hole target at different heights to obtain the drift calibration. The reasoning is
as follows. The mask data were obtained with the ^{18}O primary beam as noted
above. However, upon switching to the secondary ^{9}Li beam, the signal-to-noise
ratio became very small and the efficiency of these detectors decreased greatly. It
was surmised that this was due to the smaller ionizing ability of a beam with half
the Z and M. To counter this, the gas pressure was increased 50% from 8 Torr to
12 Torr while keeping the drift voltage constant. This did increase the efficiency of
the tracking detectors; however it also meant that the drift velocities, and hence the
x calibrations, would be different. Again, time constraints prevented repeating the
mask runs at this new pressure. It was under these new conditions that the hole
target runs were performed. Thus we have an absolute calibration of S803 at 8 Torr
and the potential of a derived calibration of S804 at 12 Torr, and these need to be
reconciled. Fortunately, the $\mathcal{E}/p$ ratio was in the region where the drift velocity
curve is approximately linear with pressure. That allows us to compensate for the
difference in the calibrations from the ^{18}O and ^{9,11}Li beams by means of a simple
linear scale factor of the gain. To do this properly, a reasonable starting point for
the drift calibration of S804 in terms of the 8 Torr pressure is needed. It can then be
fine-tuned using the hole target tracking information under the 12 Torr conditions.

Back to the task at-hand of determining this reasonable starting point for the
drift calibration of S804, a TRANSPORT [45] calculation was performed for a typ-
ical beam envelope from the exit of the A1200 to the target location using the

69

Table 4.2. Summary of S804 Gains

Description	Gain(mm/ns)
S803 calibration	0.02571
a diverging	0.02992
a converging	0.02658
Final Result	0.02974

beam line settings of this experiment. **TRANSPORT** predicted a beam half-envelope of $(x, a, y, b) = (4.77, 2.24, 2.12, 9.91)$ in units of cm and mr. Propagating back from the target location to S803 and writing in terms of a full envelope, a spot size of $(x, y) = (9.36, 3.48)$cm is expected; a spot size of $(7.4, 3.38)$cm was actually observed. Given that the mask does not allow the full beam spot to be seen and keeping in mind that **TRANSPORT** is typically trusted to only a few percent for the NSCL beam lines [46], this appears consistent. Using the a as a divergence to calculate the vertical spacing between adjacent holes yields a gain 15% greater than the gain of S803. Taking a to be converging (**TRANSPORT** knows nothing about the convergence of the beam—only its envelope) rather than diverging yields a gain even closer to that of S803. The actual calibration should lie somewhere in this range, and indeed does. Table 4.2 lists the calibration of S803, these S804 bounds, and the final S804 calibration used. The final gains for S803 and S804 differ by about 15%. This may seem disconcerting given the arguments at the beginning of this section, but in fact this discrepancy is not inconsistent with the relative gains of the focal plane CRDCs which operate in a similar fashion.

With an initial solution in-hand, it remains to find the true gain. To do this we

70

assume calibrations of the form:

$$x_{803} = -57.99 + \alpha \cdot 0.02571\,t$$

$$x_{804} = 44.62 - \alpha \cdot 0.02974\,t$$

(4.2)

where α is the linear scale factor relating the drift velocities of the two different gas pressures. A note about the form of the above calibrations: in the focal plane, the drift calibration is written as

$$position = gain(ch - offset)$$

(4.3)

but for the tracking detectors it is written as

$$position = offset + gain \cdot t.$$

(4.4)

The first form is more concise and especially clear for determining what drift time actually yields a position at the center of the detector (defined as zero). However, the issue of changing gas pressures renders that form awkward since adding a scale factor to the gain in Eq. (4.3) would imply that particles passing through the optic center ($x = 0$) would always have the same drift time, regardless of the pressure. Viewed another way, $t = 0$ should correspond to an event essentially at the anode wire, which is fixed in space. The first form would have the anode wire's position change as a function of gas pressure whereas the latter form does not. Using the actual drift times from the various hole target runs, a least-squares minimization of how far the ray-tracing from S803 and S804 missed the hole position was performed by varying α from 0.50–2.00. This process was iterated over several values of the S804 gain in the range of 0.02571–0.03000 to find the best gain/scale factor combination. That is how the final result in Table 4.2 was obtained. The final value of α was determined to be 1.335, resulting in a calibrated drift velocity of about $4\,cm/\mu s$. Using the program **MAGBOLTZ** [47] to estimate the drift velocity for this gas mixture at our voltage and pressure, we obtain an expected drift of about $6\,cm/\mu s$, so our calibration result appears reasonable.

71

Table 4.3. Final calibration results in units of mm for all four CRDC detectors. t is the drift time in TDC channels for the focal plane detectors and ns for the target chamber detectors. n represents the fitted pad centroid. The scaling factor α is 1.00 for ^{18}O, and 1.31 for ^{9,11}Li.

Focal Plane	$y = b(t - a)$		$x = 2.54(n - c)$
	a	$b\,(\text{mm/ch})$	c
S801	1390.0	-0.10330	111.8
S802	1596.0	0.10538	111.7
Target Chamber	$x = a + \alpha \cdot b\,t$		$y = 2.54(n - c)$
	a	$b\,(\text{mm/ns})$	c
S803	-56.990	0.02571	14.7
S804	44.620	0.02974	15.3

4.2 Concluding remarks

Table 4.3 summarizes all of the calibrations used. In every detector, the pad calibration places the center at the expected location using a standard gain of 2.54 mm/pad, fitting the charge distributions of the cathode pads to the nearest 0.1 pad. Spacings in the mask patterns that fall exactly where they are expected are also produced with the standard pad gain.

For the drift direction, the focal plane gains are found to be within 2% of each other while the tracking detector gains only match to about 15%. The focal plane calibrations suffer from poor statistics—especially in y. However the mask pattern is reproduced and there is high confidence in the validity of the few events present. The drift gains are consistent with those obtained in other experiments under similar operating conditions. The tracking detector calibrations suffer from using two methods (mask data and hole-target tracking) at two different gas pressures. The derived gains, however, are consistent with predictions of ion-optic codes such as **TRANSPORT** and **COSY**. These dependency checks are strengthened by the fact that the drift plane in the target chamber corresponds to the pad direction in the

72

focal plane, and vice-versa. This means that, provided the ion-optic code is operating properly, its results can be used in conjunction with a pad measurement in the focal plane to predict the corresponding drift measurements in the target chamber.

73

CHAPTER 5

Data analysis

5.1 Data preprocessing

The raw data stream contains many parameters that are not of use in the final analysis and others that are in a highly compressed format. For example, the pads of the CRDC detectors [40] are read out with FERA [48] electronics in their zero-suppressed mode. Zero-suppressed mode is highly efficient because it does not use unnecessary space on the magnetic tape during data collection, but is inefficient for off-line analysis due to the large amount of logic processing required to unpack it. Furthermore, even though information from all the active pads of an event are necessary to determine the positional centroid of that event through a least-squares fit, the analysis requires only the fit result.

The second purpose of preprocessing the data stream is to add new, calculated, pseudo parameters to aid in the analysis. There are two types of pseudo parameters added to our data stream: those related to the centroid fit of the pad distributions, and those related to detector efficiency.

5.1.1 Fitting the pad charge distributions

As shown in Fig. 3.5 on page 51, each event leaves a gaussian-shaped charge distribution over the pads, to which a least-squares fit is performed to find the true location of the event. The least-squares routine is based on the Levenburg-Marquardt method as presented in Numerical Recipes [41], with modifications. The

74

basic method in [41] simply terminates if a solution does not exist or if a convergent fit cannot be found after a reasonable number of iterations. For analyzing event-mode data, this is unacceptable behavior. To avoid this, traps that detect singular matrices and return a status flag indicating the type of failure (or success) of the fit were added to the Numerical Recipes routines.

Another consideration for analyzing event-mode data was how to automate the fitting process to reliably provide fits for a variety of spectra. This was a particular problem for the tracking detectors as most of their events had long tails due to noise. Several events were examined by eye to determine a nominal threshold below which to omit data points from the fit. This eliminates noise and zero values due to malfunctioning or dead channels. The visual inspection also revealed that, regardless of the centroid position, the FWHM of the distributions were approximately constant, allowing a single initial guess for the FWHM to be used for every event. In order to determine an initial guess for the centroid, we simply chose the channel with the largest signal. Finally, one further item must be considered. Due to the noise and intrinsic behavior of the tracking CRDC detectors, we observed the occasional event with large signals above our chosen threshold near the edge of the detector even though the main peak of the distribution is in the middle. Those edge channels, if included in the fitting process, can seriously disrupt the accuracy of the fit. To reduce the effect of these outliers we use the initial guess of the centroid in conjunction with the knowledge that the FWHM is typically 2–4 pads to fit only data from signals within five pads of the central one.

For events that truly lie near the edge of the detector, we may not have a full peak shape to fit. There may also be events which, after applying the threshold condition, have fewer than the four points necessary to perform a three-parameter least-squares fit. To avoid needlessly throwing away data, we also calculate a center-of-gravity

75

(c.g.) for the charge distribution. In cases with enough information to perform the fit, the c.g. differs from the fitted centroid by typically less than 0.5 mm. Spectra created from the c.g. also typically have resolutions that are marginally worse than the spectra from the centroid fit. This is illustrated in Fig. 5.1.

5.2 Drift corrections

The tracking CRDC detectors had several performance problems throughout the experiment, the most striking of which were due to difficulties with the ionizing gas. There were repeated problems in maintaining a consistent flow rate, and hence purity, of the gas. The effect of this was to cause the gain in the drift direction to be time-dependent. The time it takes ions created by particles passing through a single spot in the detector to drift to the anode was different at the beginning of a run than at the end. This results not only in a gain shift, but may possibly shift the baseline as well. This change in drift times is illustrated in Fig. 5.2. Furthermore, this changing gain for each of the tracking detectors, as well as the fact that the two were oriented upside-down relative to each other, meant that the measured incident angle on target also varied greatly over the course of a run. This is shown in Fig. 5.3. These changing profiles were verified to be artifacts of poorly performing tracking detectors through examination of the focal plane profiles. If the beam profile measured by the tracking detectors was truly changing, these changes would manifest themselves at the exit of the spectrograph. Since the focal plane maintained a constant position and angle profile during the times that the measured incident profile varied, we can be certain that this is an artificial effect, and account for it in the analysis.

There exists an excellent self-correcting algorithm [49] for dealing with drifts associated with electronics. However, this algorithm is unsuitable for correcting the

76
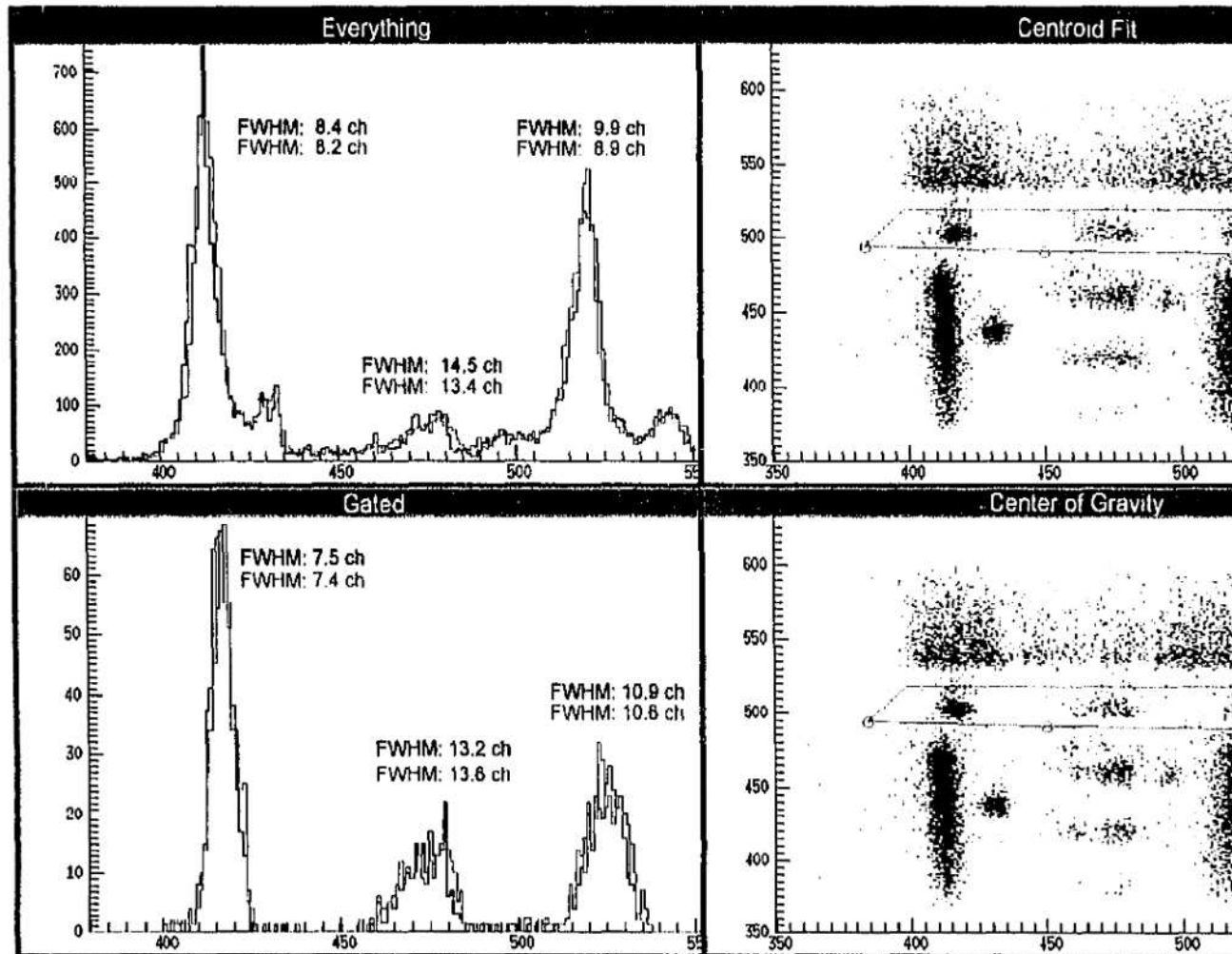
Figure 5.1. Comparison of center-of-gravity and least-squares methods for obtaining the centroid of projection spectra, the red lines describe the centroid fit while the black are for the center-of-grav
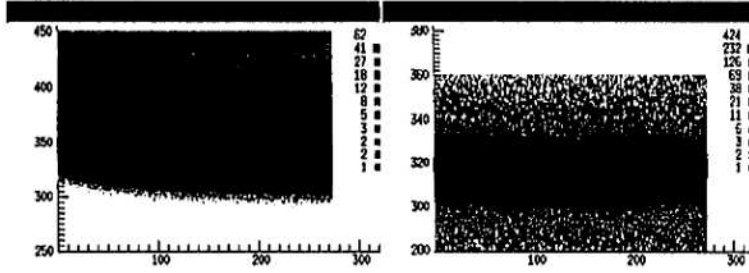
Figure 5.2. Position drifts of the tracking detectors. The left panel illustrates the target position as measured from the tracking detectors S803 and S804. The right panel shows the focal plane position measured by S801. Note that the apparent change in target position is not reflected in the final position indicating that this is only an illusory shift
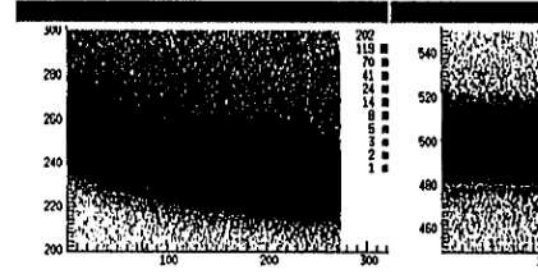
Figure 5.3. Angle drifts of the tracking c panel contains the profile measured fror tectors and the right is that of the foca As with the position, the measured chan; file is not reflected at the exit indicating rather than true beam dyna

78

drifts present in this data for two reasons. First, it requires a sharp "marker" to provide a reference or "goal" channel. This marker must be present for essentially every event. The data from the present experiment have no such feature. Second, the algorithm is much more robust when the time drifts and shifts occur over short time intervals. The fluctuations in this data have long time scales, sometimes on the order of hours, and are thus not suited for that algorithm.

The solution used in this analysis was a table look-up method. First, the data were processed while recording the full scale and baseline for each of the tracking detectors, S803 and S804, as a function of time in the manner discussed below. Then these data were reprocessed, with the gains adjusted according to the previously recorded values. This method then requires two parameters: a time scale and a method of determining the proper gains and full scales.

In establishing an appropriate time scale, we must find one that is both long enough to provide a smooth correction not overly influenced by sudden, erratic fluctuations, yet short enough to not miss any salient features of the gain shifts. Another consideration is to keep the size of the look-up table manageable. Several time scales were investigated, ranging from several events to several buffers. The final decision was to use 100 8kb buffers, which corresponds to roughly 3100 events. A typical section of runs that can be analyzed continuously consisted of 20,000–80,000 buffers.

Now we discuss the correction algorithm in detail. Over any given time interval, there are events with the full range of drift times (see Fig. 5.2). We take the baseline to be the average drift time of the N events with the shortest drift times. However, to avoid unfair weighting of the average by outliers, the M most extreme events are eliminated from the average. A similar method is used for finding the maximum drift time over the interval, with the difference becoming the recorded full scale.

79

Mathematically,

$$t_{\text{int}_{\min}} = \frac{1}{N} \sum_{i=M}^{N+M} t_{\min_i},$$

$$t_{\text{int}_{\max}} = \frac{1}{N} \sum_{i=M}^{N+M} t_{\max_i}, \tag{5.1}$$

$$t_{\text{int}_{fs}} = t_{\text{int}_{\max}} - t_{\text{int}_{\min}},$$

where

$$t_{\min_0} < t_{\min_1} < \cdots < t_{\min_{M+N}},$$

$$t_{\max_0} > t_{\max_1} > \cdots > t_{\max_{M+N}}. \tag{5.2}$$

The goal is to strike a balance between choosing N large enough to get a good average, especially in cases where there are more than M outliers, yet small enough to avoid including events in the bulk of the distribution. The values for N and M finally settled upon were 100 and 5, respectively. Over an interval with approximately 3100 events, this amounts to using roughly the top and bottom 3% of the data to find the time range. The results of applying these corrections are provided in Figs. 5.4 and 5.5.

5.3 Transfer map generation

In this section we will discuss the process involved in developing the transfer maps used in the analysis, from the measured field data to the final derivation using the ion transport code COSY.

5.3.1 Fitting the fringe fields

The first step in generating a transfer map through the S800 Spectrograph system is to approximate the actual field data with an analytical form. In principle, COSY can use actual measured field maps that consist of both the field strength and and its derivative at points along a mesh. However, due to the nature of the S800

80

81
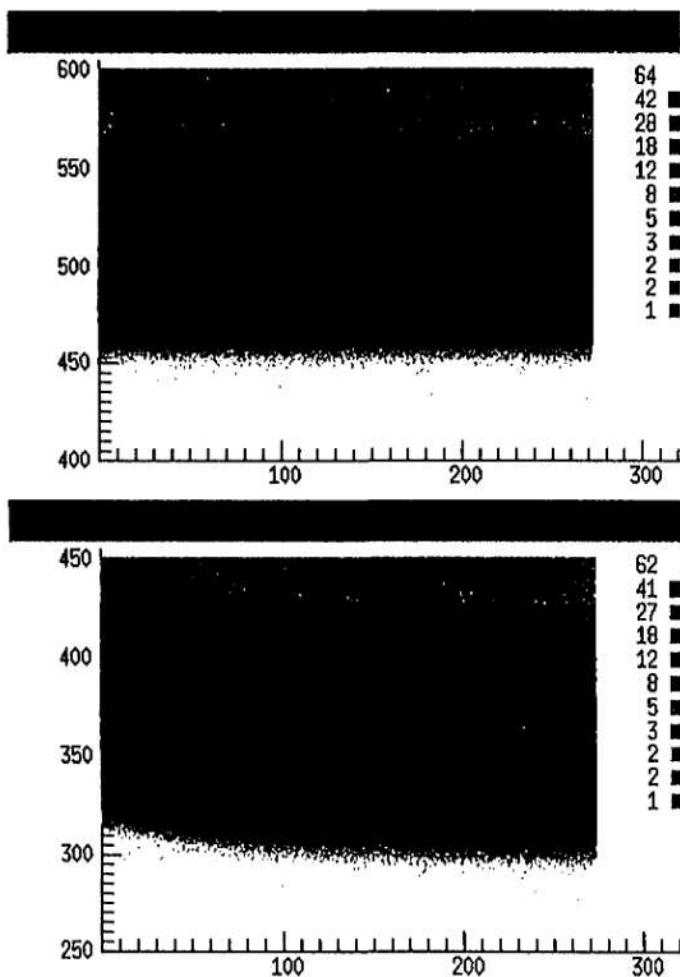
Figure 5.4. Corrected position drifts of the tracking detectors. The lower panel contains the raw data before the correction. The top panel shows the result of the correction.
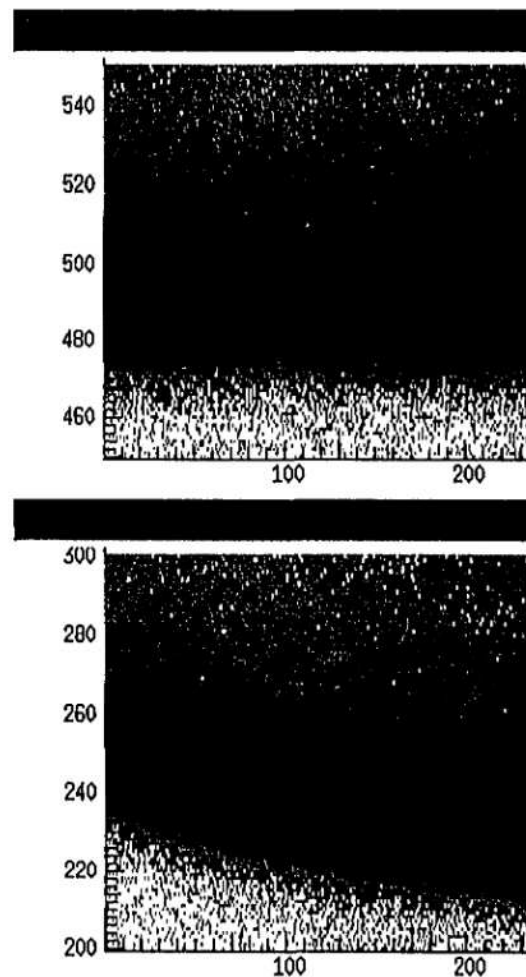
Figure 5.5. Corrected angle drifts of the
The lower panel contains the raw data
tion. The top panel shows the result

field data and its interaction with the COSY program, it was impossible to use such a method. There seem to be two possible explanations for this: either there is a problem with COSY's ability to use real field data, or there is a problem with the map measurements. Whatever the reason, the end result is that when attempting to calculate higher-order aberrations (which relate to higher-order derivatives of the field strength) the path integrals computed by the COSY code diverge radically and are unusable. This makes it necessary to use some approximations regarding the fields.

5.3.2 Modeling the fringe fields

The major assumption that was made regarding the fields of the S800's magnetic elements is that every magnet is a perfect magnet inside the region of the iron. That is, the fields are perfectly uniform and homogeneous inside the magnet. This leaves only the fringe fields as a source of variation and we modeled them as described below.

5.3.2.1 Interpolation of measurements

The S800 magnets have all been very carefully mapped throughout the entire path length at several current settings [50]. In particular, the exact field strength at seven different currents for the quadrupoles, and nine different currents for the dipoles was measured in 1.0 cm steps through each element. For each run of the experiment the current passing through each beam line element was recorded via BARNEY [51], the A1200/S800 beam line analysis/monitoring program. A new fringe field is constructed by interpolating the field at each point with a cubic spline function, using the values from the nearest current settings for which field data exist. This is done using the program IGOR [52].

82

5.3.2.2 Fitting the fields

This new interpolated field allows determination of (approximately) the value of the maximum magnetic field in each element. Once this new profile has been constructed, it must be fit with a smooth analytical function that can be used in a beam transport code such as COSY, MOTER, or TRANSPORT. The chosen functional form is that of Enge [53]:

$$B(z) = \frac{1}{1 + e^{p(z)}}, \tag{5.3}$$

where

$$p(z) = a_1 z + a_2 z^2 + a_3 z^3 + \cdots$$
$$z = x/D \tag{5.4}$$

with D the gap width of the particular element and x is the position along the beam line axis. An Enge function for one setting of an S800 dipole is illustrated in Fig. 5.6.

By definition, the zero of Eq. (5.3) is the location where the integral of the field under the entire function is equal to that of a field that drops sharply from full saturation to zero at the same location. This is equivalent to stating that the light and dark shaded regions in Fig. 5.6 have equal area. The difference between this zero and the physical edge of the magnetic element is called the "effective length", as noted in the figure. Typically the Enge function of Eq. (5.4) is terminated after five or six terms. One of the advantages to this functional form is that it has an infinite number of continuous derivatives, allowing numerical computation to arbitrary order. In order to use Eq. (5.3), which only ranges from zero to one, to fit the interpolated fringe field, we must scale the field by dividing it by B_{max}. Another consideration in fitting the interpolated field with an Enge function is to ensure that the resulting fit is smooth over the range used in ion transport codes—typically 3–5 gap-widths either side of zero. If care is not taken to fit the function over this

83
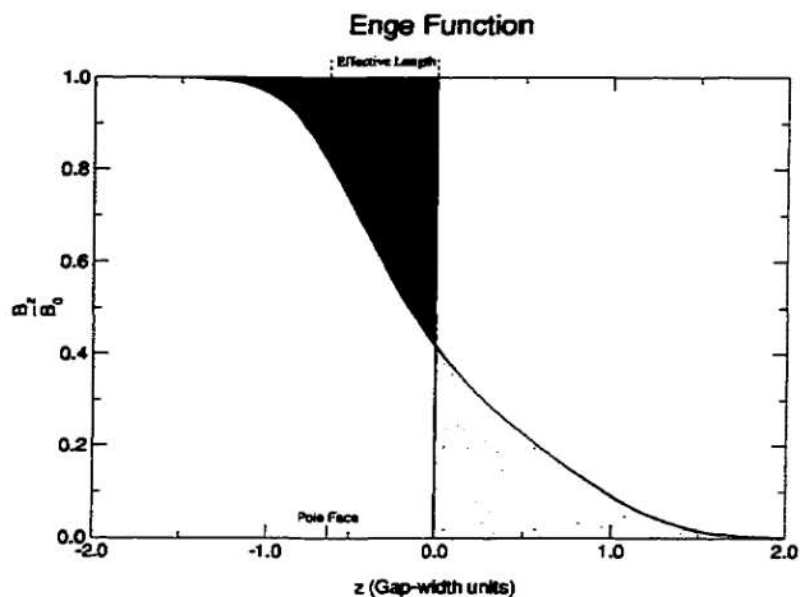
Enge Function

Figure 5.6. Sample Enge function for an S800 dipole with pole face and the effective length indicated

extended range, but simply fit to a shorter range, extremely divergent results can be obtained. Figure 5.7 illustrates just such a case. For a range of $\pm$ 2 gap-widths, this particular Enge function appears fine. However, just beyond that range to the outside of the magnet, the divergent nature appears. This particular function would lead to unreal transfer maps due to problems integrating the field in those regions.

5.3.3 Producing transfer maps

Once the fringe fields have been modeled and fit, we can use them in our ray tracing code, COSY, to determine a transfer map.

5.3.3.1 Computing the map

In conjunction with Daniel Bazin of Michigan State University (MSU), a special COSY routine for developing S800 transfer maps was developed. The essence of the routine is schematically outlined in Fig. 5.8. The parameters particular to each

84
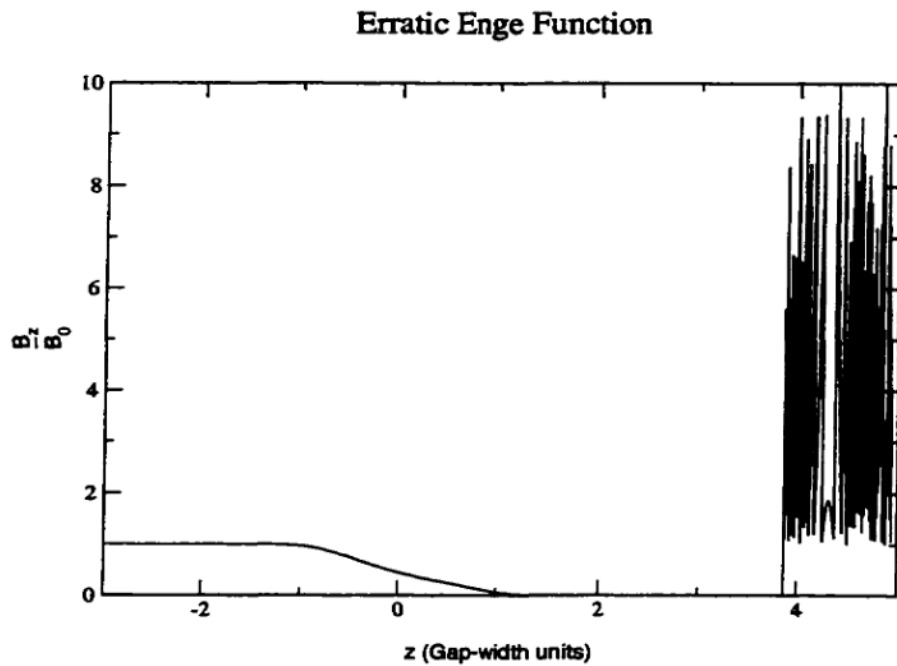
Figure 5.7. Poorly behaved Enge function. Only constraining the fit to two gap-widths either side of the effective boundary does not guarantee a smooth function over the entire range used in ion transport codes such as COSY.

85

element such as fringe field strength and shape, effective length, and aperture are determined from the characteristics determined in the IGOR interpolation of §5.3.2.1. The beam parameters are determined from the BARNEY records. In addition to the S800 elements themselves, a bit of spectrograph physics is added to the calculation. The S800 Spectrograph is designed to be an imaging system in the dispersive plane. That is, the final position should have no dependence on the initial angle—analogous to the human eye viewing distant objects. In transfer map terminology, this implies that $(x|a) = 0$. Ensuring this imaging condition provides an ideal case for the fitting capabilities of COSY.

The first method of fitting the map involved adjusting the drift length along the beam line axis from the exit of the second dipole to the first focal plane detector. The motivation for this was that, even though the spectrograph was designed to within certain tolerances, it is conceivable that when the detectors were mounted they may not have been placed at the precise location indicated by the Computer Aided Design (CAD) drafts. Furthermore, as the field in the dipoles changes, the focal length of the S800 is also slightly modified. In many cases, the fit from COSY moved the focal plane by 2–3 cm. Given that the idealized drift distance is 2.7 m, this is a small yet non-negligible effect of less than 1.0%.

However, not every case resulted in such a small change. In fact, with the BARNEY parameters obtained from the ^{18}O runs imaging the tracking detector calibration mask (§4.1.3), as well as the early ^{9}Li data, COSY predicted that the focal plane was moved 60 cm downstream to produce an imaging system. This is clearly impossible and unphysical. Further exploration revealed that the numbers recorded by BARNEY were not always accurate. In fact, it appears that the central database that BARNEY uses to collect its beam line settings was defunct for a good portion of the experiment. This is evidenced by the fact that there is absolutely no fluctuation

86

Set fringe field shapes

Set lengths and apertures

Set beam parameters

Generate map through the dipoles and save it

Set calculation to first order

Find map through quadrupoles

Apply Q-pole and Dipole maps

Check imaging condition

NO   YES

Adjust quadrupole strengths   Set final calculation order

Compute full transfer map
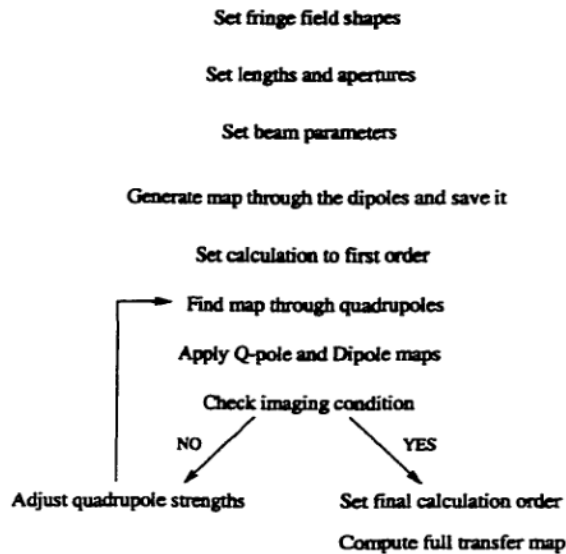
Figure 5.8. Schematic flowchart of transfer map generation

at all to five significant digits in the elements recorded over the first few days of the experiment. One would expect that, even if the field was stable, there would be at least some variation in the least-significant digits of the monitoring read-outs over time. Indeed, comparing the actual measured dependencies of the data between the early settings and the later settings shows very similar behavior and focusing of the beam—indicating that the fields remained relatively constant through the course of the experiment even though the field *measurements* as reported by BARNEY differed by as much as a factor of two and had the wrong ratios for the quadrupole fields. Table 5.1 lists the currents as read out by BARNEY for these two scenarios.

Thus, to obtain an imaging system, we used COSY to fit the field strength of the initial two quadrupoles rather than fitting the focal length. This second method of optimizing the transfer map to the real optics has several advantages, both aesthetic and physical, over the first method of fitting the focal drift. First, we know that the field strengths and fringe fields are approximate, so we should not readily expect a

87

Table 5.1. Example of inconsistent BARNEY readouts. The early runs contained 85% of the ^{9}Li data. Even though the quadrupole fields reported by BARNEY are very different, the measured beam behavior was very similar between the two data sets. This led to difficulties in determining accurate ^{9}Li transfer maps.

	Q1(A)	Q2(A)	D1(A)	D2(A)
Early Runs	35.465	27.679	209.061	211.505
Late Runs	37.903	42.370	209.967	212.851

"perfect" match between the the real field and our model-determined field. Second, since we are using modeled fringe fields, it makes sense to scale their strength by an amount necessary for the transfer map to image in the same manner as the real spectrograph system does. This provides better consistency to the interpolated method, since some imperfections in the interpolation are now accounted for with appropriate scaling. Thirdly, since the physical position and size of every other element of the S800 system is taken to be precisely the value used in the CAD design, it is consistent to hold this particular drift length fixed as well. Keeping this drift length constant regardless of the dipole and quadrupole field settings more closely matches reality as the first focal plane detector, S801, was never moved during the course of this experiment.

To compare this new method with the first, we can look at the changes effected by each. When analyzing the runs that previously moved the focal plane by 2 cm out of the 2.7 m drift, we now find that an imaging condition is met by changing the field in Q_x by less than 1.0%. For cases where the focal plane position "moved" by over half a meter, the field in the x quadrupole needs to change by nearly a factor of two, becoming approximately equal to that of the runs where the BARNEY readout was apparently closer to reality. When such a drastic change from the originally predicted field was found, the current corresponding to this new field was determined and the interpolation method of §5.3.2.1 repeated since the fringe field shape will not

88

necessarily scale linearly with strength. This new set of Enge coefficients was then used to produce a new transfer map. This second calculation then produced a further small adjustment of the fields of around 2.0%—consistent with the "good" results.

5.3.3.2 Verifying and tuning the maps

As discussed above, we are not only approximating the fringe fields with a smooth Enge function rather than using the actual field shapes, but the field to which we perform the Enge fit is an interpolated field, rather than a measured field. We also know that the BARNEY read-outs were faulty for at least part of the experiment. Even when BARNEY was correct, there still exists the uncertainty inherent in a fitting procedure. The stability of these approximations must be verified.

This can actually be done to a relatively high degree of certainty because of the nature of our experimental setup. By having tracking detectors at the entrance of the spectrograph (S803 and S804—see §3.3) as well as the exit, we can explicitly and directly measure each of the dependencies through the S800 Spectrograph system to the precision of the detectors. This is perfect for runs with no target in place. However, due to energy-loss through the target, the runs with real scattering data have different field settings, and hence different computed transfer maps from the no-target runs. The dependencies will also be smeared or fuzzed out due to statistical effects in the target such as multiple scattering. However, these will be small on average. Furthermore, by definition, when real scattering occurs the trajectory exiting the target (and entering the spectrograph) is not necessarily related to the incident tracked trajectory. However, for the data taken at zero degrees, the event stream is dominated by direct beam rather than scattered beam and these relationships will hold. For the 5° data, we must rely on what we learn from the 0° studies to guide us, with further adjustments being made clear through the Monte Carlo

89

techniques discussed in the next chapter.

What we are ultimately interested in for the analysis is a robust inverse map that can provide a means for us to determine the angles and energies entering the spectrograph based on the measurements at the exit. Now, since by definition

$$M_{\text{inv}} \cdot M_{\text{for}} = 1, \tag{5.5}$$

verifying the accuracy of the inverse map is equivalent to verifying the accuracy of the forward map. The forward map translates the initial parameters $(x, a, y, b)_i$ to the final parameters $(x, a, y, b)_f$. All of these are directly measured in our experiment. The inverse map uses the final parameters $(x, a, y, b)_f$ to calculate the incident parameters, $(a, y, b, \delta)_i$. We do not measure δ in this experiment. Therefore, we can more completely validate our transfer maps by using the forward map technique since we can directly measure all of the involved quantities. Thus we use the incident tracking measurements and propagate them through the forward map to the focal plane. These propagated values are then compared to the actual focal plane measurements. Of course, once the forward maps have been verified, the inverse maps are checked to ensure consistency. For this exploration, a random sampling of 40,000 events from each of the various run configurations was used.

As shown in Fig. 5.9, the biggest trouble comes in predicting the focal plane y and b dependencies on the incident angle b. COSY routinely produces dependencies that are too strong. The data shown are from a ^{9}Li run with no target in place. Furthermore, it is important that all aspects of phase space—including those in the focal plane—are accurately reproduced. Upon examining the focal plane correlations (Fig. 5.10) from the original COSY map, it is immediately apparent that the y-b focal plane relation is incorrect as well. Before continuing, a comment regarding the dependency mappings must be made. At first glance of Fig. 5.9, it is tempting to believe the $(x|x)$ mapping to be faulty, but it is the slope of this plot that must be

90

inspected, not the width. Our incident measurements consist solely of (x, a, y, b), not δ. However, the focal plane x position depends strongly on the initial energy:

$$x_f = -1.01\, x_i - 48.86\, \delta \tag{5.6}$$

For tracking particles forward through the S800 properly, we calculate the energy from the known dispersion relation of $103\,(\mathrm{mm}/\%\delta_\mathrm{p})$ and the conversion relation $\delta_E = (1 + 1/\gamma)\delta_p$. Since this does not account for the irreducible beam spot size, it yields the perfect correlation seen in the figures. Assuming an irreducible incident beam spot of roughly $2\,\mathrm{mm}$ FWHM and $|(x|x)| \approx 1$, one obtains the spread noticed in the focal plane.

In order to maintain consistency in the analysis, whatever adjustments are found necessary for the no-target data will be applied to the maps created for the target runs. Now we discuss at some length the necessarily iterative process used in determining the appropriate adjustments to the COSY-generated transfer maps. First, both the $(y|b)$ and $(b|b)$ terms were scaled by 0.416 and 0.632 respectively. This produced good agreement in the incident phase space as illustrated by Fig. 5.11. However, if we look at the focal plane phase space using this adjusted map we find (see Fig. 5.12) that even though it correctly predicts the y-b correlation, the above modification greatly reduces the b dynamic range. In light of this, it was decided to not scale the $(b|b)$ term at all, but maintain the same ratio of $(y|b)/(b|b)$ as in the first try. This results in a factor of 0.6586 for the $(y|b)$ term, which provides acceptable focal plane to target dependencies as well as more correct focal plane correlations. The agreement with the data is illustrated in Figs. 5.13 and 5.14. Once harmony in the forward map is achieved, we can invert it to see what happens. Again, agreement is very good. This 34% adjustment to the $(y|b)$ forward map term affects both the $(b|b)$ and $(b|y)$ terms in the inverse map by slightly less than 30%. The $^{11}\mathrm{Li}$ beams were of higher magnetic rigidity and required stronger fields to fo-

91

anl_r39orig_S801_2.dat
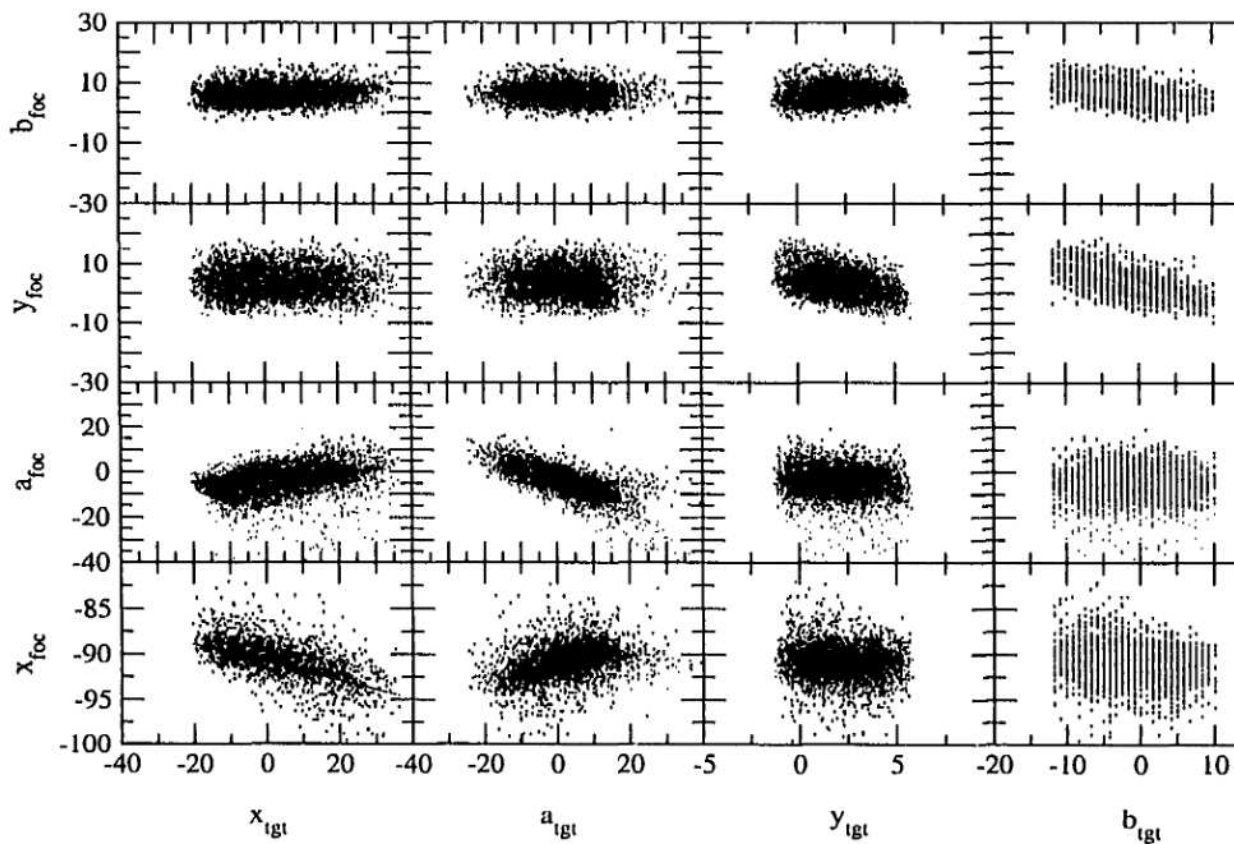
Figure 5.9. Focal plane dependencies on target parameters. The black points are actual data, the red p
target values as the black, but are then propagated through the transfer map to obtain a predicted focal
parameters with the largest mismatch in slope are in the transverse plane.

anl_r39orig_S801_2.dat

measured   mapped

93
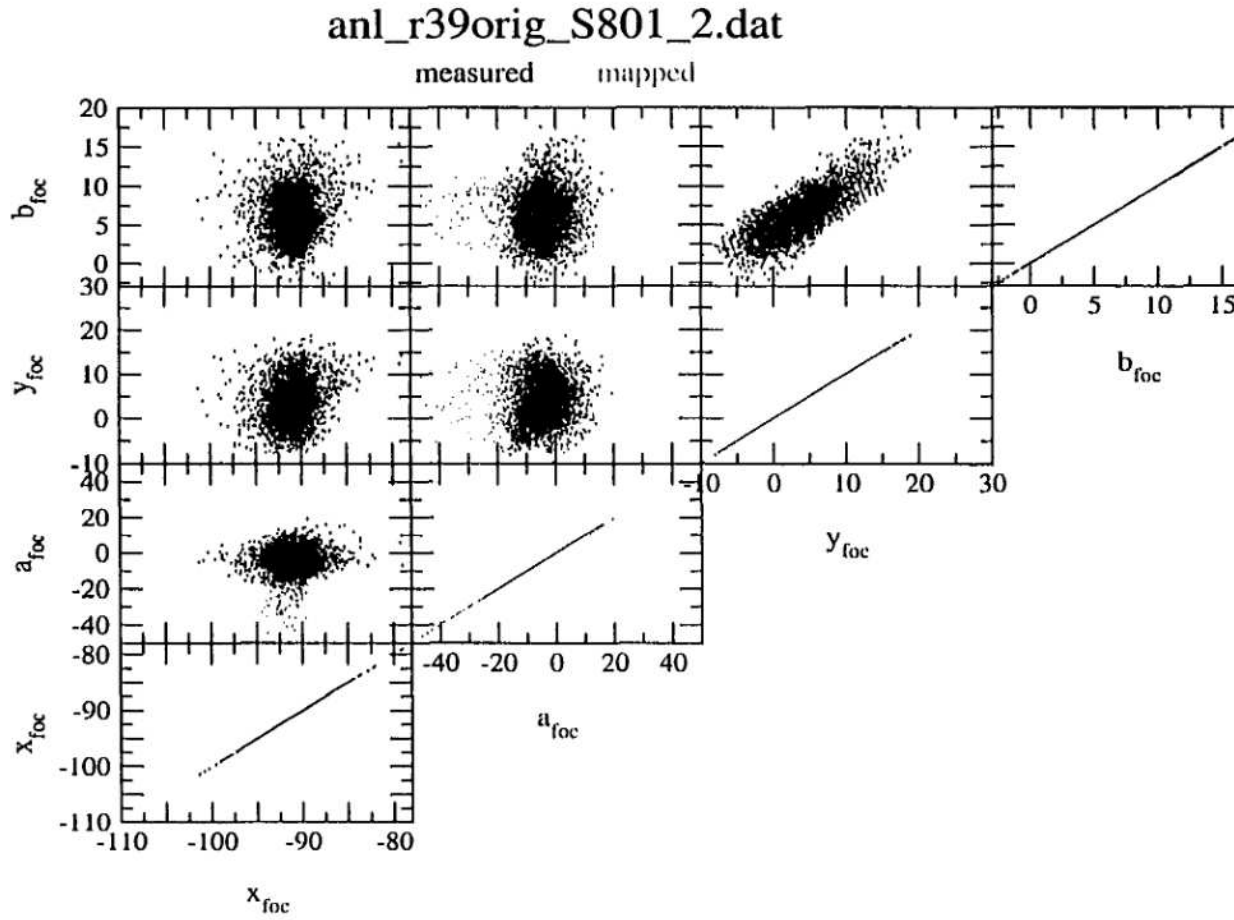
Figure 5.10. Focal plane phase space. The black points are actual data, the red points use the same t[
black, but are then propagated through the transfer map to obtain a predicted focal plane profile. Not[
relation predicted by the map.

anl_r39tweak1_S801_2.dat
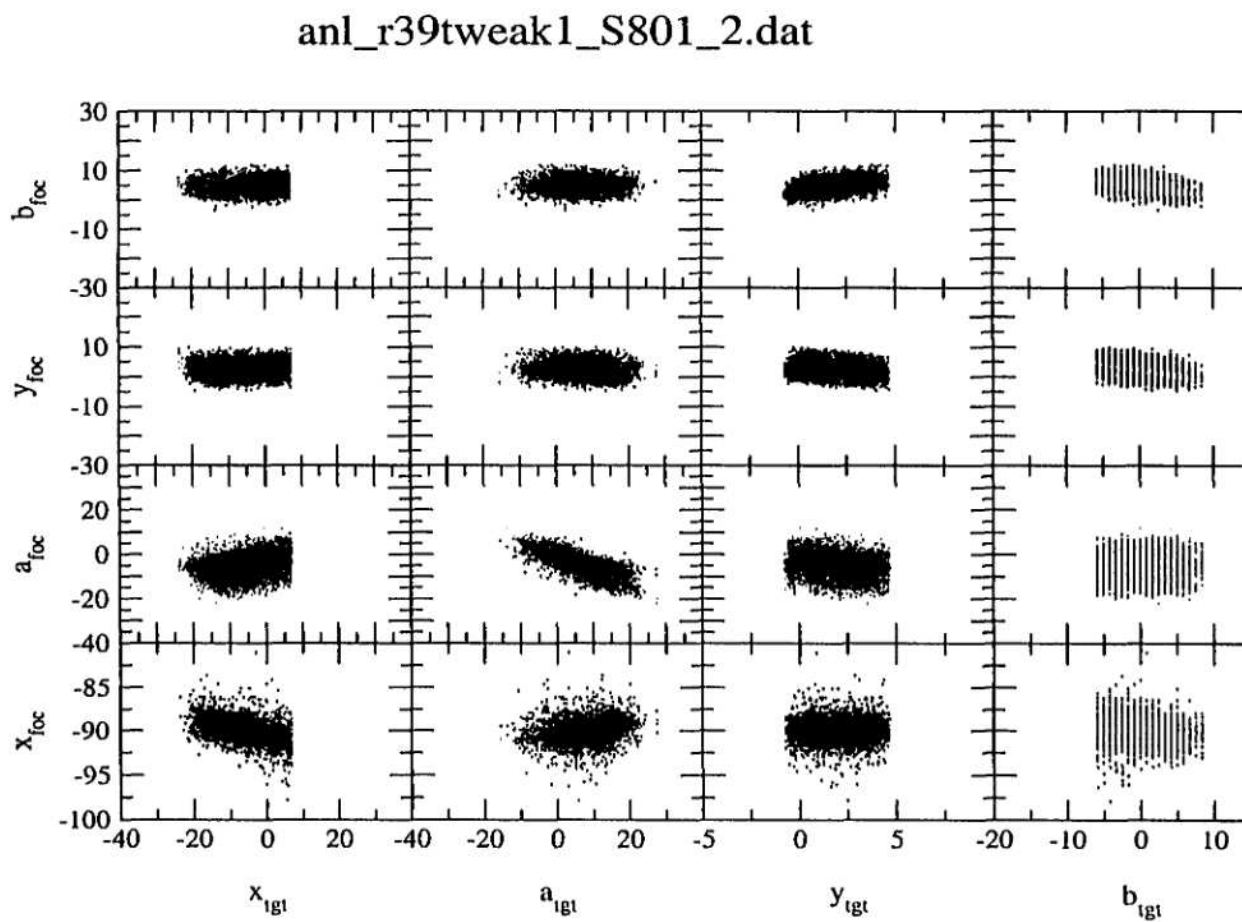
Figure 5.11. Adjusted focal plane dependencies on target parameters. Black points are data, red points
the target to obtain a predicted focal plane profile. The y and b dependencies are much improved over t

94

anl_r39tweak1_S801_2.dat

measured mapped
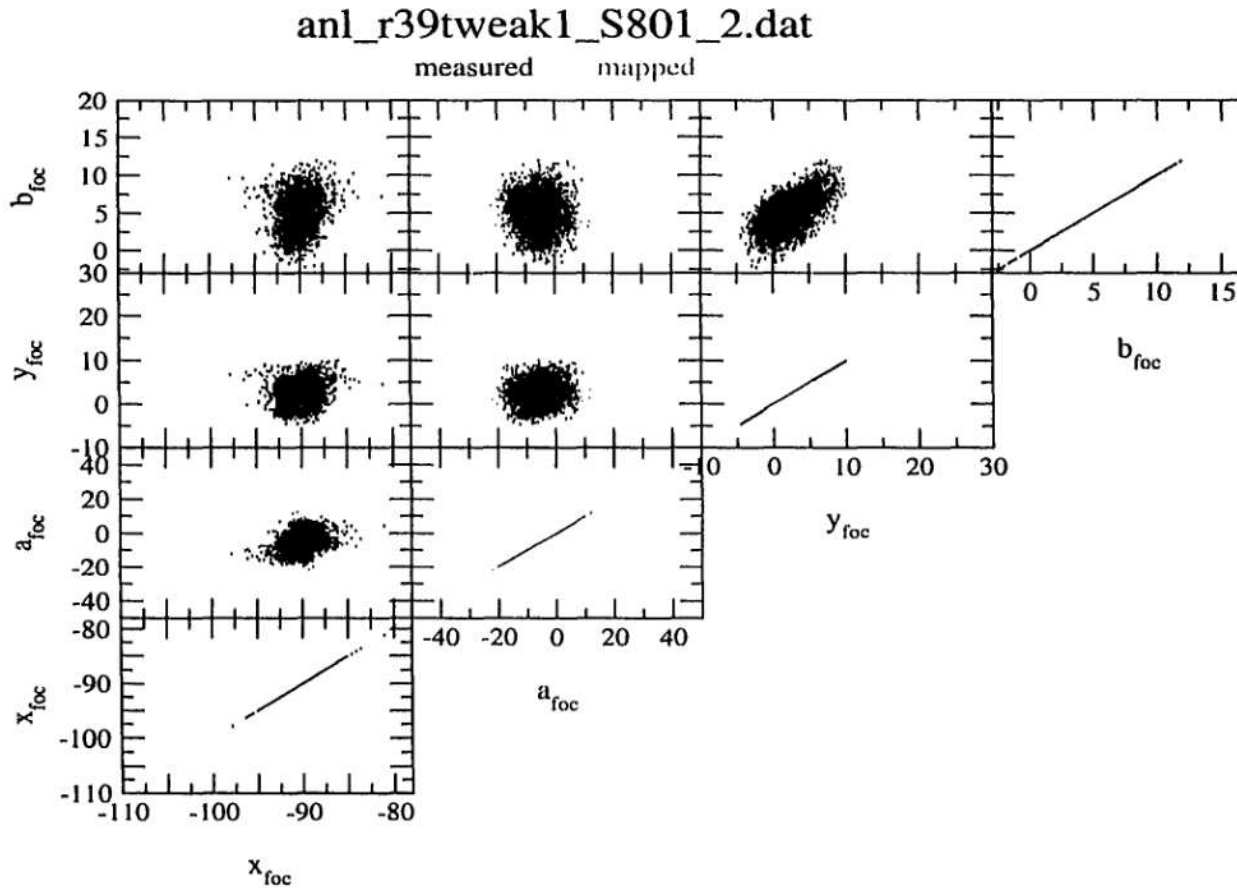
Figure 5.12. Focal plane phase space from the adjusted map. Black points are data, red points are mapp[ed] to obtain a predicted focal plane profile. Even though the correlations appear to have the proper values, the mapped y and b ranges are significantly reduced from the data indicating an imperfect adj[...]

anl_r39final_S801_2.dat
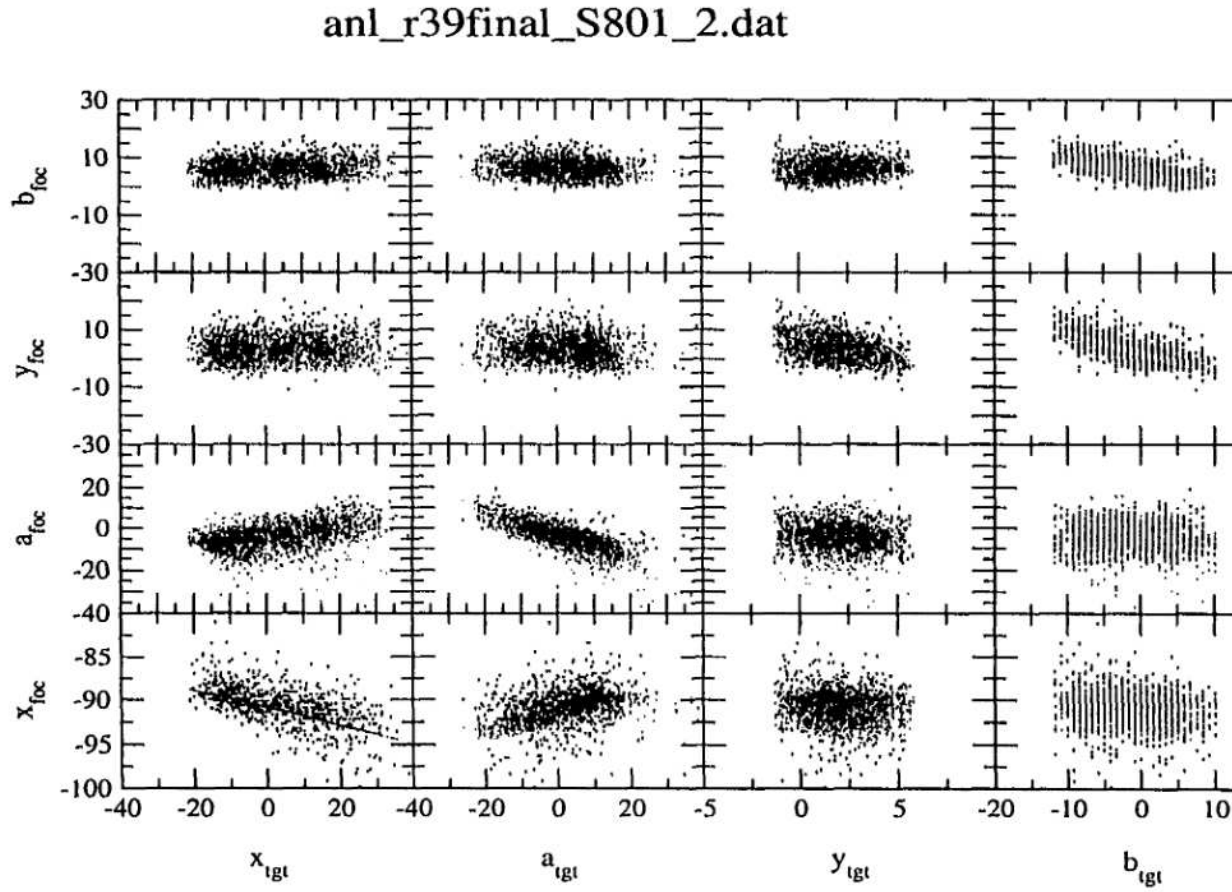
Figure 5.13. Final adjusted focal plane dependencies on target parameters. Black points are data, red
from the target to obtain a predicted focal plane profile. The y and b dependencies are consistent with t

96

anl_r39final_S801_2.dat
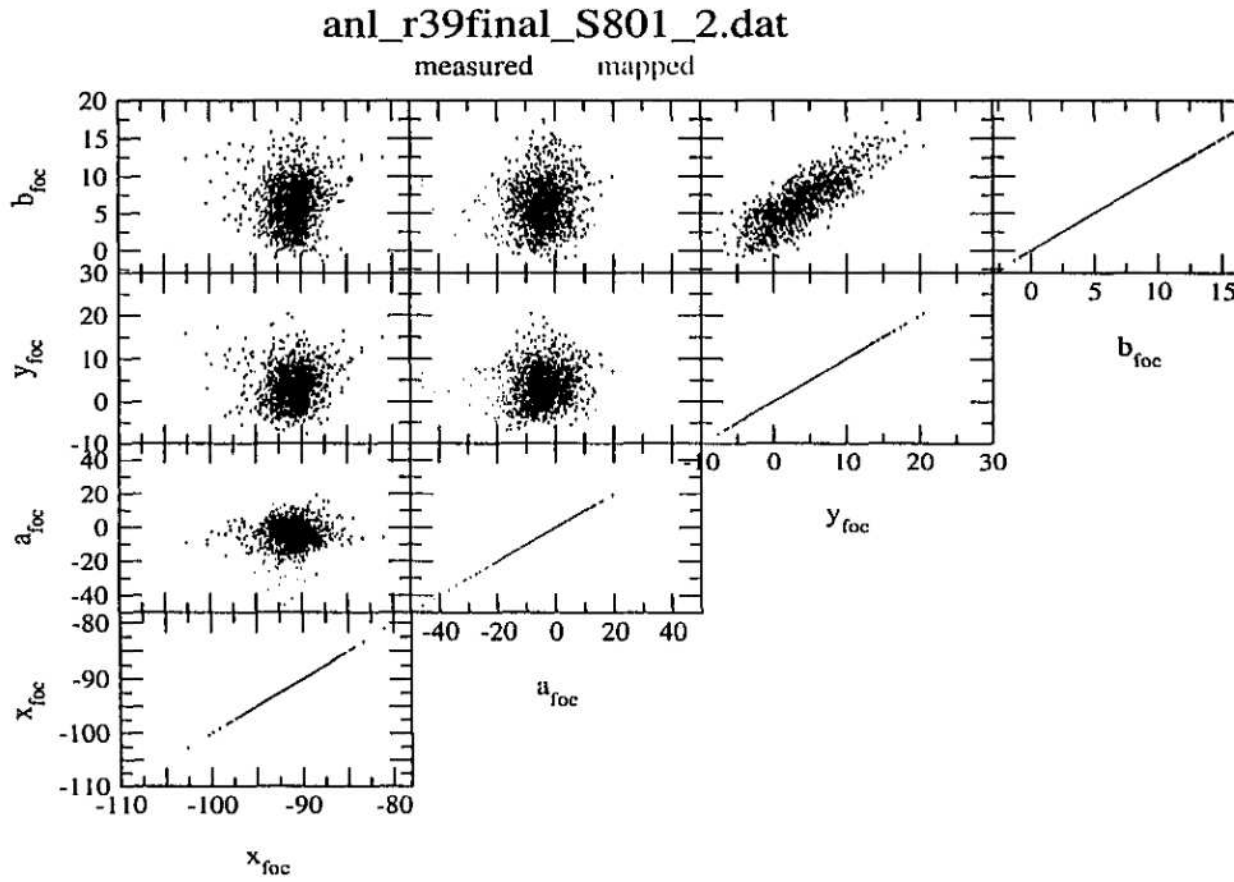
measured   mapped

Figure 5.14. Focal plane phase space from the adjusted map. Black points are data, red points are mapp
to obtain a predicted focal plane profile. The full range of the mapped y and b match the measured data
than the first adjustment.

cus than the ^{9}Li beams. Therefore, if these modifications are due to a systematic failing of COSY, we would expect the over-prediction of the $(y|b)$ dependence to be about the same, but perhaps larger than was found for the ^{9}Li based on scaling arguments. Examining the ^{11}Li data with no target in place, it was found that the forward $(y|b)$ needed to be scaled by 0.6164—a 38% adjustment that is consistent with the ^{9}Li value but slightly larger as expected. As was done with the ^{9}Li, this same adjustment was applied to the ^{11}Li maps when a target was in place.

Even with this significant empirical evidence to suggest that the COSY maps are systematically flawed, it would still be good to justify and/or verify this from an outside source. This has been done, and experimental data from other runs checked. To date, this is the only experiment with tracking detectors in the target chamber to absolutely verify the incident profile. However, other experiments have had extremely thin targets so that the kinematic effects of scattering were plain. It has been found [54, 55] that, for every case, the COSY-generated inverse map required an adjustment of the $(b|y)$ term by 12–20%. These data were also taken at $B\rho$ settings much smaller than our data, and it has been established that the quality of the IGOR-COSY method deteriorates as the strength of the fringe fields increase. Therefore we should not be concerned about making slightly larger adjustments than have been seen before, but rather be encouraged that we must modify the same element and seem to be witnessing the same failing.

However, since such large adjustments are necessary in the first-order map, it is nearly useless to explore higher orders in detail, since they are only progressively finer adjustments to correct aberrations. If COSY fails to generate a correct first-order map, there is no reason to expect it to produce a correct second, third or higher order transfer map. Nevertheless, to cover all the bases, 3rd and 5th order maps were generated (maintaining the $(y|b)$ scaling obtained above) to see if any

98

improvement could be made. None was noticed. The resolution remained the same regardless of order. Thus the first-order terms are completely dominant, and the hope of using COSY to correct the higher-order aberrations inherent in the S800 Spectrograph was futile for the 0° data.

5.4 Gating

Even with transfer maps that provide an accurate description of the ray propagation through the S800 Spectrograph system, we must still account for events that may contribute to background through poor reconstruction or tracking. If the tracking detectors provide an erroneous target position, the comparison with the ray reconstruction through the inverse map will be wrong. It is also possible that particles near the edge of our acceptance envelope (either in position or energy) may take an odd path through the dipoles or, worse, bounce off the inside of the beam line through the S800, leading to an erroneous trajectory at the exit. This in turn will lead to incorrect reconstruction. Two types of gates were used to eliminate this "noise" from our spectra: simple one-dimensional "window" gates that limit extrema, and more complex, two-dimensional "banana" gates that restrict acceptable dependencies in the phase space. They are discussed in turn. One important criterion was held for all gates: it is imperative that they not introduce bias into the results. Since the focal plane position may depend on scattering that takes place, an ill-considered focal plane gate could unwittingly cut out some important aspect of the data. Gating only on the incident parameters eliminates the chance of introducing such a bias because the scattering takes place after the gate has been applied.

5.4.1 Window regions

The simplest window gate that was applied was a cut on the time-of-flight (TOF) as measured by the beam line timer (BLT). Even though we lack a solid calibration

in terms of ns/ch for this device, it can still be used for diagnostic purposes. We cut on the TOF region around the direct beam pulse in order to eliminate beam contaminants. This cut alone improved our beam purity from 99.5% (see §3.1) to 100%.

The next gate was a combination of two gates related to the target y position. First, we simply required that the beam track to inside the target frame. Second, we required that the difference between the reconstructed and measured y positions, $\Delta y = y_r - y_m$, was a relatively small amount consistent with any expected uncertainties due to tracking, multiple scattering in the target, and the transfer map. This immediately eliminated most events with poor angular reconstruction, since if the transverse position on the target cannot be determined accurately, there is little hope of accurately determining the scattering angles, Δa and Δb. Even though this cut indirectly relies on focal plane information, it remains safe from bias since scattering is independent of target position.

In the bend-plane, upper-limit window gates were placed on a and x. It was found that, for runs with no target in place, a large portion of the data that reconstructed to large scattering angles came from either large values of incident a, x, or both. By limiting the incident range to less extreme values, much cleaner spectra were obtained.

Finally, even though it is not a "gate", per-se, we require a coincidence between all four CRDC detectors to allow complete reconstruction and tracking. For the 5° data, the increase in angular resolution provided by the tracking detectors was not required and the coincidence condition was relaxed to only require both focal plane CRDCs to allow ray reconstruction.

5.4.2 Banana regions

A banana gate drawn in the incident y-b plane was used for both Li isotopes in this experiment. This not only eliminated events with odd tracking, but also limited the incident b range analogous to the limitation of incident a set by its upper-limit window. This banana gate eliminated over 90% of the poorly-reconstructed data while only rejecting $\approx$15% of the total events.

The ^{9}Li analysis also employed a second banana gate. It was discovered that events with large Δy typically came from extreme y positions at CRDC S802. A window was drawn in a region of Δy vs. y_{802} to further enhance the reliability of the ^{9}Li data.

5.4.3 Energy cuts

One of the primary goals of this experiment was to separate true elastic scattering from inelastic contributions. Therefore cuts on the δ spectrum were used to construct angular distributions based on the process that led to it. For 440 MeV ^{9}Li the energy of the first excited state of the projectile is 0.6% that of the beam and the first excited state of the target falls at 1.0% that of the beam. For gating around these states we placed cuts at $\delta_E < 0.65\%$, $0.65\% < \delta_E < 1.65\%$, and $\delta_E > 1.65\%$ levels corresponding to the ground state of ^{9}Li, the 2^+ state of ^{12}C, and higher states of ^{12}C, respectively. For the ^{11}Li beam, which had an incident energy of 550 MeV, the excited states of the ^{9}Li core and the target occur at 0.5% and 0.8% respectively. Thus our gates were placed at $\delta_E < 0.4\%$ and $0.4\% < \delta_E < 0.75\%$.

5.5 Kinematic corrections

For the 5° data, the energy lost traversing the target is not negligible. It is enough to disrupt the dispersion-matching of the spectrograph. The problem is that for 450

101

MeV ^{9}Li, a 1.0% spread in energy incident on the 890 mg/cm^2 target results in an exit spread of nearly 1.4%. This leads to a significantly different position-momentum dispersion relation than the S800 expects and will disrupt the focusing. Fortunately, since the incident dp/dx is known, we can calculate on an event-by-event basis the extent of this effect and correct the focal plane x and a measurements accordingly before applying the inverse map.

We are not out of the woods yet, so-to-speak, with kinematic corrections. With the S800 at 5° our measured scattering angles are $\approx$5–15° in the c.m. frame. This is where energy differences due to scattering kinematics become visible with our system. Thus, we have to apply a two-pass method of calculating the scattering angle for the 5° data. The first pass uses the dispersion-corrected position (above) to determine a preliminary scattering angle, which can be used to further correct the focal plane measurements. The second pass uses these new measurements to compute a final scattering angle.

5.6 Scattering angles

5.6.1 Determination of angles

There are various methods of determining the scattering angles. A simple method, which is the basic method of S800 analysis, is to simply take the reconstructed a and b from the inverse map and add them in quadrature to obtain

$$\theta = \sqrt{a^2 + b^2}. \tag{5.7}$$

Eq. (5.7) is simple and straight-forward, but lacks precision. We improve things greatly by using information from the tracking detectors as well. Using the incident measured angles a_m and b_m, and their map-reconstructed counterparts a_r and b_r,

102

we have

$$\Delta a = a_r - a_m$$
$$\Delta b = b_r - b_m$$

(5.8)

which can then be summed in quadrature as above to obtain

$$\theta = \sqrt{\Delta a^2 + \Delta b^2}.$$

(5.9)

However, this too can be improved upon. We take advantage of COSY's native angular units and construct unit vectors for the incident and reconstructed rays. Their components are given by:

$$dz_{i,r} = \frac{1}{\sqrt{a_{m,r}^2 + b_{i,r}^2 + 1}}$$
$$dy_{i,r} = b_{i,r}\, dz_{i,r}$$
$$dx_{i,r} = a_{m,r}\, dz_{i,r}.$$

(5.10)

Then the dot-product relation can be exploited, yielding

$$\theta = \arccos\left(dx_i dx_r + dy_i dy_r + dz_i dz_r\right).$$

(5.11)

The results of calculating the scattering angle by the methods of Eqs. (5.7), (5.9), and (5.11) are shown in Fig. 5.15. The figure begins with the simplest method on the bottom, ending with the full dot product calculation at the top. It also shows the effect of multiple scattering in the target by comparing a sample of data with no target in place (left panes) to true scattering data near $0°$ (right panes). There are several important features to be noted in these plots. First, for angles this far forward, since $\sin\theta \approx \theta$ there is a small but calculable difference between using the complete dot product calculation of Eq. (5.11) or using the differences between the incident and reconstructed a and b, as in Eq. (5.9). There is a noticeable difference, however, in using the tracking information to improve the results of simple ray-reconstruction. In comparing the angular distribution from the direct beam
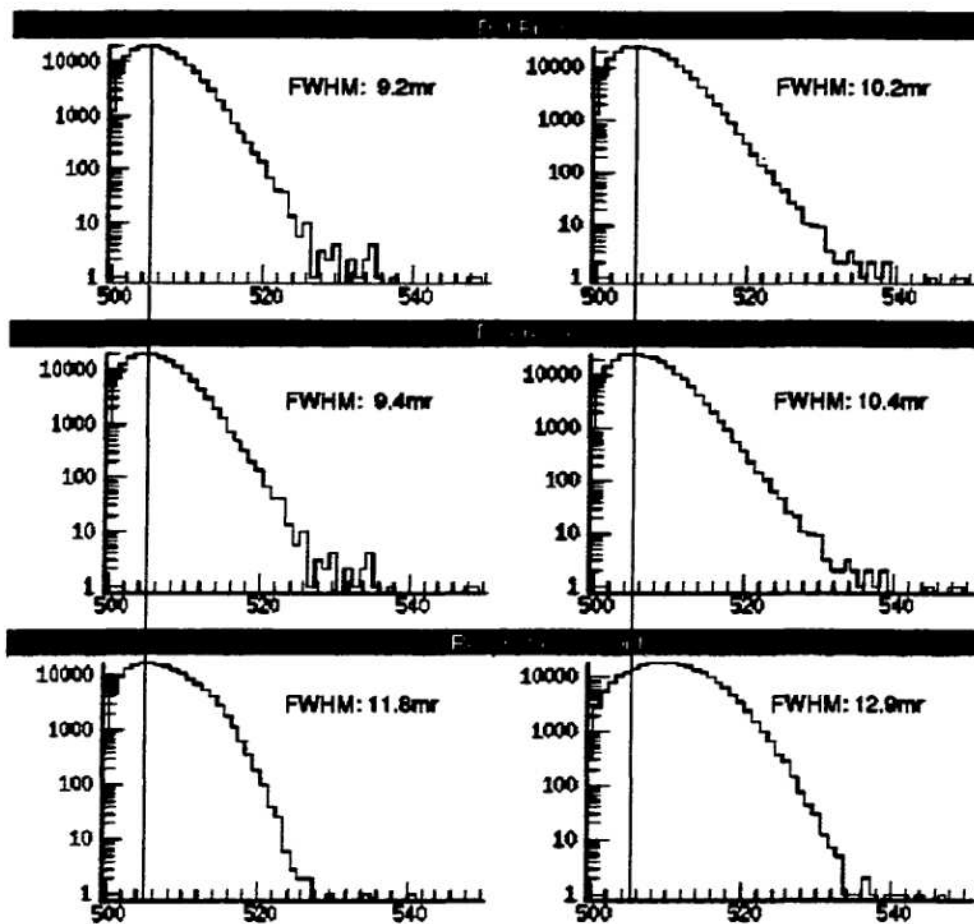
103

Figure 5.15. Comparison of various methods for obtaining the angular distributions. Direct beam (no target) data are in the left panes, 0° scattering data appear in the right panes. See text for discussion.

104

data to the scattering data, we see the same relative improvements in terms of the FWHM, and the scattering data are consistently 1 mr wider. This would imply 4–5 mr of multiple scattering in the target whereas calculations from STOPX [39] predict around 7 mr. The dramatic improvement to be gained from using the tracking detectors becomes apparent when the target is in place. For reference, a vertical line has been drawn through the distributions at 5 mr, which is the peak for both the direct beam and scattering data using the dot-product method. Now, at 0°, the data must be completely dominated by direct beam, and we should be able to recover the direct beam profile—especially since we know from STOPX calculations and the no-target data that the multiple scattering is only about half of our resolution from the mapping. Clearly, using the tracking detector information allows us to do this, providing proof of the method.

5.6.2 Results

5.6.3 Energy resolution

In Fig. 5.16, we show the energy spectra of a direct beam run and a run with the $180 \, \text{mg/cm}^2$ target in place. The direct beam spectrum reveals an intrinsic energy resolution of 0.086%, or 340 keV, for the ^{9}Li, and 0.129% (640 keV) for the ^{11}Li. These resolutions can be seen to be essentially δ functions compared to straggling effects in the target.

5.6.3.1 Basic scattering distributions

The scattering distributions for the ^{9}Li data taken at 0° with and without a target are depicted in Fig. 5.17. As expected, the data are dominated by direct beam events. After subtracting the contribution from the direct beam, there remains only a limited range of angles over which to construct an angular distribution. A similar situation occurs with the ^{11}Li data at 0° as well, shown in Fig. 5.18. We will explore

105
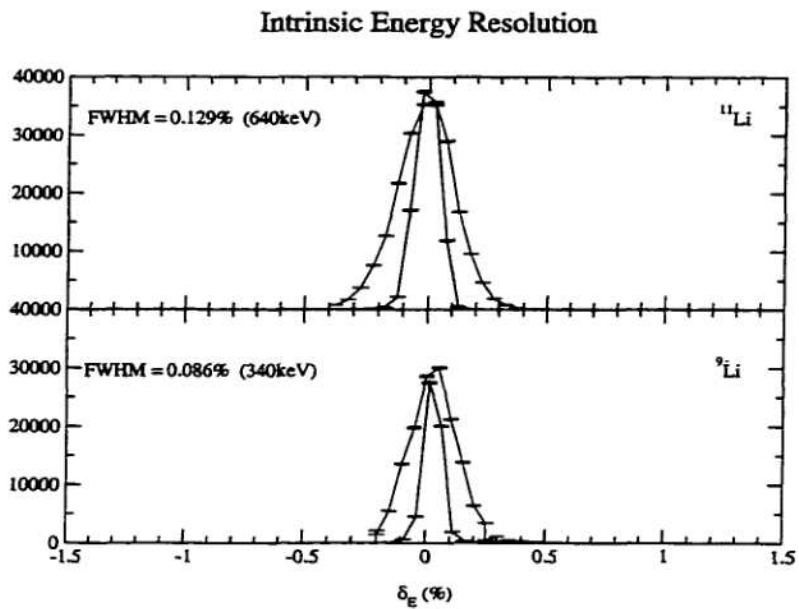
Figure 5.16. Energy resolution of the secondary beams in this experiment plotted as a percentage of the central energy for each particular beam. Direct beam data are given in black, with their corresponding FWHM values listed. The broadening due to target effects is illustrated in grey. The data sets have been arbitrarily normalized to approximately equal peak heights for illustrative purposes.

106
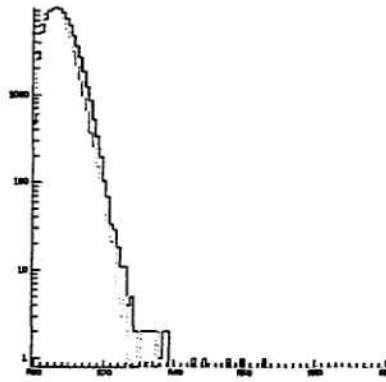
Figure 5.17. Raw scattering distribution for ^{9}Li comparing the no-target run to the reliable target data at 0°. The no-target run is depicted by the lighter histogram.
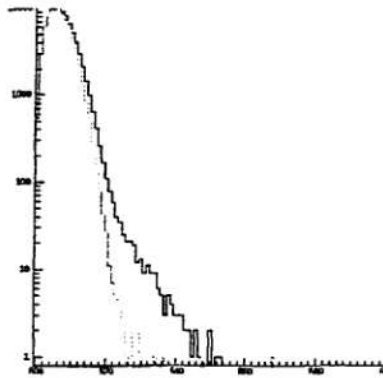
Figure 5.18. Raw scattering distribution for ^{11}Li comparing the no-target run to target data at 0°. The no-target run is depicted by the lighter histogram.

situation occurs with the ^{11}Li data at 0° as well, shown in Fig. 5.18. We will explore these distributions in more detail in the Monte Carlo analysis of the next chapter.

5.6.3.2 Energy cuts

Referring to the predicted cross sections from prior studies [56] shown in Fig. 5.19, we would expect to start seeing contributions from the inelastic channels at angles greater than 25 mr in the laboratory frame. Therefore we placed an angular cut on the data to look at only those events and their associated energy spectra. For the

107
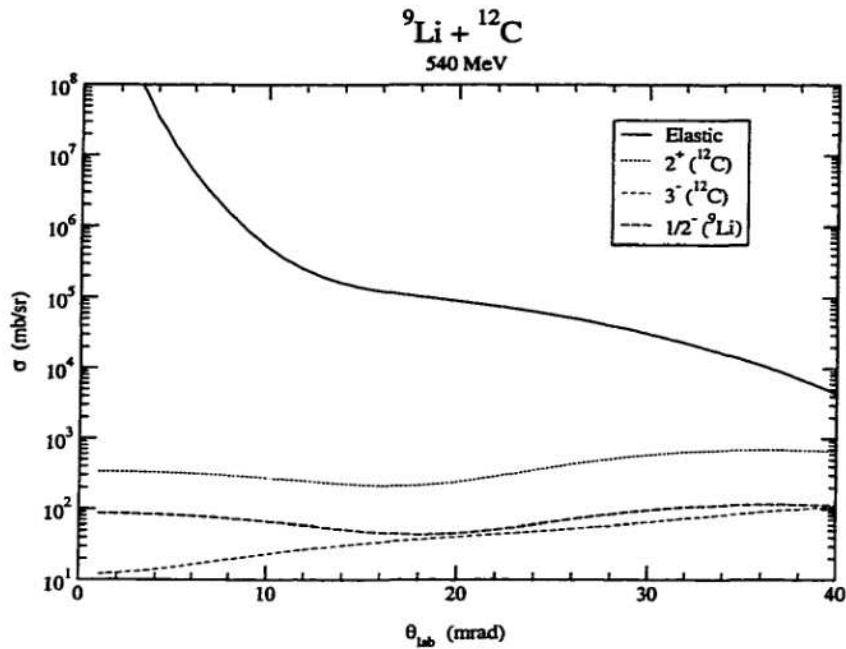
$$^9\text{Li} + {}^{12}\text{C}$$
540 MeV

Figure 5.19. The predicted cross sections for $^9\text{Li} + {}^{12}\text{C}$ from [56]

when the BARNEY readouts were clearly wrong (which required us to make further assumptions regarding the transfer maps) and one set for data taken later when the readouts were apparently valid. The energy spectra for these two sets are shown in Fig. 5.20. It is immediately apparent that there is something fundamentally different between these two run conditions. The early data show a large enhancement around 2.4 MeV, which is where the $1/2^-$ first excited state of ^9Li occurs. However, there is little or no indication of the ^{12}C 2^+ excited state at 4.44 MeV. The later data show no indication of any inelastic events occurring. We further investigated the early data by tracking the energy dependence. By breaking up the data into 10 mr ($\approx 0.5^\circ$) bins in the laboratory frame, we find, as shown in Fig. 5.21, that the putative ^9Li excited state does not track with proper kinematics. In fact, the so-called "ground state" from this data appears to *gain* energy as the scattering angle

108
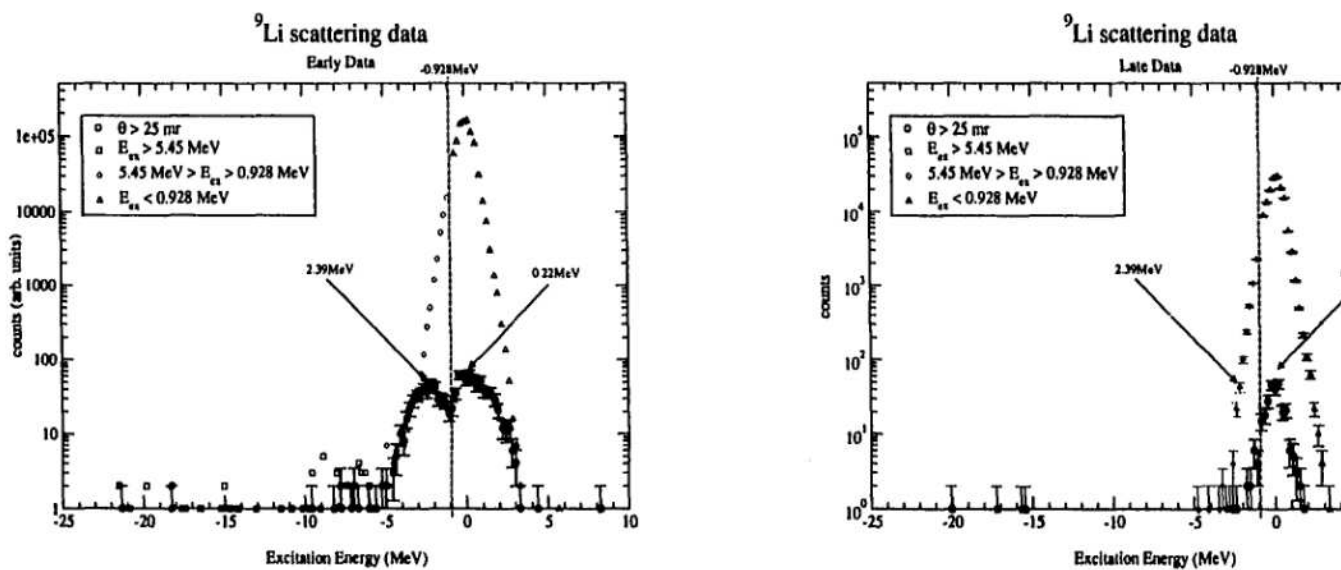
Figure 5.20. Energy spectra for ^{9}Li data from early (left) and late (right) runs illustrating the difference between the two settings.
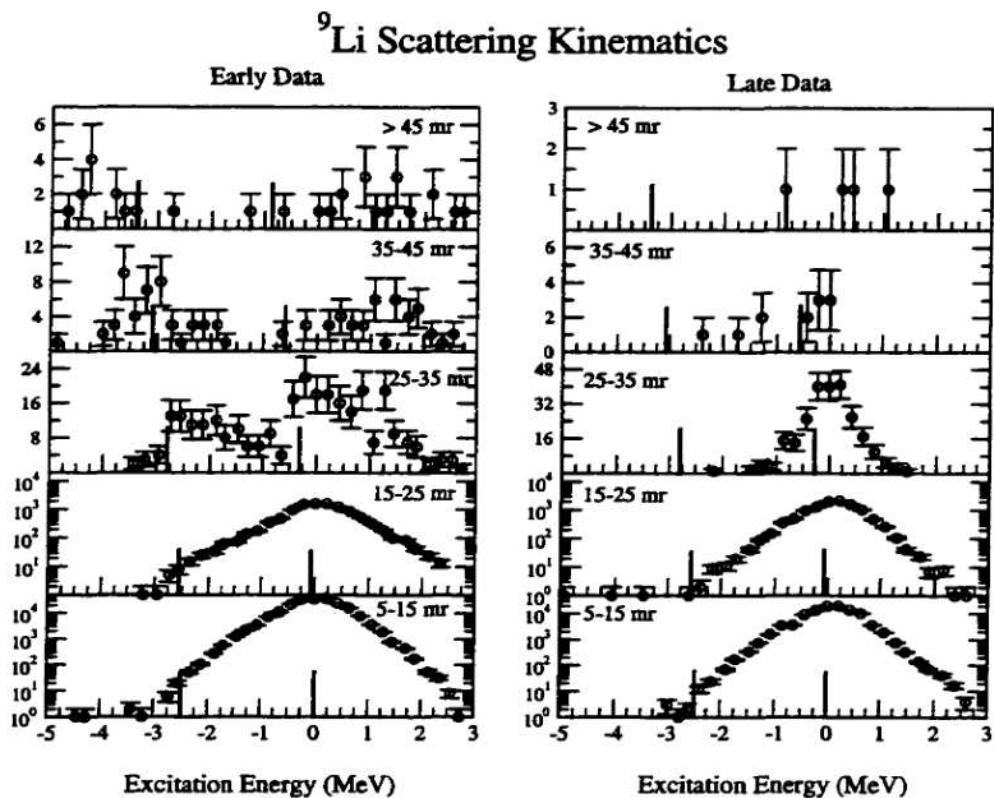
Figure 5.21. The scattering kinematics of ^{9}Li for early data (left) where several assumptions were made regarding the transfer maps, and later ^{9}Li data which required fewer assumptions and modifications. Lines illustrating the expected kinematic trends for the true elastic and the $1/2^-$ state of the ^{9}Li projectile are included to guide the eye.

110

increases. Therefore we conclude that this excitation is not real and is an artifact of a poor transfer map. Furthermore, with the kinematics obviously being wrong, there is no clear reason to trust the scattering angles generated from these data, and we must ignore this part of our data set. In contrast, the scattering kinematics of the later ^{9}Li data are found to track properly. The ^{11}Li data, which was also acquired during a time when the BARNEY readouts were behaving correctly, demonstrate proper kinematics as well, further implying that our transfer maps for the early ^{9}Li settings are incorrect, even after applying the corrections mentioned above.

CHAPTER 6

Monte Carlo analysis

This chapter will describe the use of Monte Carlo simulation to model the experimental apparatus, thereby gaining a better understanding of the data. Details specific to the implementation of the Monte Carlo method are provided in Appendix A. We begin with a discussion of how the simulation was used to determine the parameters associated with the beam and spectrograph and their associated uncertainties. Then we show some results regarding the acceptance effects on the data. We continue by demonstrating the ability to model the direct beam contributions to the data in determining the true scattering cross section. Finally, we conclude the chapter by showing the final cross sections, as ratios to the Rutherford value. The discussion will be generic since both ^{9}Li and ^{11}Li data sets were analyzed similarly.

6.1 Determination of initial parameters

First, the data with no target in place were analyzed. With no scattering taking place, we can be sure that any differences between the transfer-mapped data and measurements are due to uncertainties in the maps or measurements alone. The incident spot sizes and divergences were initially chosen to nearly match the measured distributions, and all uncertainties were set to zero. These were then propagated through the S800 system and the resulting focal plane distributions examined. Neither the transfer maps nor the CRDC [40] detectors are perfect, and thus have

112

Table 6.1. Beam parameters used in Monte Carlo simulations. Positions and divergences are given as FWHM values. Locations and trajectories are that of the central ray.

Description	Size x(mm)	Size y(mm)	Location x(mm)	Location y(mm)	Divergence a(mr)	Divergence b(mr)	Trajectory a(mr)	Trajectory b(mr)
^{9}Li no target	1.10	1.50	-2.00	2.30	10.00	13.20	2.50	1.00
^{9}Li target	1.90	2.70	-1.58	1.80	9.60	10.00	2.70	1.70
^{11}Li no target	4.05	5.00	-0.30	1.10	9.30	7.35	1.85	-0.42
^{11}Li target	4.65	6.20	0.65	3.30	9.85	7.00	4.80	1.25

some error associated with them. These uncertainties serve to broaden the distributions. Therefore the initial distribution widths were adjusted (reduced) until the focal plane distributions predicted by the Monte Carlo simulation were at least as narrow as the data. For similar reasons we must choose intrinsic distributions that are no wider than the measured distributions.

6.1.1 Determination of spot size

First the x-y spot size and location are considered. The y parameter is simple since we can easily examine the empirical distribution on target. The parameters used for the various runs are summarized in Table 6.1. Determining the x spot size is more subtle since the measured x distribution on target is the convolution of the intrinsic spot size and the energy spread, due to our use of the dispersion-matching technique. From the measured x-p correlation in the data, we compute the energy (momentum) contribution to the spot size. Then we can deduce the intrinsic size that, folded with the measured dispersion, yields the observed x distribution.

6.1.2 Determination of divergence and correlations

A complete emittance profile requires knowledge of the divergence of the beam, as well as its size and location. As with the y size, the b distribution is relatively

113

straightforward as it is in the non-dispersive direction. We use the measurements from the incident distribution to initialize the simulation. The a distribution, as was the case with x, is folded with the momentum distribution and a similar method of unfolding is used to obtain an intrinsic distribution.

There are also correlations between certain pairs of parameters that must be controlled. We can measure the y-b correlation directly from the data, obtaining a correlation angle that can be used in the Monte Carlo simulation. For x and a, which are coupled to the incident δ, we must make some other measurements and assumptions. We know approximately what these should be from ion-transport calculations. We can also measure the $(x|a)$ correlation and make use of the knowledge of $(x|\delta)$ gained from examining the forward maps (§5.3.3.2). These measurements provide good initial starting points, but eventually our final choice of dispersion relations comes from using the transfer maps of §5.3.3.2 and the data to determine the best set of self-consistent values.

6.2 Determination of systematic uncertainties

After the initial parameters have been chosen and constrained by the resolution condition of §6.1, the target uncertainties, which are only associated with the tracking detector measurements, can be adjusted until we match the measured incident data. The sources of this error are the uncertainties in the detector measurements in the drift time and the CRDC pad centroid fits (§3.4.1 and 4.1). They can be estimated from the experimental calibration resolutions (§4.2) using error propagation. For the angles, we have

$$\sigma_{\text{ang}}^2 = \left(\frac{1}{d}\right)^2 \left[\sigma_1^2 + \sigma_2^2\right] \tag{6.1}$$

where d is the distance between the detectors and σ_1 (σ_2) is the standard deviation of the measurement of position at the upstream (downstream) detector. For the

114

tracking detectors in the target chamber, the separation distance was 303 mm. We assume equal response from both detectors. This allows us to rewrite Eq. (6.1):

$$\sigma_{ang} \, [mr] = 4.667\sigma \tag{6.2}$$

with σ given in mm.

The target position is obtained by projecting the tracked ray. With a detector separation of 303 mm and a distance of 83.2 mm from the exit of S804 to the target position, we have

$$target = S_{803} + 1.274(S_{S804} - S_{803}) \tag{6.3}$$

which has an associated error of

$$\sigma_{pos}^2 = (0.274\sigma_3)^2 + (1.274\sigma_4)^2 \tag{6.4}$$

where σ_3 (σ_4) is the uncertainty in position measurement at S803 (S804). As with the angle measurement, we can obtain a simpler form by assuming equal response from both detectors. In that case,

$$\sigma_{pos} \, [mm] = 1.303 \, \sigma \tag{6.5}$$

where once again σ is given in mm.

Two methods can be used to determine σ in Eqs. (6.2) and (6.5). One method uses the calibration mask (§4.1.3). We know that the physical holes were 1/16″ (1.59 mm) in diameter, yet we measure spots of 2.5–3.0 mm in diameter. This would imply a measurement uncertainty of around 2 mm. By virtue of the fact that the imaged holes of the target mask are circular and not oblong, we assume that the horizontal and vertical errors are similar. The other method is to use the fact that the centroid fits to the charge distributions have typical full-widths at half-maximum (FWHM) of two pads. Since each pad is 0.1″ (2.54 mm), this implies a measurement

115

σ of about 1.75 mm which is consistent with the results obtained from imaging the calibration mask. These two methods, then, in conjunction with Eqs. (6.2) and (6.5), indicate the following errors in the incident distributions:

$$8.2\,\text{mr} < \sigma_{\text{ang}} < 9.3\,\text{mr}$$

$$2.3\,\text{mm} < \sigma_{\text{pos}} < 2.6\,\text{mm}. \tag{6.6}$$

Finally, the focal plane distributions from the simulation can be matched to the data by adding uncertainties. The focal plane data have uncertainties associated with both measurement and ray-tracing. We must determine reasonable relative contributions from these sources. As in Eq. (6.2), but with a separation distance of 1073 mm, we estimate an angular measurement error in the focal plane of

$$\sigma_{\text{ang}_f} = 1.318\,\sigma. \tag{6.7}$$

Comparing these error estimates to the errors needed by the Monte Carlo simulations to match the experimental data ensures that we are using reasonable parameters. A large source of error comes from the transfer maps used in performing the ray-reconstruction. As discussed in §5.3.3.2, there were several problems in using the "stock" maps generated by COSY—especially in the y-b plane. For determining the error associated with the transfer maps, COSY tells us that the uncertainty in the inverse map (accounting for adjustments to the forward map) is about 8–10 mr in both planes, with a y-position uncertainty of 2–4 mm. We can reasonably assume that the forward map has similar errors and use those as initial values. It is worth commenting that these estimates are consistent with the ranges determined above.

6.3 Consistency checks

After matching the target and focal plane measurements, we examine the reconstructed data from the inverse map. Comparison of these reconstructed parameters

116

Table 6.2. Uncertainties (FWHM) for measurements and transfer maps

Run Type	Location	x(mm)	a(mr)	y(mm)	b(mr)
^{9}Li no target	Forward Map	2.5	4.0	2.0	7.0
	Inverse Map		4.0	2.0	4.0
^{9}Li with target	Forward Map	3.0	3.0	5.0	4.0
	Inverse Map		3.0	4.0	3.0
^{11}Li no target	Forward Map	2.0	4.0	5.0	4.5
	Inverse Map		5.0	6.0	4.0
^{11}Li with target	Forward Map	3	5	6	5
	Inverse Map		5.0	6.0	5.0

with the experimental data further ensures that we have the proper correlations. We determine the error in the inverse map from the difference spectra:

$$\Delta a = a_{\text{inv}} - a_{\text{tgt}}$$

$$\Delta y = y_{\text{inv}} - y_{\text{tgt}}$$

$$\Delta b = b_{\text{inv}} - b_{\text{tgt}},$$

both from the simulation and the analyzed data. As with the direct measurements, inverse map uncertainty is added to each parameter until the Monte Carlo results match the data. Examining these difference spectra also allows us to further tune the target uncertainties for optimal matching of the direct beam data. The final uncertainties are summarized in Table 6.2.

6.4 Direct beam results

The results obtained for both Li isotopes for the runs with no target appear in Figs. 6.1 through 6.8.   It can be seen that overall the simulation does a very good job of replicating the actual data indicating that we have achieved a reasonable understanding of the uncertainties and beam profiles. In every case, the black circles refer to the measured data while the red squares are from the
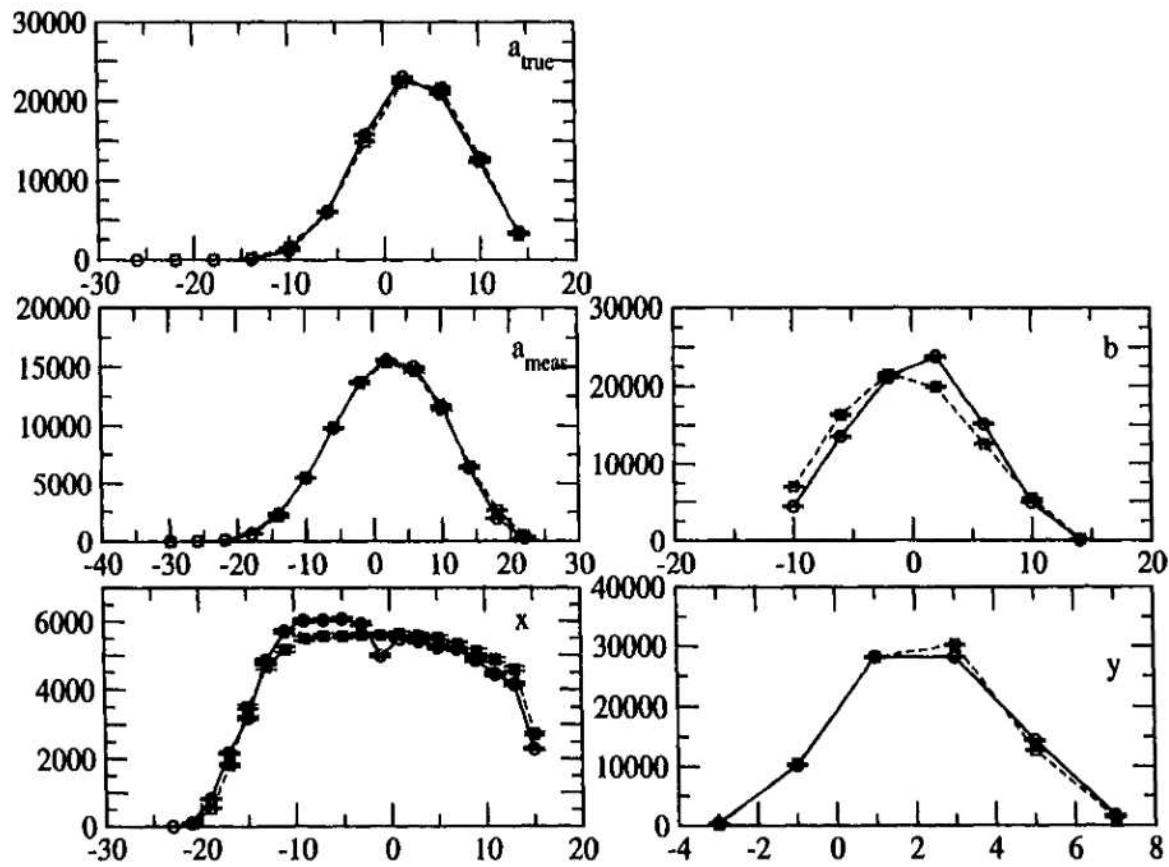
117

Target Parameters (run 39)

Figure 6.1. Monte Carlo simulation for the direct beam (grey squares) compared to experimental data (
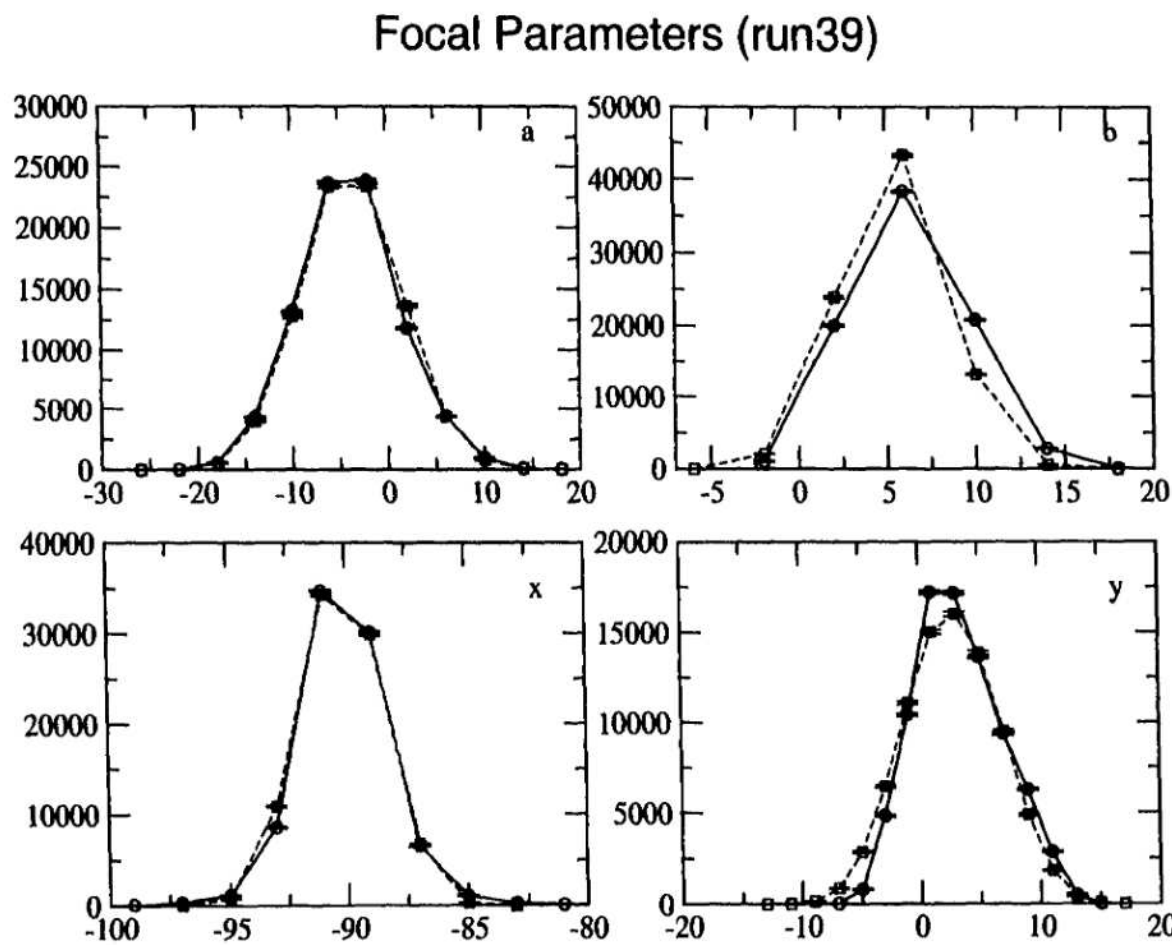target parameters of ^{9}Li. Lengths are in mm, angles are in mrad.

Focal Parameters (run39)

Figure 6.2. Monte Carlo simulation for the direct beam (grey squares) compared to experimental data (
focal plane parameters of ^{9}Li. Lengths are in mm, angles are in mrad.

Reconstructed Parameters (run 39)

Figure 6.3. Monte Carlo simulation for the direct beam (grey squares) compared to experimental data (
reconstructed target parameters of ^{9}Li. Lengths are in mm, angles are in mrad.

Apparent Scattering Distribution

Run 39

Figure 6.4. Monte Carlo simulation for the direct beam (grey squares) compared to experimental data (b observed "scattering" distribution of ^{9}Li. Since there is no target, this spectrum is related to the respo system.

122

Target Parameters (run 42)

Figure 6.5. Monte Carlo simulation for the direct beam (grey squares) compared to experimental data (
target parameters of ^{11}Li. Lengths are in mm, angles are in mrad.

Focal Parameters (run42)

Figure 6.6. Monte Carlo simulation for the direct beam (grey squares) compared to experimental data (focal plane parameters of ^{11}Li. Lengths are in mm, angles are in mrad.

Reconstructed Parameters (run 42)
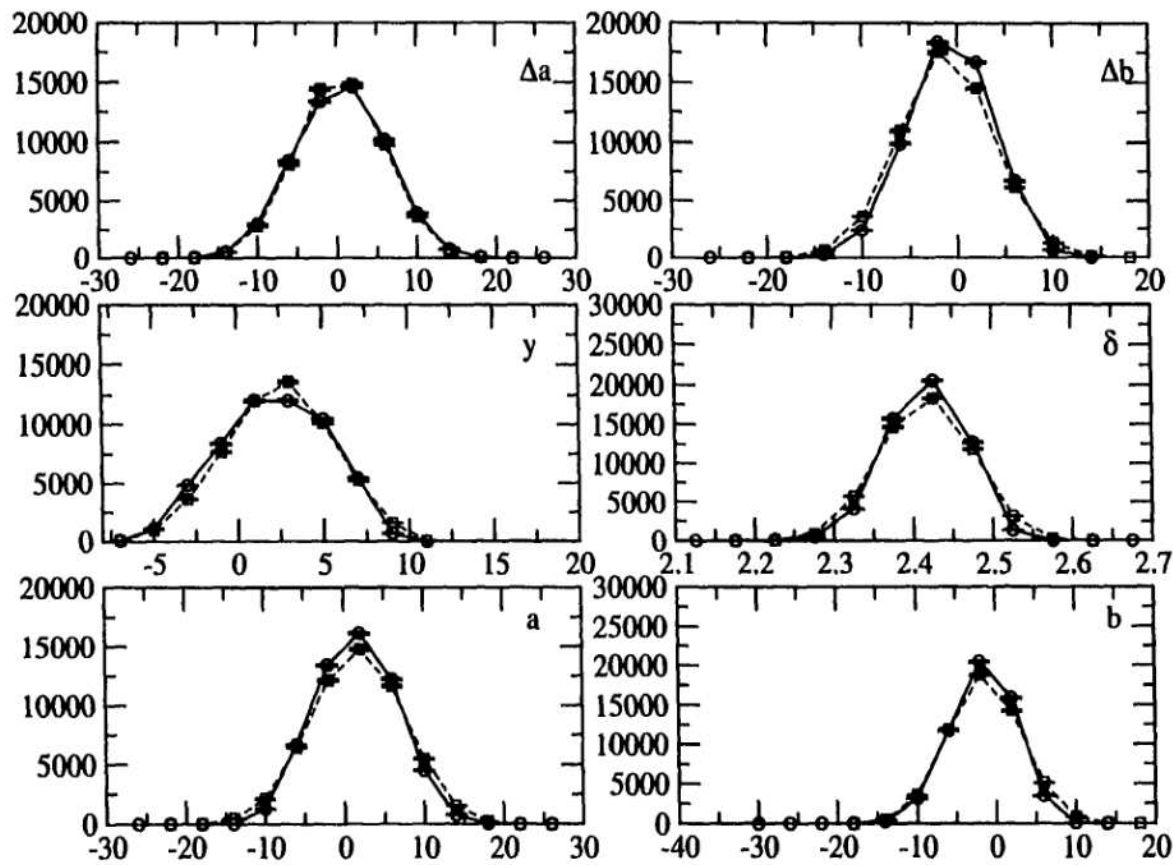
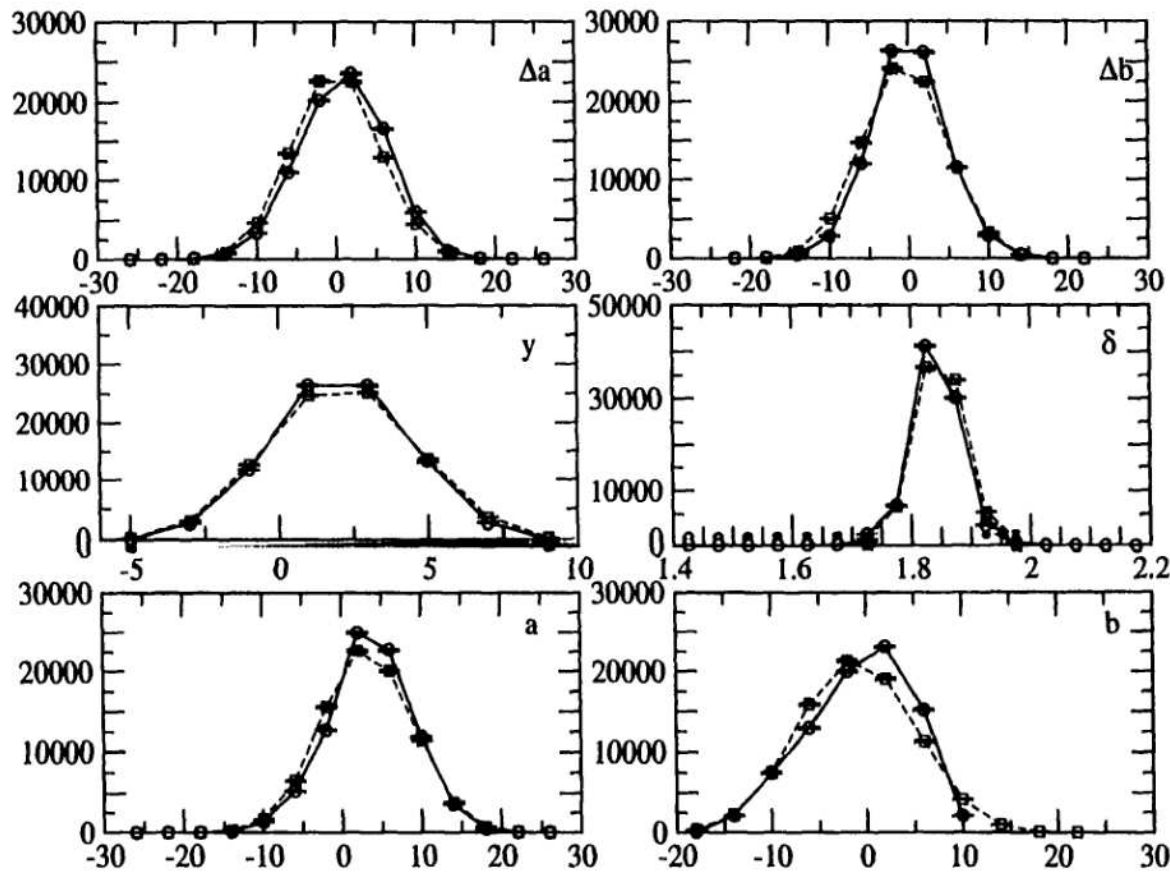Figure 6.7. Monte Carlo simulation for the direct beam (grey squares) compared to experimental data (reconstructed target parameters of ^{11}Li. Lengths are in mm, angles are in mrad.

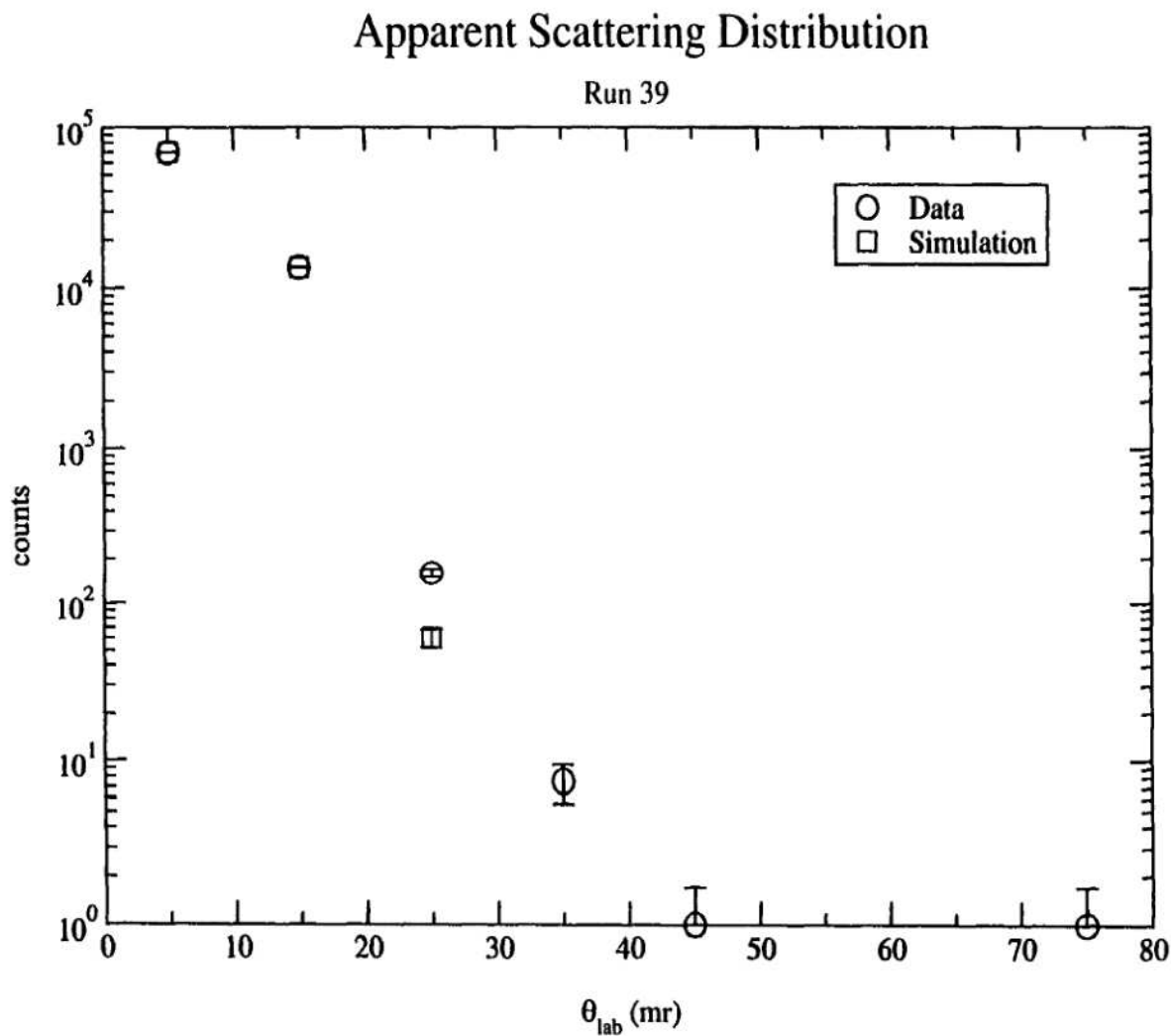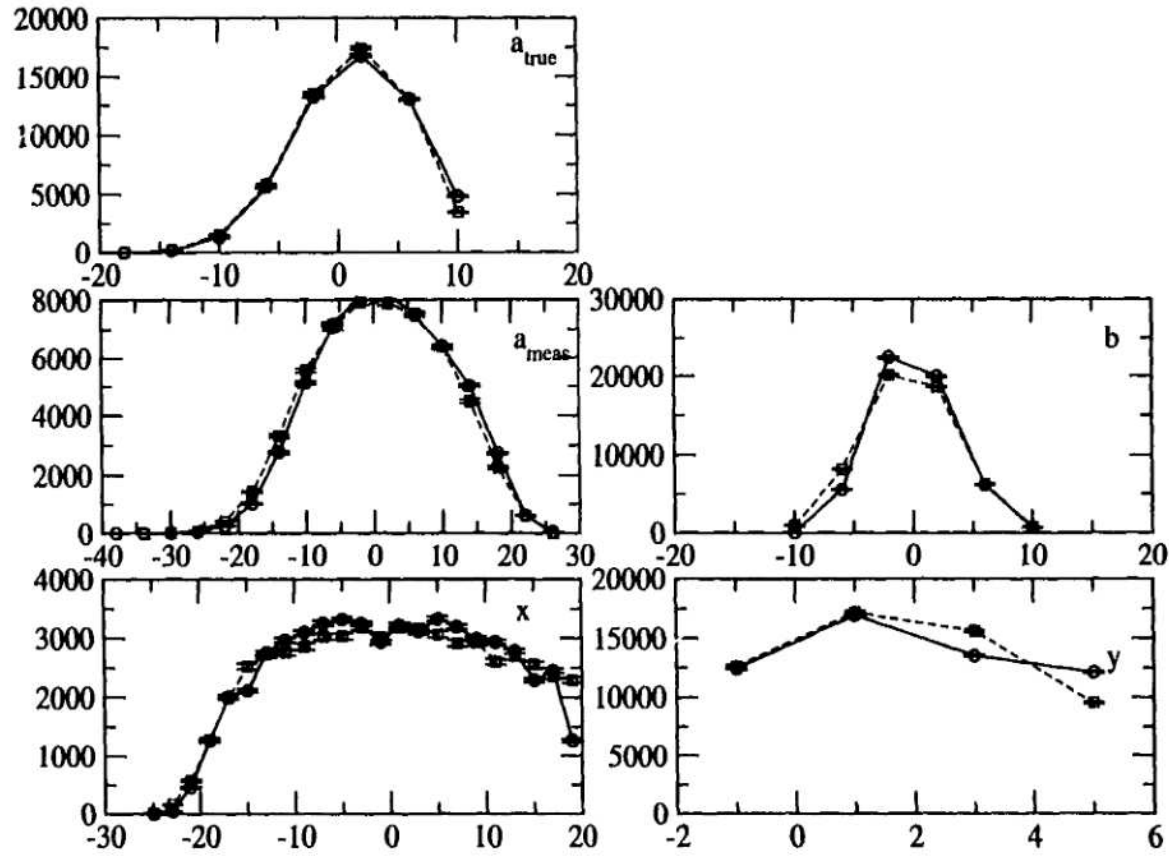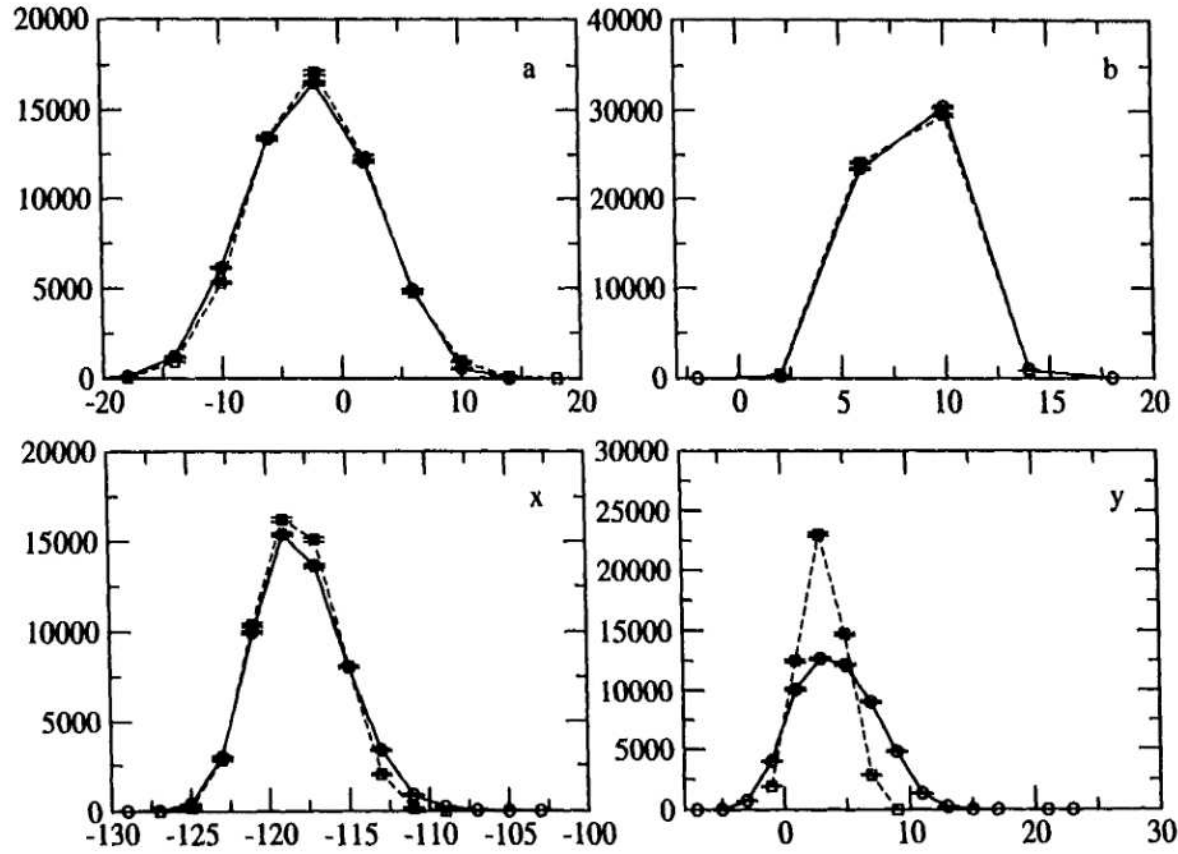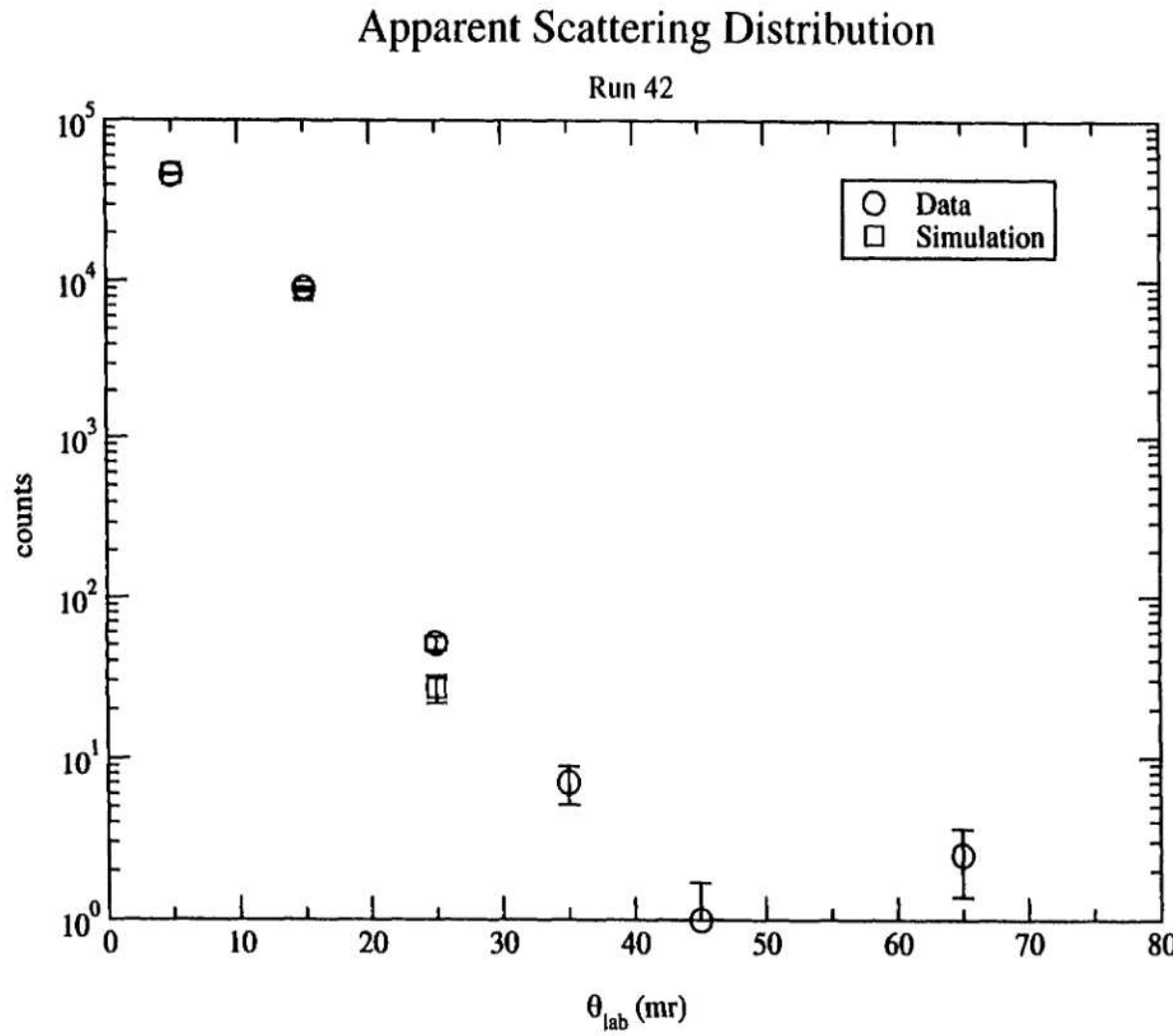## Apparent Scattering Distribution

Run 42

Figure 6.8. Monte Carlo simulation for the direct beam (grey squares) compared to experimental data (observed "scattering" distribution of ^{11}Li. As with Fig. 6.4 this spectrum indicates the response of the sy of a target.

simulation. The only exception to the excellent agreement between the simulation and data is seen in Fig. 6.6. The focal plane y profile predicted from the Monte Carlo is noticeably narrower than that of the experimental data. The reason for this is not entirely understood given that every other parameter is well-matched. This apparent discrepancy does not overly concern us, though, for the following reason. When this seemingly narrow y_{foc} distribution, along with the rest of the focal plane phase space, is processed by the inverse map, the reconstructed parameters (Fig. 6.7) match extremely well. Recall that the importance of the y measurements in the analysis is to place a "goodness of reconstruction" gate that requires the reconstructed y position on target to match the tracked position to a certain accuracy (§5.4.1, p. 100) for us to trust the event. Since both the reconstructed and incident y distributions from the Monte Carlo simulation match the empirical data, we conclude that this is only a minor effect, and is likely due to imperfections in the transfer maps. It does not have any effect in determining scattering angles. There is yet another interesting aspect of the ^{11}Li y distribution. As illustrated by Fig. 6.11 on page 129, the ^{11}Li beam had poorly understood focusing in the y-b plane which resulted in a multi-peaked profile. This profile was treated as several different trajectories, each corresponding to a segment of the total profile, in both the data sorting and in the Monte Carlo analysis. The ^{11}Li results (from data run 42) shown in Figs. 6.5–6.8 reflect only one of those segments.

In examining the distributions of Fig. 6.4 and Fig. 6.8, it is clear that we would not expect to see any counts beyond 30 mr in the lab frame in a direct beam run. However, the data from both beams show a few counts beyond 30 mr. This is an indication of a systematic background due to improper tracking or mapping in the data stream. Thus, in determining a scattering distribution, we not only have to subtract the beam contribution from far-forward angles, but have to account for a

126

background in the larger angles as well. For this purpose an additional background consisting of a shallow exponential tail was added to the beam profile before subtracting that profile from the raw data. The form of this tail was determined from examination of the deficiency of the direct beam alone. Taking Fig. 6.4 as an example, we see that approximately one extra count is needed at 45 mr and nearly 100 additional counts are required at 25 mr. However, a simple addition of this exponential to the existing counts would produce an excess of background in the far-forward points. Using the direct beam to account for only 90% of the events (allowing the exponential to account for the remainder) remedies this situation. A similar method was employed for the ^{11}Li data of Fig. 6.8. The effect of this modification to the ^{9}Li beam profile can be seen in Fig. 6.9, while the corresponding effect for the ^{11}Li profile is shown in Fig. 6.10.

6.5   Scattering

6.5.1   Statistical effects

Once the direct beam is understood through analysis of runs without a target, we can add to the simulation the uncertainties due to statistical effects such as multiple scattering and energy straggling in the target, in order to predict the direct beam contribution to the scattering data.

The multiple scattering FWHM is determined in the following manner. First, the program STOPX [39] is used to provide a basis for how much multiple scattering we might expect for a specific particle-energy-target combination. Then, that number is mildly tuned in order to match the measured forward peak of the scattering data, assuming the same measurement uncertainties as determined from the runs with no target in place. All runs for a given target will use the same value.

To determine energy straggling effects, the code STOPX was again used to deter-
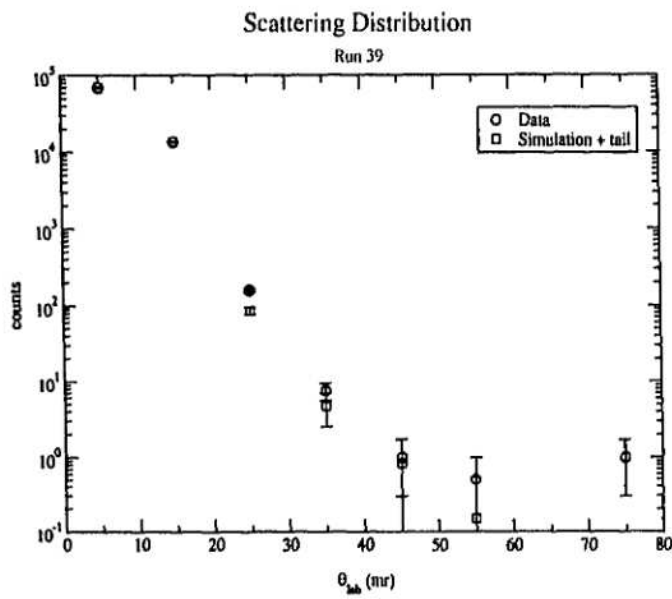
127

128

Figure 6.9. Modified background profile of the beam response calculated with the Monte Carlo plus shallow tail compared with experimental data for the ^{9}Li beam.
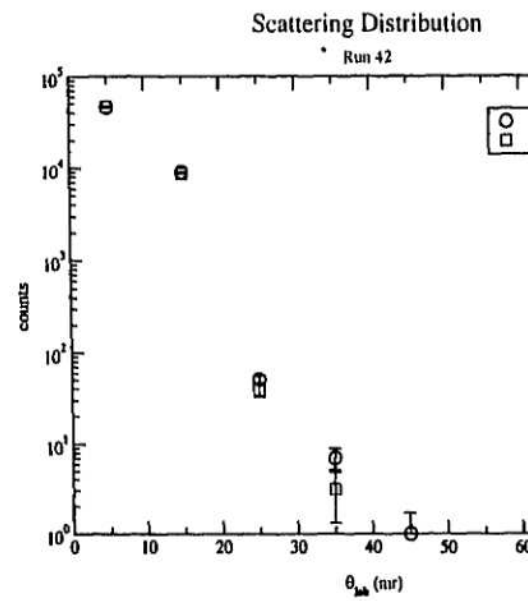

Figure 6.10. Modified background profile response calculated with the Monte Carl tail compared with experimental data for
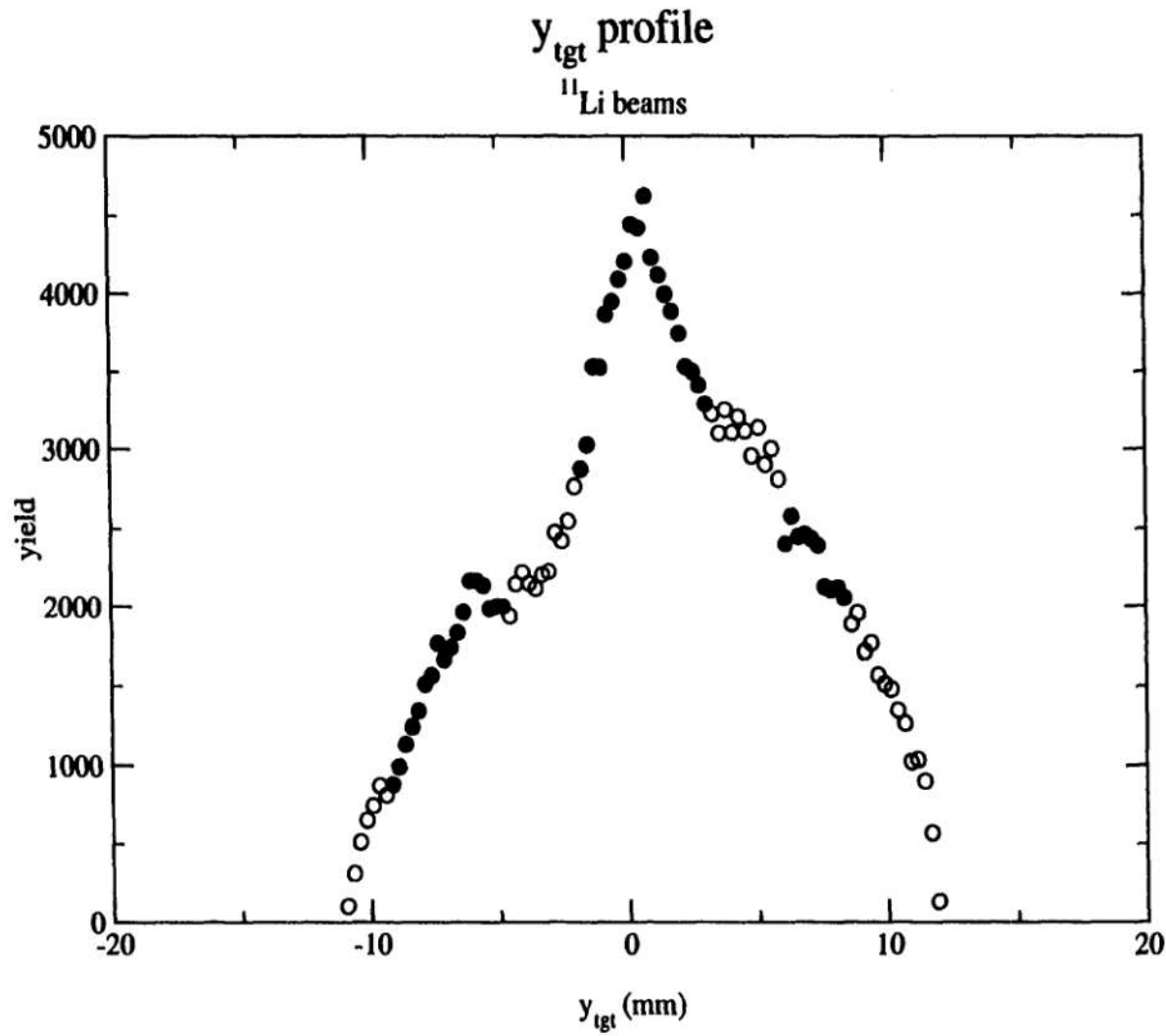
Figure 6.11. The many peaked profile of the ^{11}Li beam. The y profile was separated into pieces as consistent analysis with the Monte Carlo simulation.
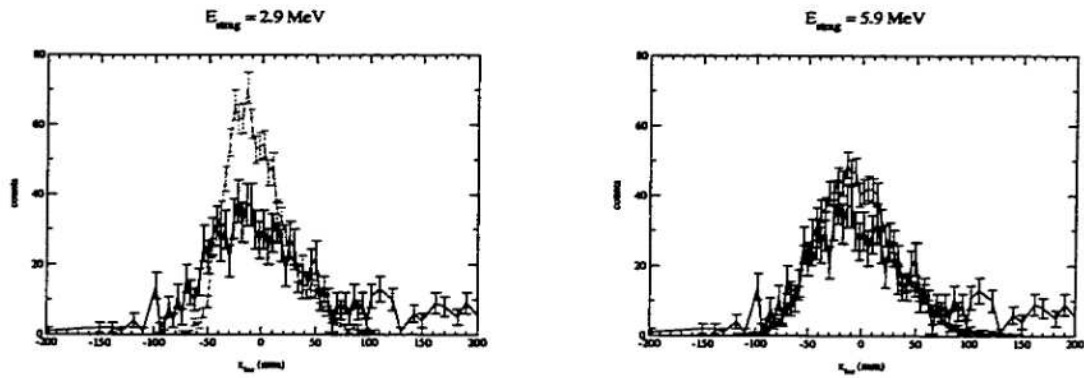
Figure 6.12. Confirmation of the need for a larger value of energy straggling than predicted by STOPX, for the 890 mg/cm²target

mine the expected FWHM for straggling. This number was also tuned for optimal matching of the data. Here we found an astonishing effect in analyzing the 5° data with the thicker (890 mg/cm²) target. While the tuning of the straggling predicted from the 178 mg/cm² target was only a fraction of an MeV different from the value predicted by STOPX, the straggling from the 890 mg/cm² target had to be increased by about 3 MeV—nearly double the predicted value! The evidence for this increase is shown in Fig. 6.12. If we use the value predicted by STOPX, we cannot reproduce the dynamic range of the data seen in the focal plane—especially the events with higher-than-average momentum which appear at negative values for x_{foc}. The larger straggling value provides an enhanced dynamic range and improves the matching quality of the simulation to the data. We explore the appropriateness of this adjustment as follows. The Li beams lose slightly more than 90 MeV in passing through this target. To obtain the total straggling of 6 MeV required to match the data implies an additional 5 MeV of straggling in the target, or nearly a 5% effect. This can be explained through inhomogeneities and imperfections in the target. Target uniformity was only tested by measuring the thickness at several points with a calipers, which does not guarantee uniform density. Of course, this

130

Table 6.3. Statistical uncertainties of the beam parameters

Beam	Target Thickness (mg/cm^2)	Multiple Scattering (mr)	Energy Straggling (MeV) STOPX/empirical
^{9}Li	178	7.5	0.91/1.24
^{9}Li	890	15.0	2.74/5.90
^{11}Li	178	6.3	0.94/1.31
^{11}Li	890	14.8	2.91/6.05

extra straggling has a further, unfortunate, effect on our experiment. Given that the 2^+ state of the ^{12}C target lies at 4.44 MeV, our expected straggling of < 3 MeV would likely cause some overlap between the ground state and excited state, but the two would remain separable. However, with an energy straggling of nearly 6 MeV, these two states become too intermingled to separate by means of an energy cut. We will discuss the methodology used to deal with this problem in the next section. The final statistical uncertainties used in the analysis are given in Table 6.3.

6.5.2 Computing angular distributions

The simulation was run for an appropriate number of iterations to match the forward (direct beam) peak of the scattering data, which was subtracted from the measured distribution leaving only true scattering events. These are then corrected for the solid angle and acceptance efficiency peculiar to the beam profile. Using the known target thickness and number of incident particles, we compute the true angular distribution of the cross section.

For the runs with the S800 Spectrograph positioned at 0° with respect to the incident beam direction, the data are dominated by direct beam and no inelastic excitation is apparent. Nonetheless, we used the energy cut discussed in §5.4.3 to ensure that we were only analyzing (and simulating) ground-state data. This cut eliminated 15–20% of our statistics, but we gain the assurance of analyzing only

131

elastic events.

As mentioned above, it is not possible to simply deconvolute the elastic and inelastic channels via energy reconstruction for the runs with the S800 positioned at 5° relative to the beam axis, due to the larger-than-expected energy straggling from the thicker target. Therefore we measure quasi-elastic scattering for these angles as in the prior study [16]. However, we can improve upon those prior results in at least removing some of the model-dependency from the analysis. Even though it is convoluted due to statistical effects in the target, we nevertheless obtain an energy spectrum from the current data. Furthermore, we can break the 5° data into 20 mr (lab) bins consistent with the resolution of this experiment, and examine the features of the energy spectrum as a function of angle. This allows us to determine at least to some extent the *relative* contributions of each exit channel in the form of an angular distribution, which can be compared with theory. There is one small problem with this method: breaking the data up into angular bins further limits the already meager statistics available to us, making it difficult to obtain a meaningful fit to the energy spectrum. What we can do, however, is to use the ratios of the exit channels as calculated in a specific theory as input for the Monte Carlo simulation. Comparing the Monte Carlo output to the data allows us to at least argue the consistency of theory with experiment. Figs. 6.13 compares the energy distributions, relative to the direct beam, from the experimental data with the Monte Carlo results obtained using the relative ratios predicted by the calculations of Ref. [56, *l*6 potential]. The Monte Carlo results were scaled to the number of counts in the experimental data. All error bars are statistical. Overall the agreement is quite good. There may be some indication that the theoretical calculations expect a little too much ground state in the 60-100 mrad range, but they are not unreasonable—especially given the available statistics in the data. To check our sensitivity to these exit channel
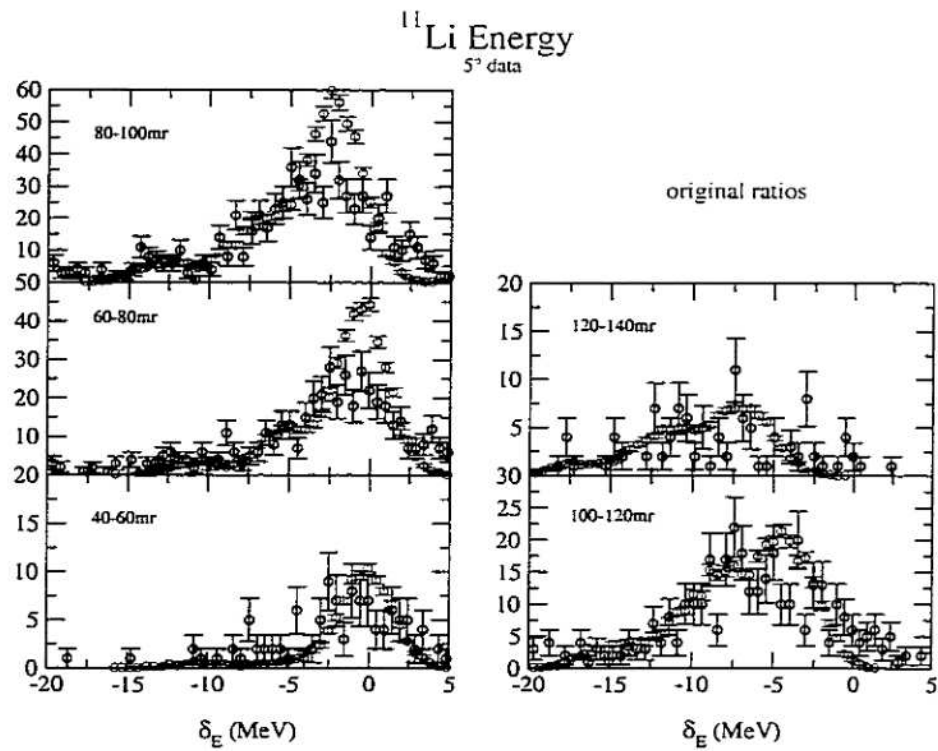
132

Figure 6.13. Comparison of the Monte Carlo simulation using exit channel ratios predicted for ^{11}Li in Ref. [56] with the experimental data. For each angular bin, the black points are the data and the red are from the simulation. The ordinates are in units of raw counts, the abscissas are relative to the central $B\rho$ of the S800.
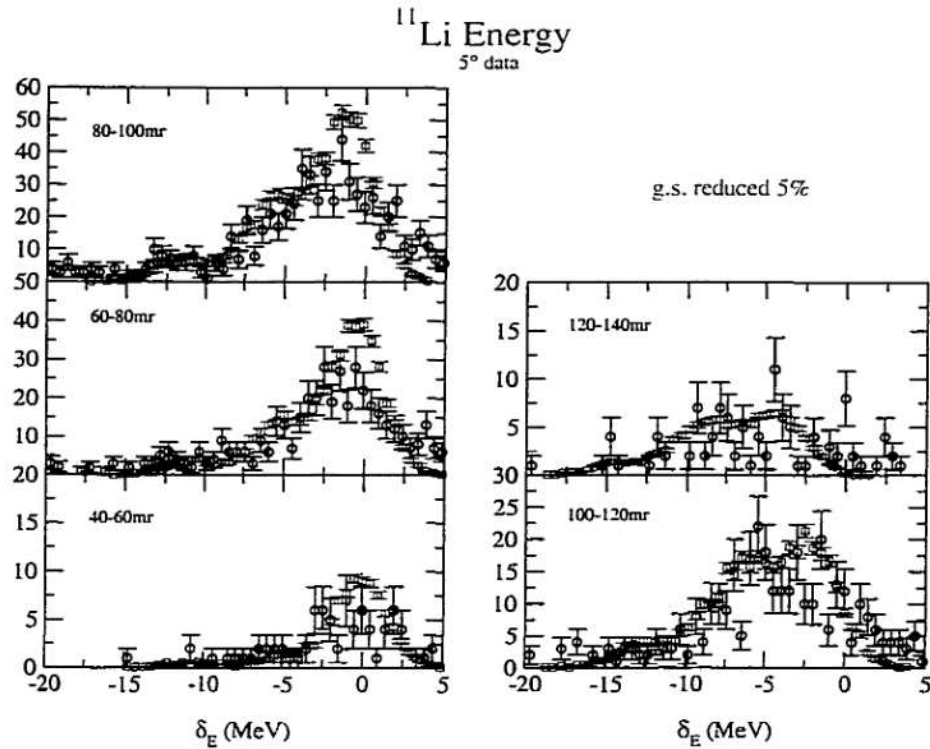
133

Figure 6.14. Energy distributions as in Fig. 6.13 but with the ratios of the ground state and 2^+ state modified by 5%.

probabilities, the simulation was rerun with the ground state contribution reduced (Fig. 6.14) or increased (Fig. 6.15) by 5%, with the difference being added to or subtracted from the contribution of the 4.44 MeV 2^+ state in the target.   These distributions are not inconsistent with the data either; however the increase in the ground state probability produces a peak that appears too narrow in nearly all angular bins, and clearly overpredicts the ground state yield for $\theta > 100$ mr lab. By reducing the ground state contribution by 10% (or more) as in Fig. 6.16 we start to see some inconsistency between the data and simulation. This is especially evident for $\theta > 60$ mr lab where the yield from the 2^+ state is overpopulated compared to the data.   These spectra indicate that this is our approximate sensitivity to
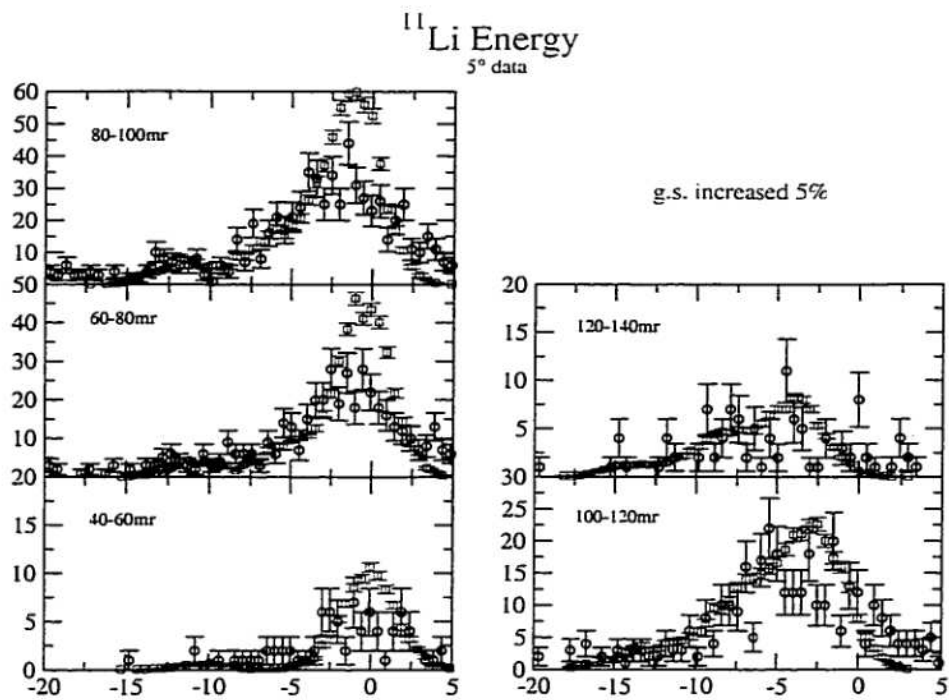
134

Figure 6.15. Energy distributions as in Fig. 6.13 but with the ground state probability increased by 5% over the prediction of ref [56] and the 2^+ state reduced by 5%.
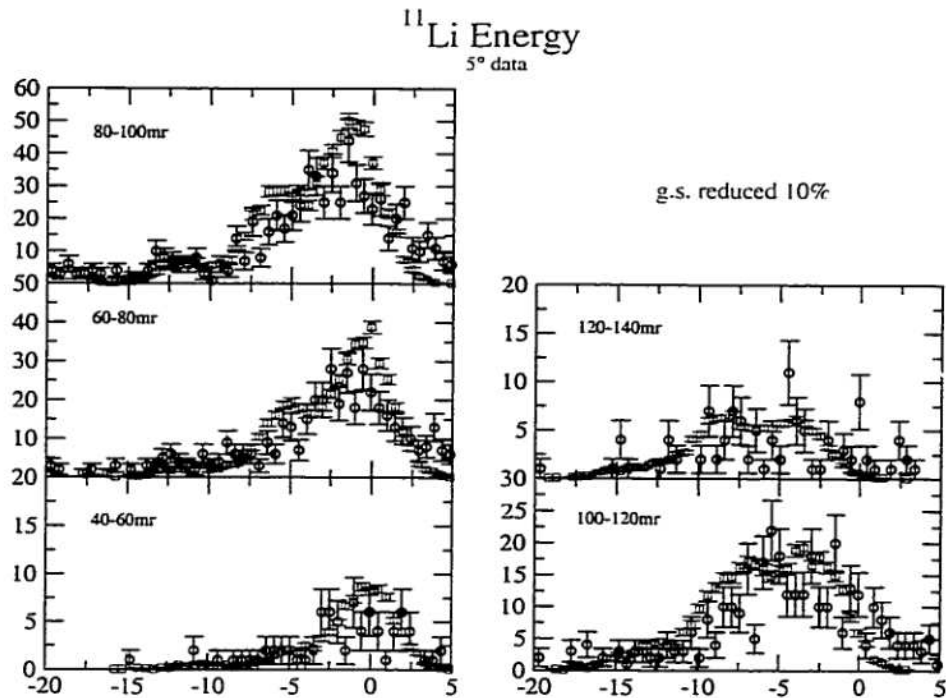
135

Figure 6.16. Energy distributions as in Fig. 6.13 but with the ratios of the ground state and 2^+ state modified by 10%.

the inelastic channels. Thus, we conclude that the relative contributions from the DWBA calculations match the data to $^{+5}_{-10}$% for ^{11}Li + ^{12}C.

The same comparisons can be seen for the ^{9}Li data in Figs. 6.17–6.20. For both the original ratios and either 5% adjustment, the simulation and data appear to be consistent.   With 10% of the ground state contribution removed and added to the 4.44 MeV 2^+ state we can start to see some deviation between the Monte Carlo simulation and the data. For $\theta < 100$ mr lab, the ground state appears to be underpopulated, with a minor discrepancy in the 4.44 MeV region, though one would hardly consider these spectra inconsistent. It is necessary to change the contribution by 20% to see a clear deviation from the data, as shown in Fig. 6.21.
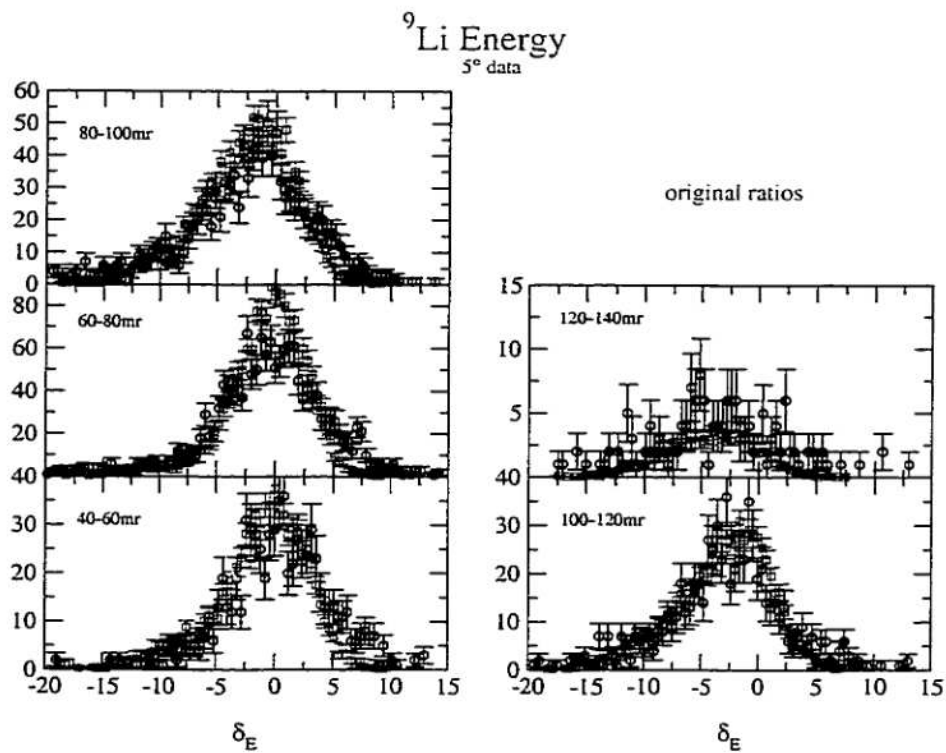
136

Figure 6.17. Comparison of the Monte Carlo simulation using exit channel ratios predicted for ^{9}Li in Ref. [56] with the experimental data. For each angular bin, the black points are the data and the red are from the simulation. The ordinates are in units of raw counts, the abscissas are relative to the central $B\rho$ of the S800.
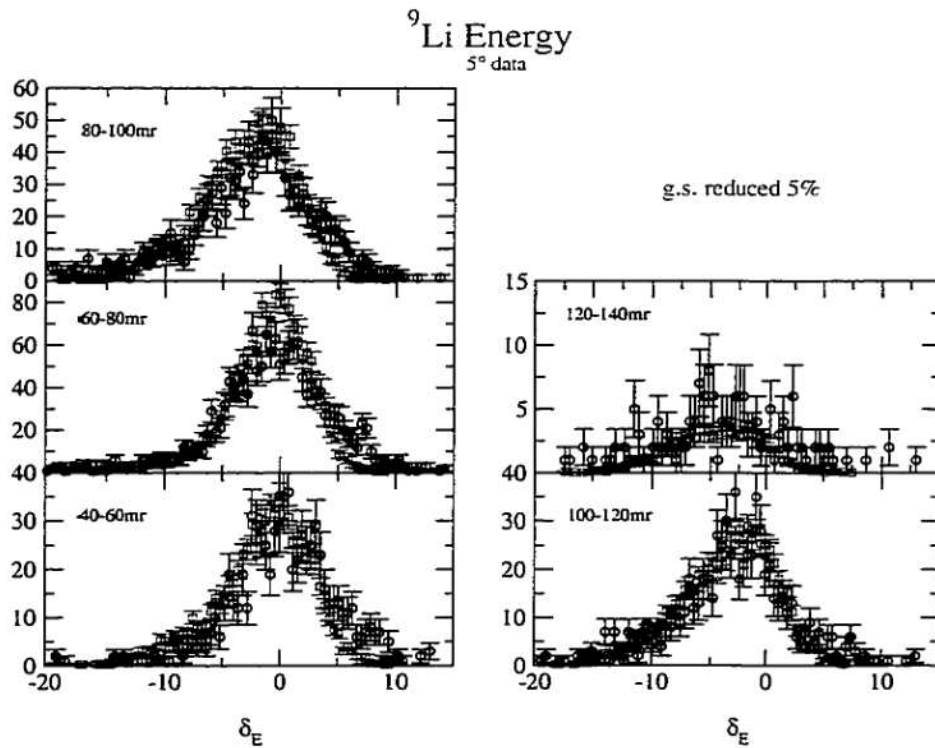
137

Figure 6.18. Energy distributions as in Fig. 6.17 but with the ground state probability reduced by 5% and the 2^+ state increased by 5%.

138

^{9}Li Energy

5° data

80-100mr

g.s. increased 5%

60-80mr

120-140mr

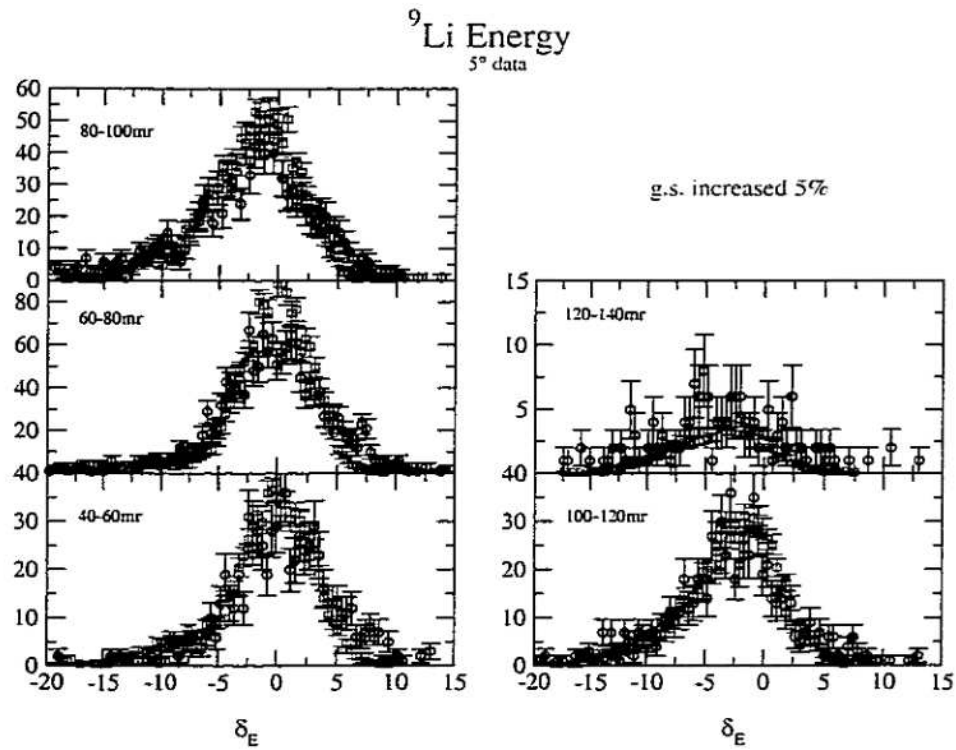40-60mr

100-120mr

δ_E

δ_E

Figure 6.19. Energy distributions as in Fig. 6.17 but with the ground state probability increased by 5% and the 2$^+$ state reduced by 5%.
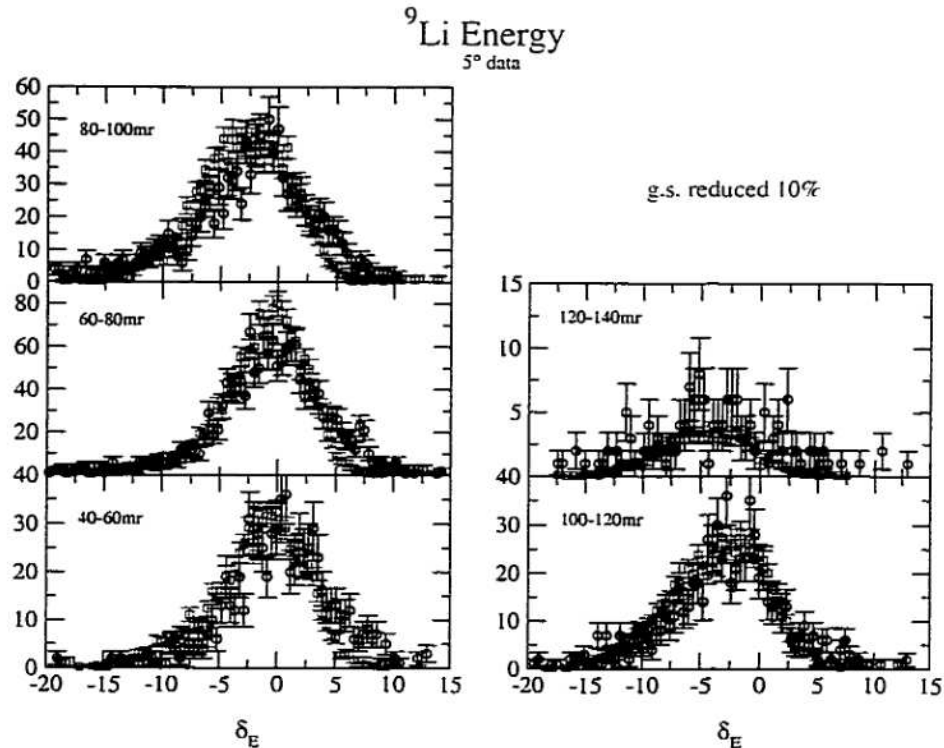
139

Figure 6.20. Energy distributions as in Fig. 6.17 but with the ground state probability reduced by 10% and the 2^+ state increased by 10%.

Due to this relative insensitivity, we can only place limits of $\pm20\%$ for the ^{9}Li DWBA calculations.

6.6 Acceptance results

One of the most important pieces of information provided by the Monte Carlo simulation is the acceptance of the S800. The opening angle of the spectrograph at the entrance to the first dipole (D1) is $3.5°$ (70mr) in the vertical direction and $5.0°$ (100mr) in the horizontal direction. However, the solid angle and acceptance are more complicated than that because of the two quadrupole magnets (Q1 and Q2) between the target and the dipoles. The exit of Q1 is 100 cm from the target with
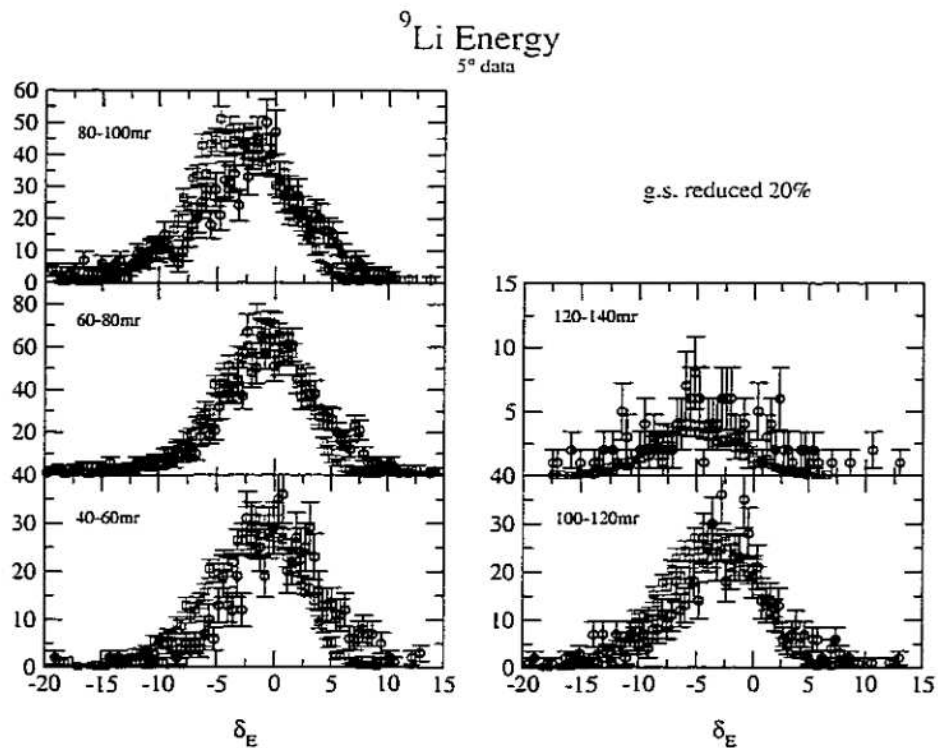
140

Figure 6.21. Energy distributions as in Fig. 6.17 but with the ground state and the 2^+ state contributions adjusted by 20%.
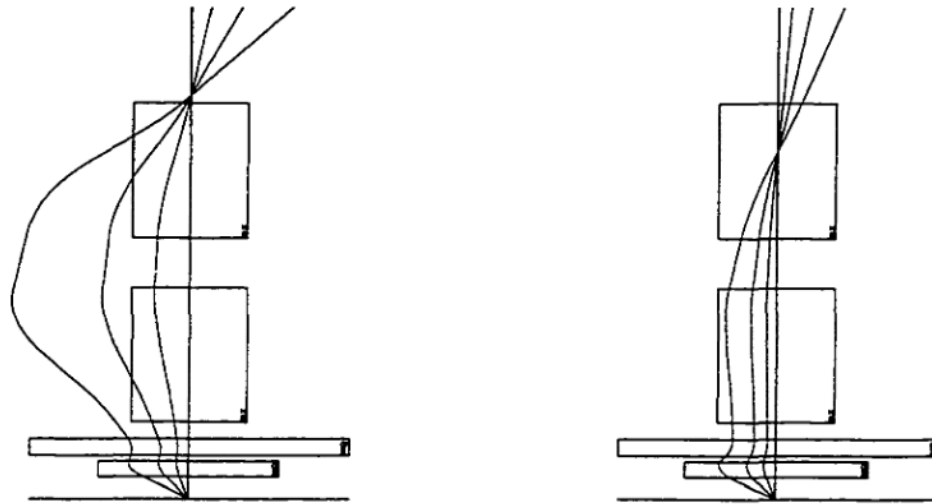
141

Figure 6.22. Trajectories for particles scattering at 20, 50 and 100 mr in the transverse plane through the S800 configured nominally (right) and with our settings (left)

an aperture of 12 cm. Q2 has an exit aperture of 21 cm at a distance of 163 cm from the target. Thus, Q1 has an angular acceptance of 120 mr and Q2 has an acceptance of 130 mr. However, since these are focusing elements, the straight-line geometrical method of determining the acceptance is not appropriate. Fig. 6.22 illustrates the effects of proper and improper focusing on the particle trajectories.

The typical acceptance, or effective solid angle curve, for this experiment is shown in Fig. 6.23, with a nominal acceptance curve given in Fig. 6.24. Independent checks [55] using our field settings compared to a nominal run show similar results as illustrated in Fig. 6.25. Immediately noticeable is the fact that our acceptance for this run was only ±50 mr in the transverse plane whereas the S800 was designed for over three times that much. The source of this limitation was improper field settings in the focusing quadrupoles. This was only the second experiment performed with the S800 Spectrograph and the operation of every element was not yet understood.
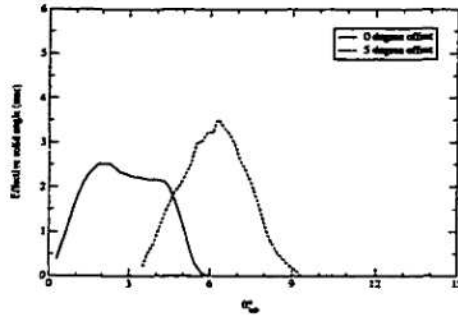
142

Figure 6.23. Typical effective solid angle for this experiment. This is the $2\pi \sin(\theta)$ factor multiplied by the spectrograph efficiency for our current settings.
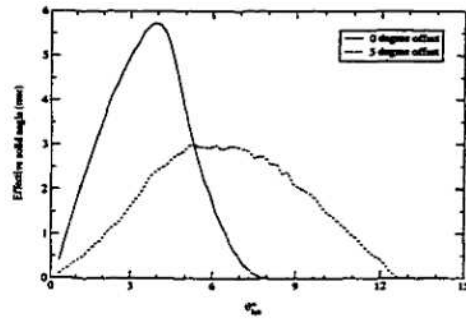
Figure 6.24. Nominal effective solid angle for the S800 at these energies. ($2\pi \sin(\theta)$ multiplied by the efficiency predicted from nominal settings.)
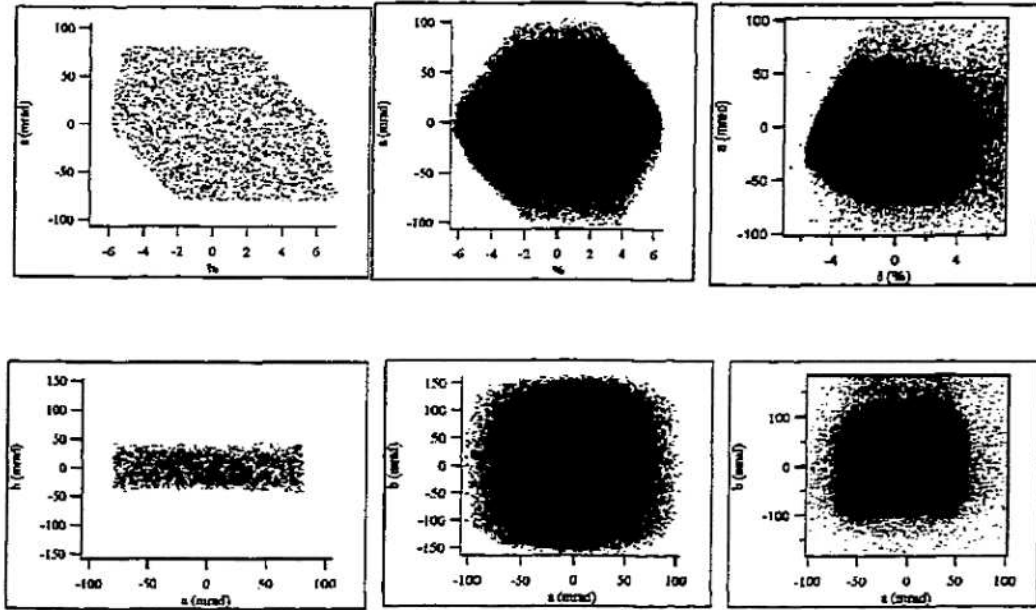
Figure 6.25. Calculations of the angular acceptance of the S800 as operated in this experiment compared with that of another experiment conducted with correct field settings. The data from the previous experiment are plotted in the rightmost panels. A Monte Carlo simulation of that acceptance [55] appears in the center panels. Finally the acceptance for this experiment calculated with the same Monte Carlo appears in the left panels. Note the greatly reduced acceptance in b, the transverse angle.

143

The saturation points of the magnets were not known. Rather than push the equipment at the risk of breaking something, the currents were kept in a lower, safe range. Furthermore, the A1200/S800 beam line monitoring system, BARNEY, was still a work in progress, with all of the "kinks" not completely worked out. Problems in the monitoring readout were discussed previously in §5.3.3.2. It also appears that the reference file that scales all magnets through the beam line only scaled some elements and not others, or was not consistent in the scaling process. The evidence for this is that, even though the dipoles of the S800 were set for particles of the appropriate magnetic rigidity, the quadrupoles were not. Since the time of this experiment in December 1996, further studies regarding the magnetic elements of the S800 have taken place, the results of which help to explain our limited acceptances. As an example, the maximum magnetic rigidity, or $B\rho$, that the S800 Spectrograph is designed to focus is 4.0 T·m. The ^{11}Li beam had a $B\rho$ of 3.75 T·m. Thus the magnets should have been very nearly saturated. Table 6.4 lists the expected saturation points [46] for the quadrupoles and dipoles, and compares them to the actual currents used in this experiment. Even though the quadrupole fields were substantially different from the appropriate settings, the ratio of Q1/Q2 is approximately right. Thus the only effects of the wrong quadrupole fields were reduced acceptance and smaller efficiency (because the more energetic particles that scattered to large angles were lost). Those particles that survived at the smaller angles behaved as expected and the ray-tracing analysis technique is valid.

The main implication of this limited acceptance is apparent when attempting to compare our disjoint data sets taken at 0° and 5.0°. If the S800 had been tuned properly, in the first part of the experiment we would have measured angles to around 6° (±5° horizontally, ±3.5° vertically) in the laboratory frame while in the second half we would have measured from 0° to just beyond 10° in the lab frame, providing a

144

Table 6.4. Comparison of expected saturation currents to the actual currents used in this experiment. Saturation currents correspond to particles of $B\rho = 4.0\,\text{T·m}$. Currents for the nominal and actual columns are for focusing particles of $B\rho = 3.75\,\text{T·m}$.

Element	Saturation (A)	Nominal ^{11}Li (A)	Actual (A)
Q1	80	70	50
Q2	90	80	58
D1	330	290	290
D2	345	300	300

significant overlap between the two data sets for normalization purposes. However, as the simulation and data confirm, we were only able to effectively measure up to 4.5° for the "zero-degree" data set, and only in to about 3.0° for the second configuration, providing little overlap between the data sets.

6.7 Scattering Results

Fig. 6.26 shows the direct beam contribution (including the exponential tail) to the ^{9}Li scattering distribution. The tail used in this background is identical to that determined from the no-target data, with the amplitude normalized to the ratio of the total number of events in the two scenarios. This beam contribution must be subtracted from the data. Then, the remaining counts are divided by the effective solid angle found from the Monte Carlo simulation to produce a cross section. Fig. 6.27 shows the final determined ^{9}Li distribution as a ratio-to-Rutherford, as measured in the zero-degree configuration. The theoretical curve is obtained by folding the absolute cross section from the DWBA calculation of Tostevin [56] with the experimental resolution and dividing by the Rutherford cross section. Rather than placing the experimental data points in the center of their respective bins, they have been placed at the average angle for a Rutherford distribution in that bin to reflect more closely the weighting of the distribution. Fig. 6.28 contains the
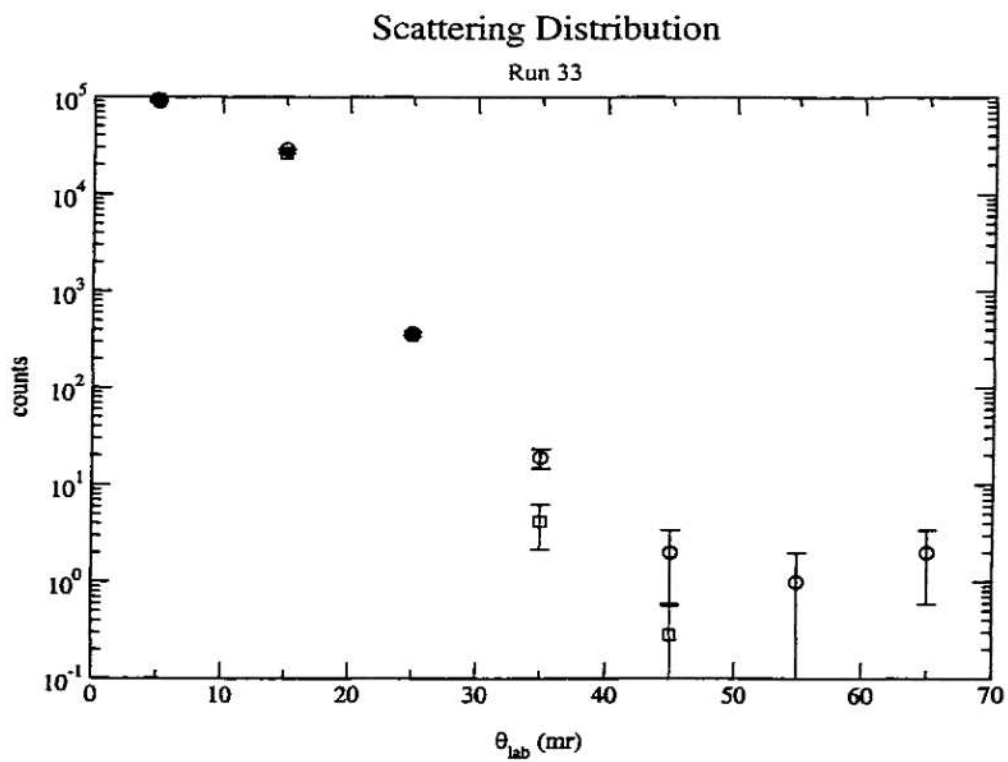
145

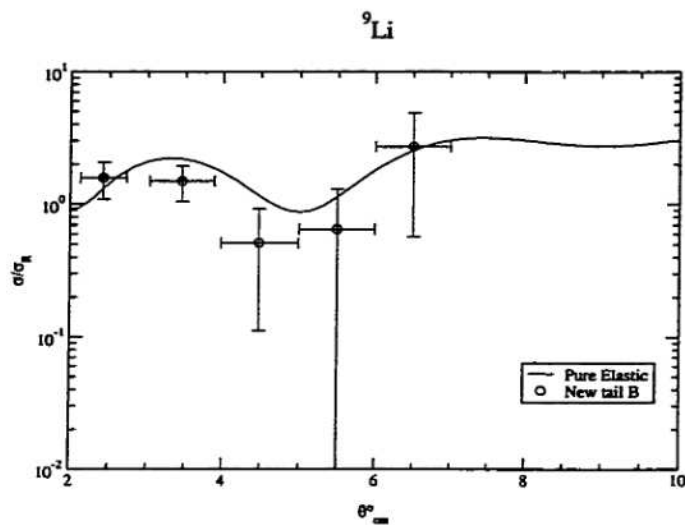Figure 6.26. Direct beam contribution to the ⁹Li scattering distribution as predicted from Monte Carlo calculations

146

^{9}Li

Figure 6.27. Final ratio-to-Rutherford distribution for ^{9}Li at 0°compared with the calculations of Ref. [56]. The calculations have been folded with the experimental resolution for direct comparison with the data. Vertical error bars represent both statistical and systematic uncertainties. The horizontal error bars reflect the systematic uncertainty in determining the scattering angle.
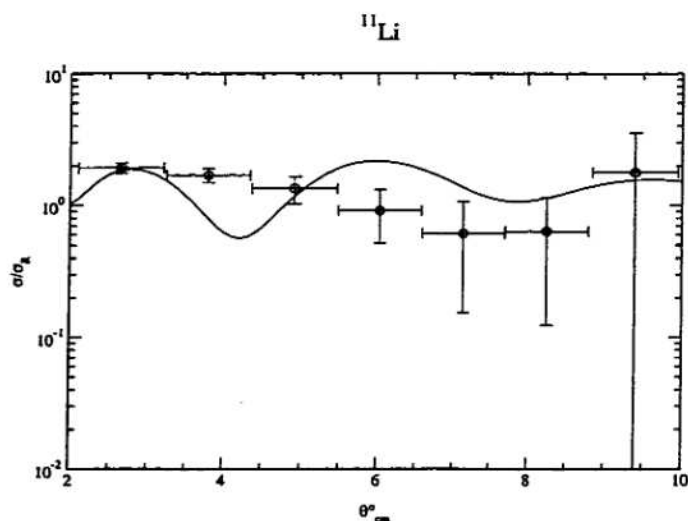

^{11}Li

Figure 6.28. Final ratio-to-Rutherford distribution for ^{11}Li at 0°compared with the calculations of Ref. [56]. The calculations have been folded with the experimental resolution for direct comparison with the data. Error bars are as in Fig. 6.27.

147

analogous results for ^{11}Li.

The results for the 5° configuration, where no direct beam contribution appeared, are shown in Figs. 6.29 and 6.30. The ratio-to-Rutherford results for the data were found by using the Monte Carlo simulation to produce the distribution that would be expected from pure Rutherford scattering of our beam profile. The experimental data point in each bin was then divided by its corresponding datum from the simulation. Since there is no direct beam in this configuration, the normalization is done so as to create a smooth overlap with the 0° data. Clearly, this is not ideal but it is all that the data allow. We can verify the shape of the distribution at these angles with great certainty, if not the magnitude. Due to the convolution difficulties discussed previously, these experimental distributions are compared with the theoretical quasi-elastic calculation rather than the pure elastic as was done for the zero-degree configuration. The theoretical curves in Figs. 6.29 and 6.30 have been obtained in the following manner. In the very forward region, where the angles are exclusive to the zero-degree data set, the pure calculation curves are folded with the experimental uncertainty of 10 mr in the laboratory frame. In the region of larger angles that are exclusive to the 5° configuration, the pure calculation curves are folded with the 20 mr (lab) resolution characteristic of that data set. For the middle range, where there is an overlap between data from the two configurations, an average of the two foldings is used. This not only provides a smooth transition between the two regions, it provides an intuitive way to compare the data in this overlap region. Overall, the results appear consistent with the theory at these angles. They are discussed in further detail in the next chapter.

148